POLITECNICO DI MILANO

Facoltà di Ingegneria Industriale

Corso di Laurea Magistrale in
Ingegneria Energetica

Numerical modelling of molten-salt thermocline storage systems: feasibility and criteria for performance improvement

Relatore:
Prof. Giampaolo Manzolini

Correlatori:
Prof. Andrea Lucchini
Prof. Michaël Kummert

Tesi di Laurea di:
Giovanni Angelini
770990

Anno Accademico 2011 - 2012

“Within 6 hours deserts receive more energy from the sun than humankind consumes within a year”

Dr. Gerhard Knies

Index

Figures index

Tables index

Abstract

The aim of this thesis is the assessment of the performance of direct molten salt thermocline thermal energy storage (TES) systems when applied to concentrated solar power plants. The considered thermocline employs solar salt at a temperature ranging between 550°C and 300°C. Thermocline TES is believed to be cheaper than state-of-art indirect two-tank TES (Andasol and Gemasolar type). The reason of this lower cost is the reduction of the number of vessels and the displacement of expensive molten salt in the tank by a low-cost packed bed (quartzite and silica sand): the packed bed acts as primary thermal storage. To better understand the behavior and performance of such TES, a two-dimensional finite-difference model is developed to predict temperature distribution in the thermocline vessel. The model includes heat transfer between molten salt and packed bed, both radial and axial diffusion as well as heat loss to the environment. The model is validated after comparison with four particular analytical solutions and with experimental data available in literature. Two performance indicators are defined in order to make a consistent comparison between thermocline and two-tank configuration: discharge efficiency and collection efficiency. Discharge efficiency is defined as the ratio of thermal energy withdrawn from thermocline TES at a temperature above 545°C on total thermal energy withdrawn. Collection efficiency is defined as the ratio of thermal energy stored in the TES on thermal energy available for storing. Both discharge efficiency and collection efficiency are equal to 100% for two-tank systems, while for thermocline TES they are found to be about 70% and 90%, respectively. It is observed that discharge efficiency is closely related to the thickness of the thermocline in the tank: further studies on molten salt and packed bed thermal conductivity, molten salt choice and tank height are made to assess if there is any chance to reduce thermocline thickness and, hence, to improve discharge efficiency.

Key words: Concentrated solar power plant, thermocline thermal energy storage, direct molten salt storage, discharge efficiency, thermal ratcheting, numerical modeling of heat transfer within a packed bed

Sommario

Nella presente tesi sono studiate le performance di sistemi di accumulo diretto di sali fusi in serbatoi a termoclino associati a centrali solari termodinamiche. Il sistema in questione utilizza “solar salt” a una temperatura compresa tra i 300 °C e i 550 °C. I serbatoi a termoclino hanno costi d’investimento molto inferiori rispetto ai classici sistemi a doppio serbatoio (Andasol e Gemasolar): infatti, si riduce il numero di serbatoi richiesto per l’accumulo e i serbatoi sono riempiti con un letto impaccato di rocce di quarzite e sabbie che ha un costo molto contenuto e rimpiazza un egual volume di più costosi sali fusi. L’accumulo termico avviene principalmente nel letto impaccato e non nei sali fusi. Per comprendere le perfomance degli accumuli a termoclino viene sviluppato un modello bidimensionale alle differenze finite che permette di prevedere la distribuzione di temperatura nel serbatoio. Il modello include la trasmissione di calore tra il letto impaccato e i sali fusi, le perdite termiche verso l’ambiente e la conduzione termica radiale e assiale. Il modello è validato a seguito del confronto con quattro soluzioni analitiche e con dei dati sperimentali disponibili in letteratura. Sono definiti due rendimenti che permettono il confronto delle performance dell’accumulo a termoclino con il sistema a doppio serbatoio: il rendimento di scarica e il rendimento di accumulo. Il rendimento di scarica è definito come il rapporto tra l’energia estratta dal termoclino a temperature al di sopra di 545°C e l’energia estratta totale. Il rendimento di accumulo è definito come il rapporto tra l’energia accumulata nel serbatoio e l’energia accumulabile. Entrambi questi rendimenti sono 100% per il sistema a doppio serbatoio, mentre sono rispettivamente 70% e 90% per l’accumulo a termoclino. Si osserva inoltre che il rendimento di scarica è strettamente dipendente dall’estensione del termoclino nel serbatoio: viene condotto uno studio di sensibilità sulla conduttività termica dei sali fusi e del letto impaccato, sull’altezza del serbatoio e sul tipo di sali fusi utilizzati per cercare di ridurre l’estensione del termoclino e, quindi, di aumentare il rendimento di scarica.

Parole chiave: Centrali termodinamiche, accumulo termico in serbatoi a termoclino, accumulo diretto di sali fusi, thermal ratcheting, modelizzazione numerica dello scambio termico tra un letto impaccato e un fluido.

Estratto in lingua italiana

L'accumulo diretto di sali fusi in serbatoi a termoclino ha dei costi d'installazione molto più contenuti rispetto agli accumuli termici a doppio serbatoio utilizzati attualmente nelle centrali solari termodinamiche (Andasol, Gemasolar) [1][2][3][4]. L'accumulo termico è responsabile del 15-20% del costo di installazione dell'impianto e una riduzione dei costi di tale sistema sarebbe auspicabile [5]. Infatti, serbatoi meno costosi permetterebbero di aumentare le dimensioni dell'accumulo con conseguente riduzione del costo dell'elettricità grazie al numero maggiore di ore equivalenti [3].

I sistemi a termoclino sono meno costosi perché viene ridotto il numero dei serbatoi necessari per l'accumulo termico; in più, il serbatoio a termoclino è riempito con un letto impaccato a basso costo che occupa l'80% del volume del serbatoio, rimpiazzando più costosi sali fusi. L'accumulo termico avviene principalmente nel letto impaccato e non nei sali [1].

Tuttavia il termoclino ha prestazioni di accumulo minori perché i sali ad alta e bassa temperatura sono a contatto tra loro: si instaura un gradiente termico, detto termoclino (Figure 0-1). È per questo motivo che tale sistema di accumulo viene detto "a termoclino".

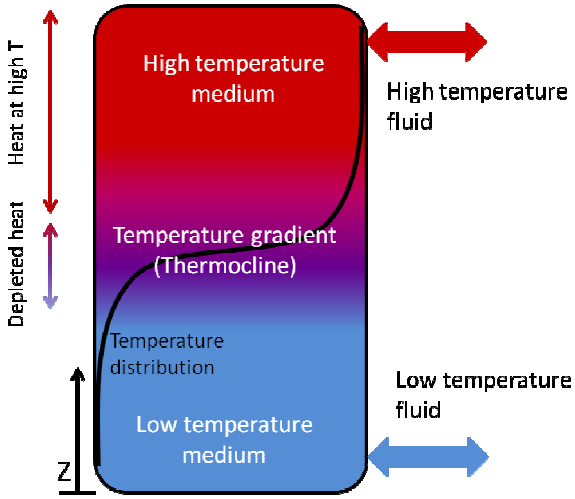

Figure 0-1: schema di un accumulo a termoclino

Le performance, come accennato, sono minori rispetto al sistema a doppio serbatoio perché una parte dei sali immessi a 550 °C vengono accumulato nel termoclino e vengono poi estratti ad una temperatura compresa tra i 550 °C e i 300 °C: gran parte di essi è inutilizzabile per la conversione termoelettrica, vista

la loro troppo bassa temperatura. Viceversa, in un sistema a doppio serbatoio, i sali fusi sono estratti costantemente a 550 °C.

Per comprendere il comportamento del termoclino viene sviluppato un modello 2-D alle differenze finite che permette di calcolare la temperatura dei sali fusi e del letto impaccato in ogni punto del serbatoio ad ogni istante temporale (Figure 0-2). Il modello include lo scambio termico tra letto impaccato e sali fusi, la diffusione termica assiale e radiale e le perdite termiche verso l'ambiente. Il codice è implementato in Matlab e il modello è stato validato mediante confronto con quattro soluzioni analitiche particolari e con dati sperimentali disponibili in letteratura.

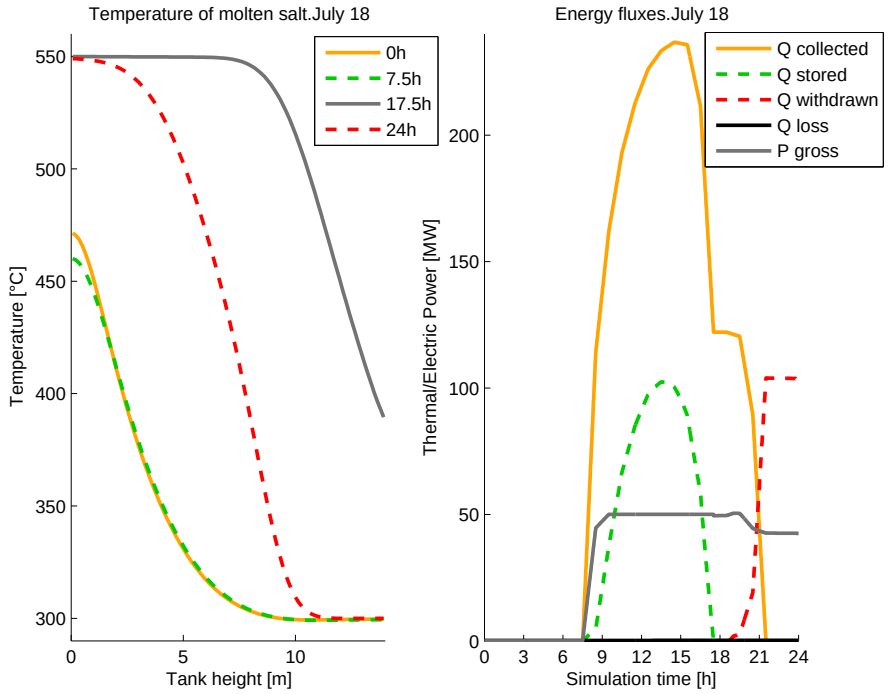

Figure 0-2: Temperatura del termoclino il 18 Luglio alle 7:30 (inizio caricamento), alle 17:30 (fine caricamento e inizio scarcia) e a mezzanotte (fine giornata, discharge continua oltre mezzanotte) (sinistra). Bilancio energetico 18 Luglio (destra).

Il modello è stato utilizzato dapprima per studiare fenomeni quali il "thermal ratcheting" e il fingering, che impedirebbero il corretto funzionamento dell'accumulo. In seguito, si valutano e confrontano le performance dell'accumulo a termoclino con quelle dei sistemi a doppio serbatoio, sia nel funzionamento estivo che in quello primaverile. Infine, sono condotte delle ricerche al fine di individuare l'accumulo a termoclino più performante.

Thermal ratcheting

Il termoclino è soggetto ad un fenomeno chiamato “thermal ratcheting” [6]. Il serbatoio tende ad allargarsi per dilatazione termica quando sali fusi ad alta temperatura vengono accumulati. Mentre il serbatoio si allarga, il letto impaccato si riassesta occupando lo spazio vuoto lasciato per via dell’espansione del serbatoio. Una volta che il calore è estratto, il serbatoio si raffredda e tenderebbe a restringersi per tornare al volume originale. Tuttavia, il letto impaccato non può più ritornare nella posizione originale, a causa della forza di gravità, e il serbatoio si ritrova costretto nella posizione dilatata. Ne risultano forti tensioni nella parete di acciaio del serbatoio: questi sforzi potrebbe portare allo snervamento, ad una propagazione ciclica della deformazione plastica, eventualmente fino al punto di rottura del materiale.

Il thermal ratcheting è studiato e tre possibili strutture per accumuli a termoclino vengono proposte. Vengono definiti un criterio semplificativo per la valutazione dello sforzo nella struttura metallica e un conseguente fattore di sicurezza rispetto al limite di snervamento $f_s = \sigma_{snerv}/\sigma$. I risultati mostrano che uno strato di isolante tra le pareti metalliche e i sali fusi è necessario per limitare l’impatto del thermal ratcheting. Questo isolante ha grande resistenza termica e riesce a mitigare notevolmente la temperatura dell’acciaio oltre che la sua dipendenza dalle variazioni di temperatura dei sali fusi all’interno del serbatoio. Vengono identificate tre strutture che resistono al thermal ratcheting con fattori di sicurezza tra 1,3 e 7,4.

Perdite termiche verso l’ambiente

Tuttavia, la coibentazione di due di queste è insufficiente e porta ad un raffreddamento dei sali troppo repentino. La struttura con fattore di sicurezza 7,4 offre invece una coibentazione molto migliore. Questa struttura è composta da uno spessore di isolante interno di 0,3 metri di materiale refrattario, di uno spessore di 0,03 metri di acciaio inossidabile e da un altro strato di isolante esterno di 0,15 metri di lana di roccia/vetro. Questa configurazione è scelta per le simulazioni che seguono.

Fingering

Un altro fenomeno studiato è il fingering, che consiste nello spostamento di un fluido da parte di un altro con diverse caratteristiche fisiche [7]. Quello che può avvenire è che invece di avere un fronte di avanzamento regolare, si potrebbe verificare una penetrazione del fluido iniettato nella matrice del fluido in quiete, provocando un miscelamento tra i due (Figure 0-3). Questo miscelamento è

indesiderato perché rovina la stratificazione termica e può aumentare considerevolmente lo spessore del termoclino.

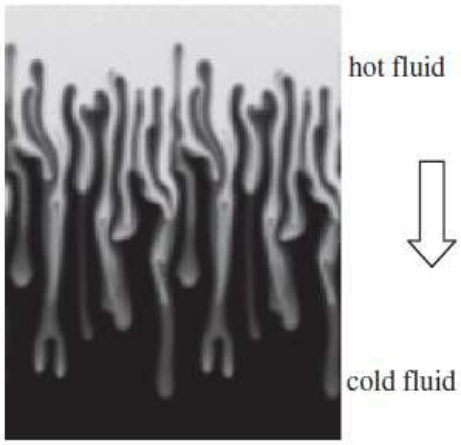

Figure 0-3: rappresentazione schematica del fenomeno del fingering [7]

In un termoclino a sali fusi, il fingering potrebbe avvenire durante lo stoccaggio di energia termica. I sali fusi ad alta temperatura sono iniettati nella parte alta del serbatoio; man mano, questi sali ad alta temperature spingono verso il fondo dell'accumulo i sali fusi a bassa temperatura. In queste condizioni, il "mobility ratio" è maggiore di uno e il fingering potrebbe avvenire. Studi più dettagliati e bilanci di pressione (legge Bernoulli e Darcy) permettono di individuare una velocità critica: se i sali fusi sono introdotti nel serbatoio al di sotto di questa velocità, l'effetto del fingering dovrebbe essere trascurabile. Si evince che questa velocità critica è un centinaio di volte superiore alla velocità tipica di immissione dei sali fusi negli accumuli a termoclino, quindi il fingering non rappresenta una minaccia per gli accumuli a termoclino studiati in questa tesi.

Previsione delle prestazioni degli accumuli a termoclino

Le prestazioni degli accumuli a termoclino vengono confrontate con quelle del sistema a doppio serbatoio; inoltre, la configurazione che dà le migliori performance è ricercata. Per comparare i due sistemi, il sistema a due serbatoi di una centrale solare termodinamica di cui si dispongono i dati orari (irraggiamento, portata di sali fusi al campo solare, al power block e all'accumulo) viene sostituito con un accumulo a termoclino [8]. Si cerca dapprima di determinare la dimensione del serbatoio ottimale, cioè il serbatoio che si comporta nel modo più simile possibile al sistema a doppio serbatoio. Sono definiti due rendimenti per confrontare le prestazioni dei due sistemi: il rendimento di scarica e il rendimento di accumulo. Il rendimento di scarica è

definito come la quantità di calore estratta dal termoclino a più di 545 °C diviso la quantità di calore estratta totale. In un sistema a doppio serbatoio il rendimento di scarica è sempre 100%, perché i sali fusi sono estratti a temperatura constante e pari a 550 °C. Invece, nel termoclino una parte del calore è stoccata a temperature tra 550 °C e 300 °C: solo la frazione estratta sopra ai 545 °C viene considerata come utile. Il rendimento di accumulo è definito come il rapporto tra l'energia accumulata nel serbatoio diviso l'energia totale utile per l'accumulo. Non tutta l'energia disponibile viene infatti accumulata nel sistema a termoclino: una volta che il termoclino raggiunge il fondo del serbatoio (accumulo quasi pieno), la temperatura dei sali fusi in uscita aumenta (>300°C) e alcuni specchi sono messi in posizione di defocus per evitare condizioni di eccessiva temperatura nel campo. Ciò provoca il mancato assorbimento di una parte dell'energia solare. Invece, nel sistema a doppio serbatoio il rendimento di accumulo è sempre 100% perché il sale fuso estratto dal serbatoio freddo è costantemente a 300 °C.

Test su settimana estiva – dimensione ottima accumulo a termoclino

Dapprima, le simulazioni sono fatte su una tipica settimana estiva con 7 giorni di sole e un elevato irraggiamento (9 – 15 Luglio): si ricerca la dimensione ottimale del serbatoio a termoclino. Si riscontra un trade-off tra il rendimento di accumulo e il rendimento di scarica. Per serbatoi di piccole dimensioni, il rendimento di accumulo è basso perché il serbatoio si riempie rapidamente e molta energia disponibile non viene stoccata (Figure 0-4).

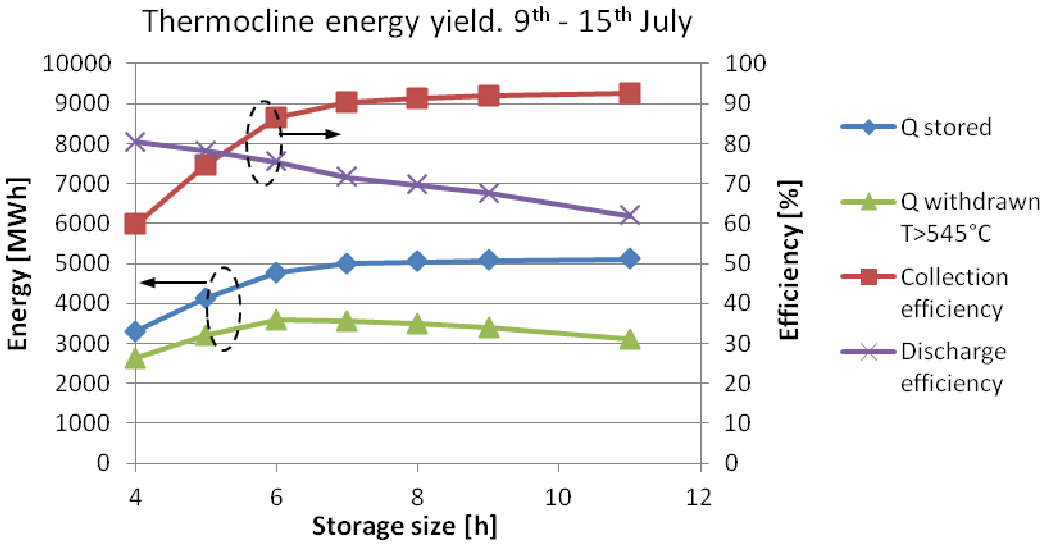

Figure 0-4: bilanci energetici e efficienze termoclino. 09 – 15 Luglio

D’altro canto, il termoclino è mediamente molto inclinato: un gradiente termico ripido separa nettamente la regione ad alta temperatura da quella a bassa temperatura, garantendo un’ottima stratificazione termica e un alto rendimento di scarica. Per un termoclino da 4h, cioè che può alimentare il blocco di potenza per quattro ore a potenza nominale, il rendimento d scarica è 80% e il rendimento di accumulo è solo 60%.

Per serbatoi di grandi dimensioni avviene il contrario. Il rendimento di accumulo è molto alto, perché quasi tutta l’energia raccolta riesce ad essere accumulata. Non si raggiunge comunque mai il 100%, ma un valore asintotico di 92-94%. Questo perché il termoclino raggiunge sempre la parte inferiore del serbatoio: alcuni sali vengono estratti a più di 300 °C e alcuni specchi vengono messi in defocusing per compensare l’aumento della temperatura dei sali fusi in ingresso. Per questi grandi serbatoi il termoclino è esteso e molta energia è stoccata tra i 545 °C e i 300 °C: il rendimento di scarica è quindi basso. I serbatoi sono sovradimensionati. Per un serbatoio da 9h, il rendimento di scarica è 67% mentre quello di accumulo è 92%.

Si trova che la dimensione ottima è 6h perché la quantità di calore estratta sopra ai 545°C è massima. In ogni caso, anche serbatoi da 7h e 8h sono delle possibili scelte, perché la quantità di calore estratto sopra ai 545 °C è solo leggermente inferiore. Viene però preferito un serbatoio da 7,5h perché il serbatoio da 6h è caratterizzato da variazioni di temperatura repentine indesiderate durante le fasi di carica e scarica. Durante la carica del serbatoio da 6h, la temperatura dei sali fusi cresce rapidamente appena il termoclino raggiunge il fondo del serbatoio (accumulo quasi pieno). Per evitare un surriscaldamento del campo solare, alcuni specchi sono messi in posizione di defocusing e entro mezz’ora l’accumulo è completamente pieno. Quando invece il termoclino raggiunge il top dell’accumulo, la temperatura dei sali, fino a quel momento di 550 °C, diminuisce rapidamente e il ciclo Rankine deve prontamente abbassare la pressione di evaporazione e la procedura di arresto della centrale viene avviata. Più il serbatoio è grande, meno queste variazioni di temperatura sono repentine. In conclusione, il serbatoio da 7,5h è scelto per le buone performance, vicine all’ottimo, e perché semplifica la conduzione dell’impianto.

Nella settimana estiva simulata il serbatoio da 7,5h ha un’efficienza di scarica del 70,6% e un’efficienza di accumulo del 90,9%. In questo termoclino, l’energia stoccata è 5019 MWh_{th} e quella estratta utile è 3518 MWh_{th}. Le perdite termiche sono 31 MWh_{th} e la variazione di energia interna molto piccola ($\approx$ 5 MWh_{th}). Quindi i restanti 1426 MWh_{th} sono estratti a una temperatura al di sotto dei 545 °C. Come confronto, nello stessa settimana un accumulo a doppio serbatoio avrebbe accumulato 5522 MWh_{th} e restituito 5450 MWh_{th} di calore al di sopra dei 545°C.

Test su settimana primaverile – scadimento prestazioni

Le prestazioni del sistema a termoclino sono testate anche su una settimana primaverile (23 – 29 Marzo). In questa settimana, la radiazione utile è inferiore rispetto alla settimana estiva e in un paio di giorni il cielo è molto nuvoloso. Nei giorni nuvolosi il termoclino è poco utilizzato: tutto il calore raccolto è inviato al blocco di potenza; negli altri giorni invece molta energia termica viene stoccata nell'accumulo e la produzione elettrica è estesa per 4-6 ore dopo il tramonto. In media, il serbatoio è usato in modo meno intenso che in estate: serbatoio da 7,5h è sovradimensionato per questa stagione e le prestazioni del termoclino si riducono. La dimensione ottimale è 6h e in questo caso gli accumuli da 7h e 8h sono sconsigliati. Nel caso da 7,5h, il rendimento di scarica scende a 65,8%, mentre il rendimento di accumulo rimane a 90,9%.

In realtà il blocco di potenza sarebbe capace di elaborare anche calore molto al di sotto dei 545 °C: per esempio, il blocco di potenza della centrale SEGS I è in grado di lavorare fino a 90 °C al di sotto della temperatura nominale [2]. Nel caso di una centrale che lavora a 550 °C, temperature fino a 475 °C potrebbero essere considerate come utili. Considerando 475 °C come temperatura limite, il rendimento discarica arriva al 95%. In ogni caso, questo rendimento non può più essere confrontato con quello del sistema a due serbatoi, che restituisce i sali fusi costantemente a 550 °C e, quindi, calore ad un'altra qualità.

Ricerche per il miglioramento delle prestazioni degli accumuli a termoclino

Infine, alcune simulazioni sono state condotte per cercare di individuare possibili miglioramenti delle prestazioni del termoclino, in particolare il rendimento di scarica. È già stato osservato che il rendimento di scarica è strettamente connesso alla pendenza del termoclino: si cercheranno quindi delle soluzioni per rendere il termoclino più ripido. Per esempio, si confronta l'impiego di due sali: il solar salt e l'Hitec. Le performance nei due casi sono simili, per via del simile comportamento dei sali nel'accumulo [9]. Tuttavia, i solar salt lavorano a temperature più elevate e il calore estratto dal serbatoio è convertito al blocco di potenza con rendimenti superiori che nel caso dell'Hitec. I solar salt sarebbero quindi da preferire.

In seguito, viene condotta un'analisi di sensitività sulla conduttività termica. Il risultato è che il termoclino si espande principalmente a causa del trasporto avvettivo dei sali fusi e solo in modo secondario per conduzione termica [1] [10][11][12]. La ricerca di sali fusi o letti impaccati con minor conduttività termica è quindi inutile perché la stratificazione termica non verrebbe migliorata in modo sensibile.

Infine, si prova ad aumentare l'altezza del serbatoio. Per via di limiti costruttivi, i serbatoi a sali fusi non possono superare i 14 metri di altezza [13]. Tuttavia, è ben noto che in serbatoi più alti la stratificazione termica è migliorata [1] [12][14]. Accumuli alti 25 metri mostrano un'efficienza di scarica aumentata del 5% rispetto ai serbatoi da 14 metri studiati finora. Aumentare l'altezza oltre ai 25 metri non è utile, perché la stratificazione è migliorata di poco e in compenso aumentano molto le perdite termiche, per via della maggiore superficie laterale esposta all'ambiente. Per raggiungere i 25 metri si è proposto un sistema di due serbatoi a termoclino da 12,5 metri collegati in serie. In questo caso, ci saranno due termoclini che si comportano in modo semi-indipendente in ognuno dei due serbatoi. Questa configurazione è molto interessante, ma studi più dettagliati sono necessari.

In conclusione, l'accumulo di sali fusi in serbatoi a termoclino è promettente perché ridurrebbe notevolmente i costi di accumulo termico nelle centrali solari termodinamiche. Tuttavia, le prestazioni di questi serbatoi sono inferiori a quelle del sistema a doppio serbatoio comunemente utilizzato: l'energia estratta ad una temperatura al di sopra di 545 °C è un 30-40% in meno che nel caso a doppio serbatoio. Una parte dell'energia estratta sotto ai 545°C è ancora utile per la generazione elettrica, che però avviene a carichi parziali e quindi con rendimenti di conversione inferiori a quello nominale. Per ottimizzare le prestazioni dei sistemi a termoclino si suggerisce di aumentare l'altezza dei serbatoi a 25 metri, magari collegando due serbatoi da 12,5 metri in serie.

Possibili studi futuri

Per meglio comprendere la convenienza dei sistemi a termoclino rispetto ai sistemi a doppio serbatoio si dovrebbero fare delle simulazioni su base annuale e confrontare l'output elettrico nei due casi [2]. In questo modo sarà possibile fare un'analisi dei costi tra i due sistemi e stimare il "levelized cost of electricity" per entrambi i casi. A questo fine, si consiglia lo sviluppo di modelli monodimensionali e monofase per delle simulazioni su base annuale dei sistemi a termoclino [2][15]. Infatti, si è riscontrato che per serbatoi ben isolati la distribuzione radiale della temperatura è quasi uniforme: quindi, il problema può essere trattato come monodimensionale. Inoltre, i sali fusi hanno velocità molto ridotte e lo scambio termico con il letto impaccato molto efficace: si riscontra infatti che la differenza di temperatura tra letto impaccato e sali fusi è sempre sotto ai 2°C: il mezzo può essere quindi trattato come monofase. Queste due ipotesi (monodimensionalità e omogeneità), semplificano il modello, aumentano la velocità di calcolo e rendono il modello applicabile a simulazioni annuali.

Introduction

Background

Humanity has always been searching for energy sources which could improve its life conditions. Indeed, there is a close connection between progress and availability of energy at low costs [16].

In the last 40 years, energy has grown at a rate of 1,9% every year most primary energy consumption relies on fossil fuels: in 2011, fossil fuels supplied 87% of worldwide primary energy consumption, which is estimated to be 12,7 Gtoe per year. Basically, consumption relies on resources like oil, coal, natural gas, biomasses and nuclear (Figure 0-1) [17].

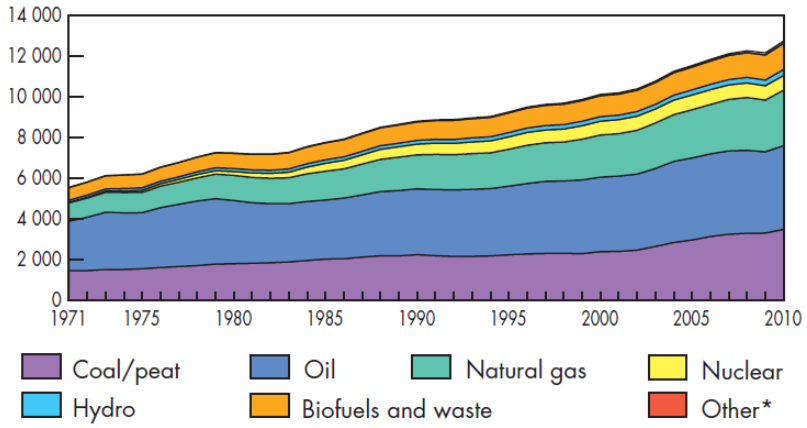

Figure 0-1: World total primary energy supply from 1971 to 2010 by fuel (Mtoe) [17]

In this scenario, electricity consumption is increasing even more quickly at a rate of 3,5% per year. Electricity consumption is assessed to 21 400 TWh, or 1,85 Gtoe per year (Figure 0-2). Fossil fuels are the main resource.

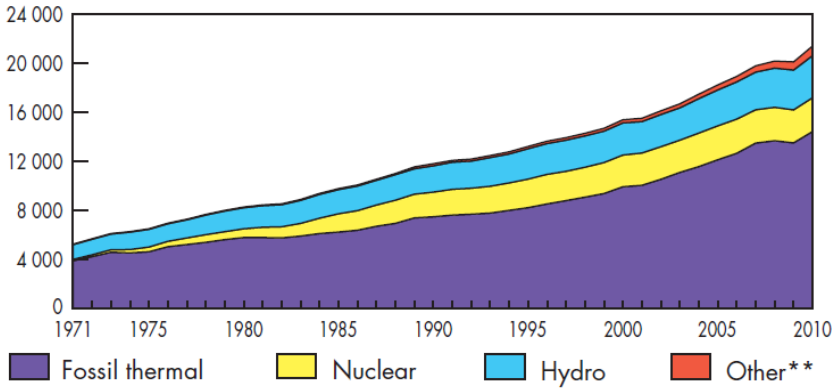

Figure 0-2: World electricity generation from 1971 to 2010 by fuel (TWh) [17]

Electricity is produced mainly in thermoelectric power plant burning fossil fuels. More in detail, 40,6% of worldwide electricity is supplied from coal, 22,2% from gas and 12,9% from nuclear. Among renewable energy, hydro has a significant share of 16% while other renewable together generates only 3,7% of worldwide electricity (Figure 0-3) [17].

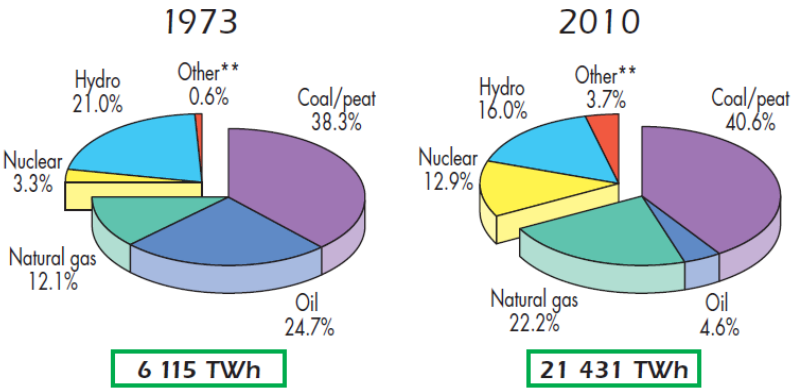

Figure 0-3: 1973 and 2010 fuel shares of electricity generation. **Other includes geothermal, solar, wind, biofuels and waste, and heat [17]

Such energy scenario is destined to default because reserves of fossil fuels are limited and because an excessive release of greenhouse gases (CO_2 in primis) could have severe effects on world climate. Energy consumption at present rates would exhaust reserves in few decades: according the British Petroleum statistics, reserves-to-production ratio (R/P) are estimated to be 55 years for oil, 65 years for gas and 110 years for coal [18]. Besides, the dependence of mankind on fossil fuels together with the depletion of reserves themselves have caused great price fluctuation of any kind of raw materials (oil, coal, gas and many other goods). This exposes international market to the behavior and politics of exporter countries, especially the few which export oil (Figure 0-4).

Figure 0-4: US Gulf Coast product prices 1994 – 2012. US $ per barrel [17]

It is for this reason that many nations are trying to reduce consumption of fossil fuels, optimizing consumption (energy efficiency) and shifting energy supply to other resources, such as wind, sun, waves, hydro, biomasses and waste, etc. Those resources are called renewable because they are available in almost infinite quantities: indeed, their rate of regeneration is quicker than the rate of consumption. Among those, solar energy is one of the most promising sources because of its large availability and because large scale exploitation is likely to be possible in the next future.

Several technologies have been developed for harvesting solar energy in order to supply electricity: for example, photovoltaic and concentrated solar power plants. The former is being massively installed in some countries as costs are dropping and technology is becoming competitive. Unfortunately, no electricity storage is possible and electricity generation is interrupted after sunshine. The latter is a promising technology because energy storage is possible and 24h electricity supply is feasible (plant of Gemasolar). Unfortunately, the cost of concentrated power plant is very high [5].

Objectives

In this thesis a particular energy storage which offers chances for cost reduction in concentrated solar power plants is studied. This system is direct molten salt thermocline thermal energy storage.
The thesis is structured in six chapters.

- In the first chapter, developed technologies for electricity generation are presented. Advantages and disadvantages of each are briefly discussed. Especially, concentrated power plants (CSP) are described.
- In chapter 2, possible thermal energy storages for CSP are scanned. Direct molten salt thermocline thermal energy storage (TES) is found to be a promising system. A simple cost comparison with the other systems is carried out.
- In chapter 3, literature review is made. Research methodology and findings on thermocline TES are presented.
- In chapter 4, a new two-temperature two-dimensional finite-difference model is developed to predict of the temperature distribution in the thermocline TES. The model is validated after comparison with four analytical solutions and with experimental data available in literature.
- In chapter 5, some issues of thermocline TES are presented and possible solutions are discussed. For example, the thermal ratcheting problem is studied and possible vessel envelopes are proposed. Also, fingering problem is faced.
- In chapter 6, performance of thermocline TES is compared to state-of-art two-tank configuration. Thermocline model is run under effective solar data

to perform weekly simulations. Also, design of thermocline TES which gives optimal storage efficiency and which behaves the most similarly to two-tank configuration is researched.

1 Electric supply form solar energy

The Sun behaves as a blackbody at 5774 K. In its internal regions, atomic fusion take place and hydrogen is combined to form helium. This reaction releases a large amount of energy, as described by Einstein mass-energy equivalence $E=mc^2$. Energy flows towards external surface of the Sun by convection and internal radiation, and it is finally emitted to the universe.

As described by Stephan-Boltzmann law, hydrogen and other elements are burn at a rate of $3{,}8 \times 10^{14}$ TW [16]. This energy irradiates the universe, and half a trillionth of it (approximately 172500 TW) is intercepted by Earth. This amount of energy depends of the diameter of Earth and Sun and on the distance between the two celestial bodies. Also, it slightly changes seasonally and depending on sunspot solar activity; radiation intensity can vary of about 5% maximum.

Radiation attaining external layers of the atmosphere of Earth is averagely 1364 W/m^2. This mean value of radiation/thermal power is called "solar constant". However, radiation is partially absorbed by the atmosphere and much less power reaches the ground. Elements in the atmosphere like CO_2, O_3, N_2O and H_2O absorb radiation of a certain wave length and re-emit it in the infrared spectrum. For example, O_3 absorbs very short-length radiation, also called UV, and protects Earth from this dangerous radiation. Also, air molecules, humidity and dust provoke scattering of radiation: basically, scattering deflect sun radiation in all direction, with a consequent loss in available radiation. As a result, effective radiation attaining Earth ground is about 1000 W/m^2 when the sun is at the zenith, and average annual radiation on Earth is assessed to about 198 W/m^2 [19].

Totally, Sun irradiates Earth with 885×10^6 TWh every year [16], which is about 6000 times the yearly primary energy consumed by mankind. In other words, in just 90 minutes sun supplies enough energy to satisfy annual energy needs of humanity[5]. While fossil resources are limited in time, solar energy is widely available and completely renewable (Figure 1-1). Large-scale harvesting of solar energy has the potential to solve the energy supply problem.

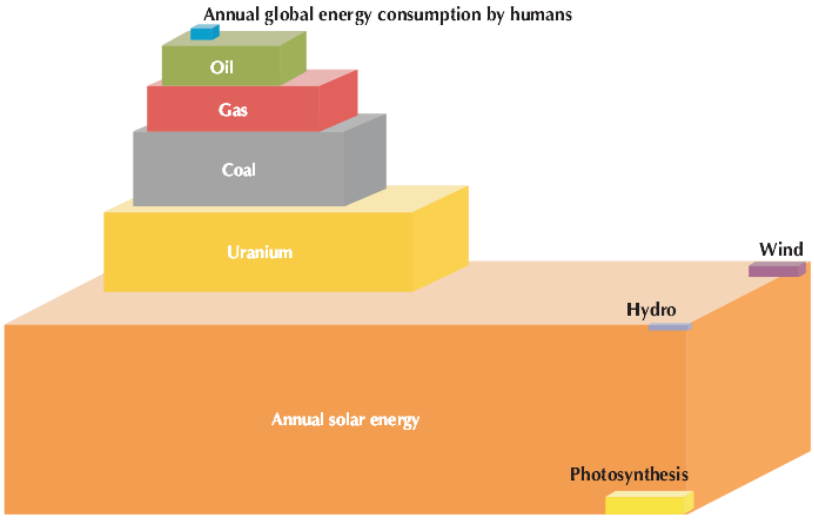

Figure 1-1: Total energy resources [19]

In the last decades many efforts have been addressed to develop systems in order to exploit solar radiation for electrical supply. Two main technologies have been developed: photovoltaic and thermal conversion technology.

1.1 Photovoltaic

Photovoltaic performs direct conversion of both beam and diffuse radiation in electricity. This system exploits the photovoltaic effect: a photon hit an electron of a material transferring a share of its energy. The electron results "excited" and it leaves the lower energy orbital. Hence, collision between photons and electrons generate an electronic flux, i.e. an electric current. Particular materials, called semiconductors, are used to effectively collect those excited electrons and extract the energy they gained.

In semiconductors there is an electronic energy gap between the valence band and the conductive band. Most of photons are enough powerful to push electrons over this gap, exciting them. To effectively capture these excited electrons, two semiconductors are joined. The first is a positive doped semiconductor and the second a negative doped semiconductor. This junction results in a permanent electric field which manages to effectively displace electrons once excited (Figure 1-2). So, electrons are collected and an electric current is obtained.

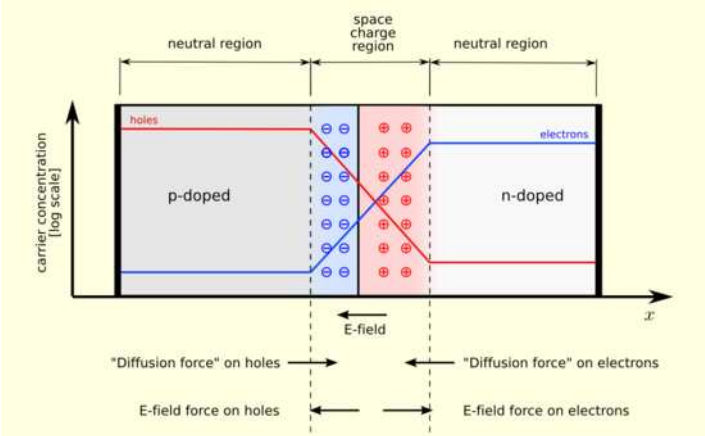

Figure 1-2: p-n junction [21]

Unfortunately, photovoltaic efficiency is limited to about 10-20%. This is because only a certain share of photonic energy can be exploited. First, electrons must overcome the "energy gap" between the valence band and conduction band. For silicon, this gap is 1,12 eV and only 78% of photons are enough powerful to push electrons above this energy barrier. Second, all photonic energy above the energy barrier is lost because it is not transferred to electrons. In silicon, photons transfer just 1,12 eV to electrons, even if their internal energy was higher. This causes an avoided absorption of other 25% of available photonic energy [20].

Besides of this 50% photonic loss, large-scale constructive issue and technology further limits photovoltaic efficiency to 10-20%. More efficient modules exist, such as multi-junction panels. However, considering their cost and materials used, they are unsuitable for large-scale utilization [20].

Besides of the low efficiency, photovoltaic is a very energy intensive process and PV panels are very expensive. Melting of silicon and further purification processes require big amount of energy. Silicon for solar application has a degree of impurities below 10^{-4} ppm (solar grade silicon). Also, much silicon is wasted when coarse solar grade silicon is cut and shaped in wafer, just before panel assembly.

The overall cost of photovoltaic is assessed to typically 1800-2400 €/kW and incentives are required to make it competitive [22]. Although, research is sharply reducing the costs. It has been estimated that every time worldwide installed capacity is double, photovoltaic cost is reduced of 20% [22].

In the past years installed capacity sharply increased. In 2012, about 30 GW have been installed worldwide increasing the overall installed capacity to about 100 GW in February 2013, according to EPIA statistics. Germany, Italy, Spain, Japan, USA, Taiwan and China are leader either in production or/and in installed capacity (Figure 1-3) [22][23].

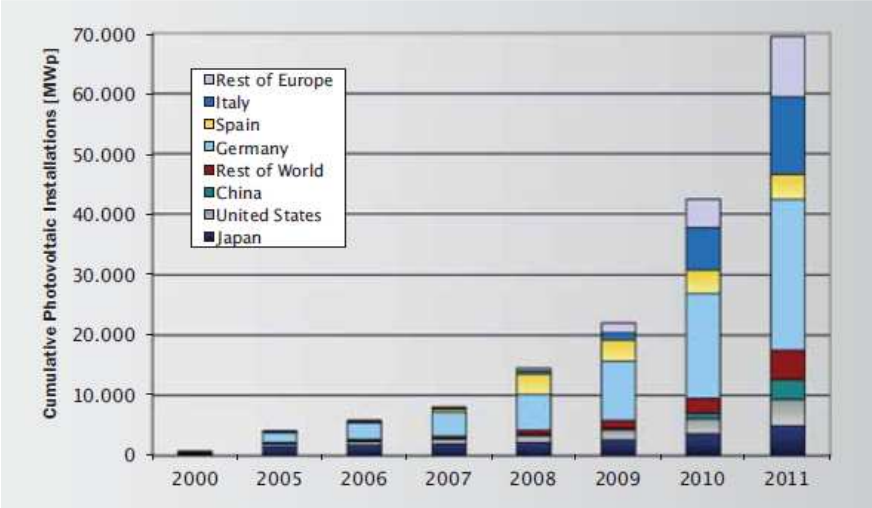

Figure 1-3: Worldwide cumulative PV installed capacity [22]

Researchers are developing new photovoltaic technology to reduce costs and to reduce the amount of energy required to build them. Especially, second-generation thin-film panels use much less semiconductor material than first generation panels [24]. Typical second-generation PV are CdTe, amorphous Si and CIGS cells. Costs are contained, but rapid oxidation of those cells limits their efficiency and lifetime. Since few years, third-generation organic cells have been developed. Those cells are capable for further cost reduction because they are made with very low-cost materials; unfortunately, their performance are very poor: efficiency of state-of-art laboratory-cells hardly overcomes 8% [25] (Figure 1-4).

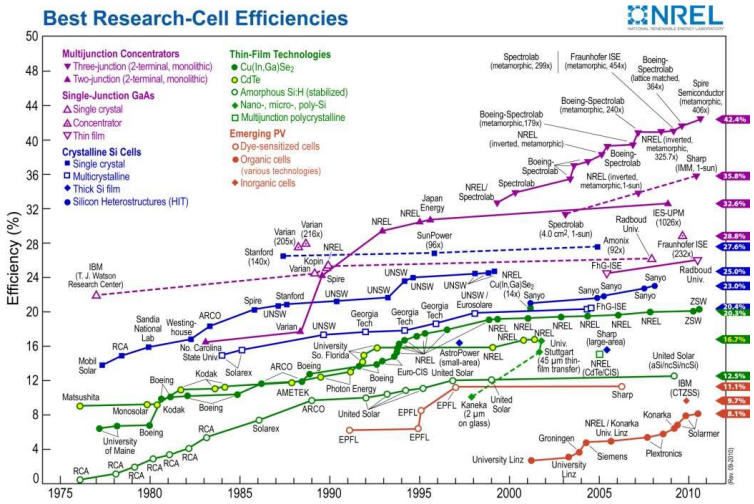

Figure 1-4: Photovoltaic cell efficiency - laboratory tests [25]

There are still many doubts about photovoltaic for large-scale electrical production. Indeed, solar radiation is available only few hours per day, and electric storage is very expensive and possible for only little electrical quantities. Despite of that, big photovoltaic facilities have been realized and others are under construction. For example, the biggest photovoltaic plant is “Agua Caliente Solar Project”, in Arizona. It sizes 247 MW with 5.2 millions of modules spread on 970 hectares of desert surface (Figure 1-5). Also, two thin-film 550 MW PV facilities are under construction in California: “Desert Sunlight Solar Farm” and “Topaz Solar Farm”.

Figure 1-5: Agua Caliente PV facility

Large penetration of photovoltaic (and wind) in the electrical production would result in an unbalanced electrical grid. To solve this issue, “smart grids” and the concept of dispatchable loads must be developed: as photovoltaic production is intermittent, the only way to effectively exploit its output is to displace consumption when photovoltaic energy is available. However, smart grids are still at early stage of development.

Summing up, photovoltaic is a promising technology, but it is unsuitable neither for large-scale electric production nor as base load electric supply because of the intermittency of radiation and the impossibility of energy storage.

1.2 Thermoelectric conversion

In solar thermal power plants solar thermal energy is converted through a thermal process to electricity. So, energy conversion in a solar thermal plant is completely different than in photovoltaic technology (PV). PV exploits the photoelectric phenomenon and radiation is converted directly to electricity. In a thermal process, radiation is converted to heat and then to electricity, i.e. an indirect process. Solar thermal conversion is rather similar to a thermoelectric power plant where heat from solar radiation replaces heat from fuels.

The biggest advantage of thermoelectric solar power plants compared to other renewable technology and to PV is the possibility of thermal energy storage (TES). When much radiation is available heat is stored in the TES; when radiation drops, heat is withdrawn from the TES and supplied to the thermal block for extra electric production. For example, the TES feeds the power block during cloud passages or after the sunset. So, in solar thermal power plants solar intermittency is controlled: the TES allows to produce electricity even if radiation is insufficient or absent. Another advantage is the increase in the load factor of the solar thermal plants. Load factor in solar thermal power plants without storage ranges between 20% and 25%, while in plants equipped with a 6h-7.5h full-load capacity TES it is between 40% and 55%. Also larger TES of 15h have been realized, with load factors of 75% (Gemasolar) demonstrating feasible power production for 24 hours per day for many weeks of the year [5]. Summing up, dispatchability is the main advantages of thermoelectric solar power plants.

Another interesting possibility is the Integrated Solar Combined Cycle. This gas combined cycles are equipped with a solar field which supply heat extra thermal power to the bottomed Rankine cycle. The biggest plant in the world is the 75 MW Martin Next Generation Solar Energy Center, in Florida. Here, a share of the electric output is associated to solar contribute, while the remaining is associated to natural gas.

In solar-only driven thermal power plants, thermoelectric conversion of solar energy is performed either in no concentrated plants or in concentrated plants, depending on the absence or the presence of a concentrating device for solar radiation. Concentrated option is more attractive because very high temperatures are reached and good thermal conversion is possible, as described by Carnot's law. Developed thermoelectric conversion systems are:

a. Not concentrated systems
    - Solar Pond
    - Solar updraft tower
b. Concentrated solar power (CSP) plants
    - Parabolic trough
    - Central receiver
    - Fresnel collectors
    - Solar dish

Unfortunately, only beam radiation is exploitable in CSP plants, because radiation is concentrated. Beam radiation is the share of solar radiation that arrives directly from sun; in contrast, the share of solar radiation that had been scatted by atmospheric molecules, humidity and dust is called diffuse radiation. Beam radiation is about 80% of total radiation. PV exploits both diffuse and

beam radiation while concentrated power plants and concentrated PV only exploit beam radiation. Hence, less radiation is available for CSP and this limits the regions where CSP plants are economically convenient. Sites with high annual irradiation and many sunny days per year are required, which limits possible application to much less sites than PV. For example, very good sites are Saharan desert, southern Spain and oriental USA. All these regions have average yearly direct irradiance above 2000kWh/m^2.

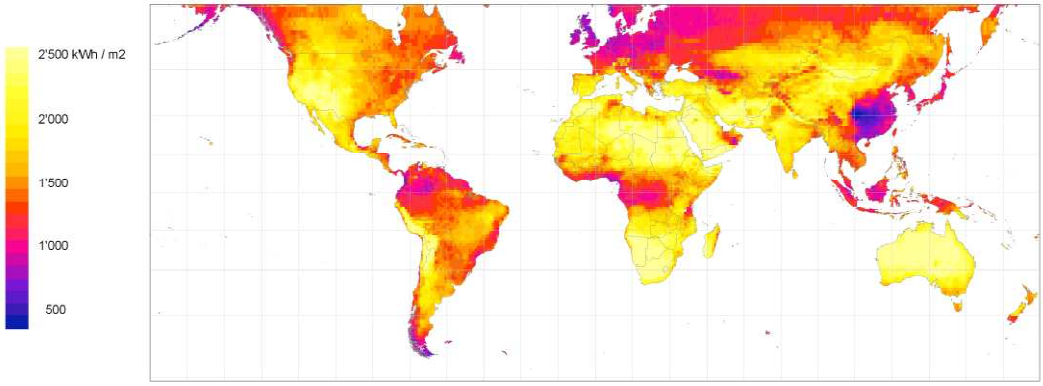

Figure 1-6: Yearly sum of direct normal irradiance [26]

One of the biggest disadvantage of solar thermal power plants is the high installation cost, assessed between 3500 and 5000 €/kW [5]. This is 4-5 times the cost of conventional fossil and about twice the cost of PV systems. Also, operation and maintenance costs are higher than in conventional plants and equivalent working hours are less, even when thermal energy storage are added. As a result, thermal solar power plants are far to be economically competitive.

However this technology offers the chance for great cost reduction. There are only few plants worldwide. Hence, the exploitation of economies of scale is at early stage [5]. At the beginning of 2012, 1,9 GW of installed capacity were operative worldwide, mostly in Spain and USA (Table 1-1). This capacity is very little compared to the 100GW of installed PV technology. However, many plants will be operating in the next years: 2,5 GW under construction, and more than 10GW have been announced between Spain, USA, China and few other countries.

Table 1-1: Operating CSP in the world [27]

Country	CSP operating at the beginning of the 2012
Spain	1331 MW
USA	518 MW
Rest of the world	75 MW

1.3 Not concentrated solar power plants

1.3.1 Solar pond

Solar pond system consists in a pool of saltwater. The floor of the pool is a black absorptive surface. As a result, deep water of the tank is sensibly heated up. Free convection is prevented to take place because of the salinity gradient: the hotter lower fluid has great content of salt, and it is heavier than the colder but lighter water at the surface of the pool. Hence, thermal gradient is balanced by a "halocline", i.e. saline gradient, free convection is prevented and good thermal stratification is obtained. Hot water is then used to drive an organic Rankine cycle engine. Typically, salt is $NaHCO_3$.

There are only few solar ponds in the world. The biggest was the 5MW plant of Beit HaArava, Israel, which was decommissioned in 1988. Here, water temperature was 30°C at the surface and 90°C at pool floor [28]. Temperature gap cannot be further pushed, because above 100°C water starts to boil. Thermal efficiency is quite low because of the little temperature difference; according to Carnot, its maximum value is about 16,5%. Nowadays, the biggest operating solar pond is El Paso, USA (Figure 1-7).

Figure 1-7: El Paso solar pond

1.3.2 Solar updraft tower

Solar updraft tower exploits the "chimney effect", i.e. the density difference between warm and cold air, to generate an air stream which drives wind turbines. Solar updraft tower are composed by glass structures which covers a large land surface and a central tall hollow tower. Below the glass roof

air is heated up by solar radiation, due to greenhouse-like effect. This warm air is lighter than external cold air and it tends to climb in the hollow chimney. The warm air stream is intercepted by wind turbines at the entrance of the chimney, converting kinetic energy of air into electricity (Figure 1-8).

Unfortunately, to achieve big electric output the tower must be very tall, even 1000-1500 m, and glass surface should cover several km^2, which results to be economically and technically unattractive. Indeed, solar updraft tower occupies big land surface is generating little power outputs. Solar radiation would be more efficiently harvested with other solar technology. Despite of that, some big project have been proposed, such as the 200 MW Enviromission tower in Arizona or the 400 MW Greentower in Namibia.

The only solar updraft tower ever realized was Manzanares, build in Ciudad Real, Spain in 1982. It was a 195 m tall tower and glass roof occupied 46 hectares; nominal power was 50 kW (Figure 1-9). The tower was built with low-quality materials and suffered rusting and corrosion. The systems failed in 1989 when a storm blew down the tower.

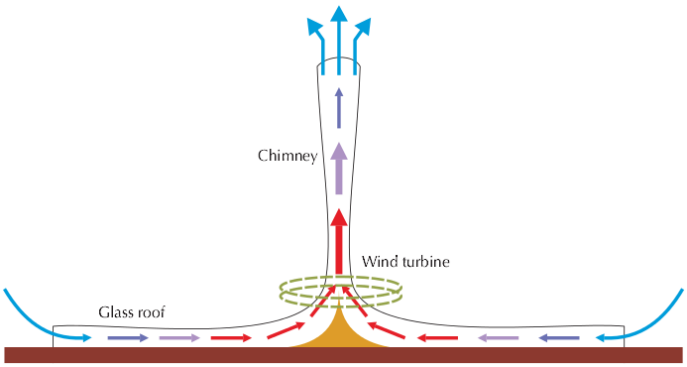

Figure 1-8: Solar updraft tower scheme

Figure 1-9: Manzanares updraft tower

1.4 Concentrated solar power plant

In CSP plant solar radiation is reflected on mirror surfaces and concentrated. A receiver body receives radiation from mirrors, heating itself up and reaching high temperatures. This receiver body is hollow and a heat transfer fluid (HTF) is forced to flow through it, cooling it down. The hot HTF leaves the receiver body and it is displaced towards a power block, which absorbs heat and converts it to electricity. Sometimes CSP plants are also equipped with thermal energy storage: in these plants a portion of the heat collected at the solar field is stored at mid-day hours and then used at low radiation hours.

The area of the mirrors is widely larger than the surface of the absorber and thermal power hitting the absorber is great. The ratio between the reflecting surface extension S_r and the surface of the absorptive surface extension S_a is called solar concentrating ratio. Radiation hitting the absorber is equal to solar beam radiation multiplied by this solar concentration ratio. Solar concentration ratio cannot tend to infinite because of geometric considerations. Indeed, Sun subtends Earth with an angle of 0° 32'. Hence, solar radiation hitting Hearth is not perfectly perpendicular, but rather contained in a cone-shaped volume. As a result, concentration ratio is limited to about 215 in linear concentrating system, while in punctual systems much higher values up to about 46 000 are attainable [29].

Several collectors have been developed. They are classified in linear and punctual. In the former, mirrors track the sun along one angle, either azimuth or solar altitude; these systems are parabolic trough, which is the state-of-art technology, and linear Fresnel concentrators, which are cheaper but less performing collectors. In the latter, mirrors track the sun along both azimuth angle and altitude angle; for example, solar dishes, which are suitable for off-grid or distribute generation, or power tower systems, which allows to reach high concentrating factors.

1.4.1 Parabolic trough

Parabolic trough is the state-of-art technology and it is used in about 90% of CSP plants in the world (Table 1-2). Mirrors are parabolically shaped in order to reflect normal radiation to their focal point (Figure 1-10). The absorber body is a tube placed in the focus of the parabola and it receives all radiation reflected by mirrors (Figure 1-11). The absorber is composed of a metallic tube surrounded by a protective glass envelope, which prevent corrosion of the tube and limits convective heat loss with the environment. An HTF flows inside the absorber, progressively heat itself up and leaves the solar field at high temperature. The hot HTF is finally pumped to the power block, where thermal-

to-electric energy conversion takes place. Solar concentration ratio of this mirrors ranges 60-80 [5].

Parabolic trough mirrors are supported by a metallic structure and they are equipped with tracking device. Mirrors can rotate around their longitudinal axis and hence they are oriented to intercept the maximum of solar radiation at any hour of the day. If parabolic trough is North-South oriented, inclination of mirrors is equal to the azimuth solar angle; if parabolic trough is East-West oriented, inclination of the mirror is always equal to solar altitude angle. Usually, North-South orientation is preferred, because the amount of radiation collected over a year is more than in East-West layout. However, East-West orientation manages to collect radiation more constantly during the year.

Table 1-2: Worldwide CSP operating plants, by CSP type [27]

CSP type	Installed capacity [MW]
Parabolic trough	1800
Central receiver	70
Linear Fresnel concentrators	35

Figure 1-10: Parabolic trough solar field

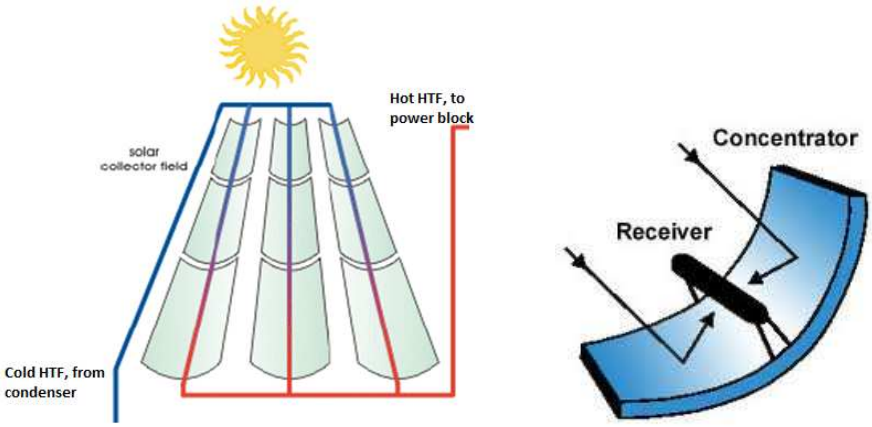

Figure 1-11: Parabolic trough scheme [30]

Parabolic trough collectors are characterized by both thermal and optical losses. Optical efficiency is the ratio between the quantity of solar radiation which attains the absorber and the available solar radiation. Many geometric and optical phenomena influence optical efficiency, such as shadowing effect, reflection of the mirrors, absorption of the absorber tube, transmittance of the protective glass envelope, etc. Thermal efficiency is defined as the ratio between radiation attaining the absorber and thermal energy effectively transferred to the HTF. To limit convective heat loss, vacuum is maintained between the absorber tube and the glass shell. Further, a selective coating is applied on the surface of the absorber tube: selective coating is a silver or tin oxide which optimizes absorption of solar radiation and prevents emission of radiation typical of bodies at low temperature, such as the absorber. The selective coating is applied also to PV and makes them look blue. The overall performance of parabolic trough collectors depends mainly on average temperature of the HTF and on average irradiative solar intensity

Concluding, parabolic trough is the most employed system for CSP plant. It is reliable and very performing. Although, it is quite expensive: the complex parabolic shape of the mirror and the absorber itself lead to high costs per collector unit. Further, collectors cover a very large surface: solar field is responsible of about 50% of the cost of the entire CSP installation [5]. To sum up, its reliability and good cost-effectiveness ratio make parabolic trough collectors the state-of-art technology.

1.4.2 Linear Fresnel collectors

Linear Fresnel collectors are the second type of linear collector. The reflecting surface is composed by straight thin flat mirrors which lean on the ground and which can rotate independently along their longitudinal axis. Mirrors point the absorber body which is placed above them. This structure is simpler and lighter than the parabolic trough. As a consequence, it is also cheaper. The absorber is

substantially the same as in the parabolic trough. Another advantage is very little shading effect; hence less land is occupied than in the parabolic trough case (about half). Also, mirrors are ground-based, so operation and maintenance (i.e. cleaning) is simpler.

Linear Fresnel collectors are suitable for direct steam generation (DSG). In parabolic trough the absorber rotates with the mirrors and ball joints are present in the collector. Direct steam generation requires high pressure ranging 50-100 bars and ball joint cannot stand those pressures. Hence, DSG is impossible in parabolic trough. On the other hand, absorber of Fresnel collectors is fixed and only the mirrors rotate. Hence, DSG is possible in linear Fresnel collectors.

However, cheapness is compensated by relative poor performances. Nominal optical efficiency is quite poor: about 65% versus the 75% of parabolic trough [31]. Most of optical losses are due to geometric loss. Indeed, the reflecting area is less than the opening (illuminated) area, even at zero incidence angle (Figure 1-12). Mirrors are not normal to sunray because they are oriented to deflect radiation to the absorber. Hence, a cosine effect causes a loss in the real reflecting area. Particularly, when the sun is low on the horizon this cosine effect affects is much relevant. Instead, mirrors of parabolic trough can swing and their aperture area is always normal to solar radiation. As a result, at off-design conditions the optical efficiency gap between parabolic trough and Fresnel mirrors is even increased.

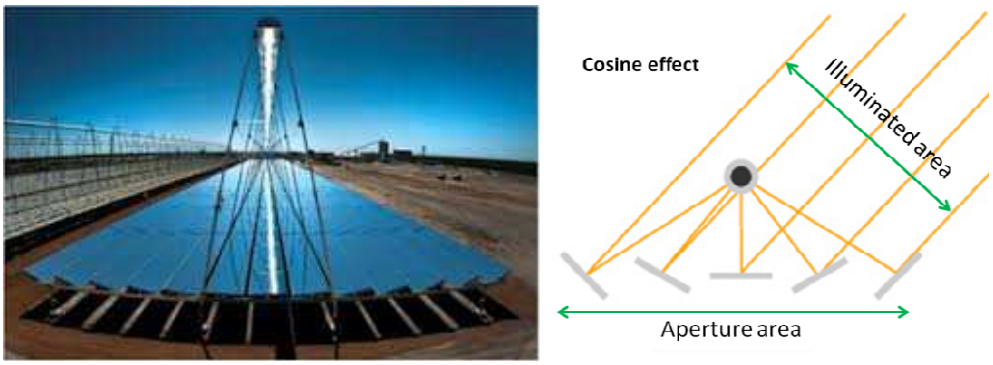

Figure 1-12 : Fresnel mirrors (left) and cosine effect – optical loss (right) [32]

Summing up, Fresnel concentrators are sensibly cheaper than parabolic trough and they allow DSG. However, parabolic trough is still preferred because of their greater optical performance.

1.4.3 Central receiver

Central receiver system, or solar tower system, consists in a tall tower surrounded by a field of thousands of heliostats. Each heliostat has a surface of

about 100 m^2 and tracks the sun rotation along both azimuth and altitude angles. Heliostats reflect solar radiation to a heat exchanger placed at the top of the tall central receiver. All heliostats are equipped with electromechanical devices called “trackers”, which continuously orientate mirrors depending on sun position. Concentration factors are typically of 1000-5000 and temperature at the top of the tower reach easily 600 °C – 1000 °C (Figure 1-13) [33].

Figure 1-13 : Gemasolar facility

Central receiver plants are theoretically more interesting than parabolic trough. These CSP plants offer better optical efficiency than parabolic trough technology and they are good candidate for large thermal energy storage. Very high temperatures can be attained and many studies are being carried out on the power block: it is indeed possible to replace the actual Rankine cycle with more efficient combined cycles. Central receiver technology has been demonstrate as promising and feasible with any storage type and any heat transfer fluid but it is still little developed compared to parabolic trough plants.

Technological and economical problems hinder the development of large solar power tower facilities. Central receiver systems are constrained in size for two reasons. Big plants require very high towers above 150 m. Here, very high temperatures are reached and costly materials are required for both the tower and the receiver body/heat exchanger. Also, optical losses are high because closer heliostats block the radiation reflected by outer heliostats. This optical phenomenon, called “blocking” or “interference”, reduce effective radiation collected from outer mirrors. From an economic point of view, the two-axis tracking orientation electro-mechanic system of heliostats is quite expensive, considering the required degree of precision: mirrors must continuously reflect radiation to the heat exchanger at top of the tower, which sizes hundreds of square meters and which is up to 1 km distant. Another issue of central receiver plants is connected to the little thermal inertia of the tower: when radiation

drops, available thermal power decrease in a while, causing a drop in thermal power available at the power block and causing thermal stress in the mechanical equipment [33].

Only few central receiver plants sizing more than 10 MW have been realized: Solar One and Two (USA), Gemasolar (also called Solar Tres, Spain), PS10 (Spain) and PS20 (Spain). All kinds of HTF have been used: steam/DSG (PS10 and PS20), mineral oil (Solar One) and molten salt (Gemasolar, Solar Two). These plants were equipped with very different storage systems: saturated water storage (PS10 and PS20), indirect oil thermocline TES (Solar One), indirect two-tank molten salt TES (Solar Two, Gemasolar). Four central receiver systems sizing 100 MW each are under construction in the USA (Ivanpah facility, Crescent Dunes project).

Concluding, central receiver solar power plants are promising, but many technical and economical issues must be overtaken.

1.4.4 Solar dish

Solar dish is a large parabolic mirror that can rotate with two degree of freedom. Each solar dish performs concentration, collection and conversion of the thermal energy to electricity. Radiation hits the parabolic mirror and it is reflected to the focus of the parabola. Here, a Stirling engine is placed. Stirling engine receives concentrated radiation, i.e. concentrated thermal energy, and converts it to work and then to electricity (Figure 1-14). So, each dish generates electricity independently. Power generated by a solar dish CSP plant is exactly proportional to the number of installed solar dishes.

Sun-to-electric efficiency of Stirling solar dish is very high. Optical efficiency ranges 90% because most of radiation is effectively concentrated. Furthermore, Stirling engine is characterized by high 30-40% thermal efficiency, despite of its little size. To optimize it, gases like H_2, He or N_2 are used because they are thermodynamically very efficient. Besides, compared to parabolic trough, there are neither piping losses nor auxiliary consumption. Hence, overall nominal sun-to-electric efficiency is 25-31%, which is great compared to the efficiency of 15-20% of the three CSP systems presented above [5].

Figure 1-14 : Solar dish

Unfortunately, the cost of each parabolic dish is very high and little economies of scale are possible. As a result, solar dishes are of little interest for large scale generation because they are expensive and there are little chances they will become more convenient than other CSP layouts. Solar dishes are instead suitable for stand-alone/off-grid generation of remote communities and for distributed generation. For instance, a single solar dish of 10 m diameter supplies about 15 kW.

1.5 History of CSP plants

Many scientists, such as Ericsson and Mouchout, have studied and developed little thermal solar-driven engines and machines since 1842 [34]. Between 1965 and 1981, professor Giovanni Francia made several experiments on Fresnel linear collectors and was chief of the $1MW_e$ central receiver plant built near Genoa, Italy [35] [36]. However, the first large-scale CSP plant was Solar One, built in the Mojave Desert, California, in 1982 and decommissioned in 1988. Solar One was a successful central receiver test-plant. Just after Solar One went online, the nine Solar Energy Generating Systems (SEGS) parabolic trough plants realized between 1984 and 1991. Afterwards, no CSP plants were built anywhere in the world for several years. It is just in 2006 that Spain started investing in CSP parabolic trough plants, becoming quickly the country with the largest installed CSP capacity (Table 1-1) [27]. Nowadays, the number of plants are under construction is greater than the number of operating plants.

As said, the state-of-art technology is parabolic trough. Although, also linear Fresnel collector and central receiver solar power plants are very attractive for large-scale electric production. Solar dishes are more interesting

for off-grid or distribute production. An overview of the principal parameters of each technology is presented in Table 1-3.

Table 1-3: Principal parameters of CSP systems [37]. 1: Rankine cycle; 2: Stirling engine; 3: with thermal energy storage

Technology	Power (Mwe)	Concentration factor	Nominal efficiency[(1)] (%)	Average efficiency (%)	Load factor (%)	Occupied land surface (m^2/MWh/y)
Parabolic trough	10-200	60-80	21[(1)]	10-15[(1)]	25-70[(3)]	6-8
Fresnel	10-200	25-100	20[(1)]	9-11[(1)]	25-70[(3)]	4-6
Central receiver	10-100	300-1000	20[(1)]	8-10[(1)]	25-70[(3)]	8-12
Parabolic dish	0,01-0,04	1000-3000	31[(2)]	16-18[(2)]	25	8-12

CSP counts in the world 1,9 GW of installed operative capacity. The list of the biggest plants for each technology is presented in Table 1-4. Most of plants are Spanish parabolic trough systems which have gone online since 2010.

Table 1-4: List of operating CSP plants. PB: parabolic trough; CR: central receiver; ISCC: Integrated Solar Combined Cycle [27]

Capacity [MW]	Name	Location	Country	Technology type	Inauguration
354	SEGS	Mojave Desert	USA	PB	1984-1989
150	Solanova	Sanlucar	Spain	PB	2010
150	Andasol	Guadix	Spain	PB	2008-2011
150	Extresol	Torre M. Sesmero	Spain	PB	2010-2012
100	Manchasol	Alcazar de San Juan	Spain	PB	2010-2011
100	Valle	San José del Valle	Spain	PB	2011
100	Helioenergy	Ecija	Spain	PB	2011-2012
100	Aste	Alcazar de San Juan	Spain	PB	2012
75	Martin Next Gen.	Indiantown	USA	ISCC	-
64	Nevada Solar One	Nevada	USA	PB	2007
31	Puerto Errando	Murcia	Spain	Fresnel	2009-2012
20	Planta Solar (PS20)	Seville	Spain	CR	2009
19,9	Gemasolar	Fuentes	Spain	CR	2011
1,5	Maricopa Solar	Poria	USA	Solar Dish	2010

Besides of the 1,9 GW of installed capacity, other 2,5 GW are under construction (Table 1-5). Leading countries are USA, Spain as well as other countries like Israel, China, South Africa and Arab Emirates. Parabolic trough

remains the most deployed system yet big central receiver plants are under construction; for example, the 370MW Ivnapah facility, California.

Table 1-5: List of CSP plant under construction. PB: parabolic trough; CR: central receiver [27]

Capacity [MW]	Name	Location	Country	Technology type	Expected inauguration
370	Ivanpah	San bernardino	USA	CR	2013
280	Solana	Gila Bend	USA	PB	2013
280	Mojave Solar Pr.	Barstow	USA	PB	2014
250	Genesis Solar	Blythe	USA	PB	2014
121	Ashalim power st.	Negev Desert	Israel	PB	2013
110	Crescent Dunes	Nye Country	USA	CR	2014
100	Shams	Abu Dhabi	Arab Emirates	PB	2013
100	Termosol	Navalillar de Pela	Spain	PB	2013
100	Khi Solar One	Upington	South Africa	PB	2014
50	Nokh	Nokh	India	PB	2013
50	Erdos	Hanggin Banner	China	PB	2013
50	Delingha	Delingha	China	CR	2013
12	Alba Nova	Corsica	France	Fresnel	2013

Locations suitable for CSP plants are theoretically capable of powering the entire world. Projects, like Desertec, are studying the installation of many CSP plants in Northern Saharan desert: electric supply which overcomes local consumption is transferred to Europe countries through very high voltage subsea connections [38].

Figure 1-15: operating (blue) and under construction CSP plants (yellow) in the world [27]

2 Thermal energy storage

Recent CSP plants are equipped with thermal energy storage (TES). At mid-day hours much thermal energy is available. In these conditions, the power block works at nominal power and extra thermal energy is stored in a TES. Here, a storage medium manages to absorb thermal energy cooling down the HTF. During low radiation hours or cloudy weather, thermal energy is withdrawn from the storage medium to drive the power block. Thus, TES manages to smooth the mismatch between radiation availability and electric demand and it avoids the stop of the plant due to solar intermittency. As a result, equivalent working hours of the plant are increased. It has been also demonstrated that the Levelised Cost of Electricity is decreased when a CSP plant is equipped with a correctly-sized TES.

There is a mismatch between solar availability and electric consumption (Figure 2-1). Thermal energy storage allows to store solar energy as thermal energy and to use it later on, when electrical consumption is maximal. Also, electrical production during peak load periods is more valuable. Summing up, dispatchability of electrical supply is the main advantage of CSP plant compared to other renewable technology; TES systems are fundamental for the succeeding of CSP plants.

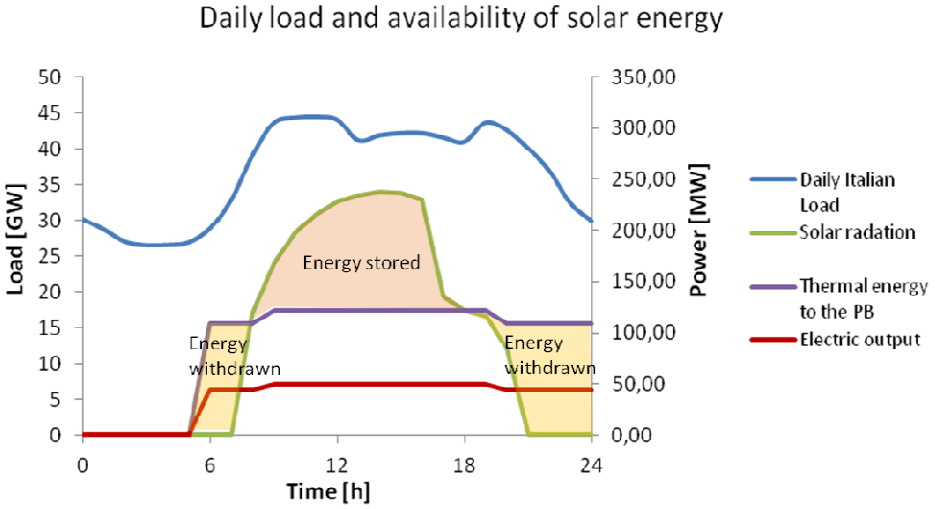

Figure 2-1: Average daily Italian electric [39] consumption compared to the availability of solar radiation

When designing thermal energy storage, several aspects issues are considered. Thermal storage must have a certain thermal capacity, in order to store a determined amount of energy. For example, a TES could be sized to cover cloud passage only. Alternatively, TES can be much bigger to extend power supply to nighttime. Further, thermal energy is collected and stored at high temperature; it

is desirable to efficiently maintain this temperature in the TES for sufficient time, so heat is withdrawn still at high temperature. However, one of the most important parameter is cost-benefit.

Thermal energy storages are classified in sensible, latent and chemical systems. In sensible storage, heat is stored by changing the temperature of a storage medium, i.e. by changing its internal energy. In latent storage, thermal energy is stored in a changing phase medium. Finally, in chemical storages, heat is stored making reversible endothermic/exothermic reaction happen (Figure 2-2).

Sensible storage is further classified in passive, active indirect and active direct storage. In passive storage the HTF flow inside the storage, which is rather a regenerator. This regenerator is both heat exchanger and TES and storage medium is either a solid material or a phase change material (PCM). In active indirect storage systems the HTF flowing in the solar field transfers collected heat to a second liquid storage medium. This storage medium is a different fluid stored in a tank. When heat is stored or withdrawn, the liquid storage medium is pumped next to a heat exchanger where heat transfer with the HTF takes place. It is called active because the storage medium is physically displaced towards the heat exchanger, in contrast with passive where the HTF flows in the solid storage medium. Finally, in active direct storage the HTF is also the storage medium and it is directly stored in TES system when extra thermal energy is available.

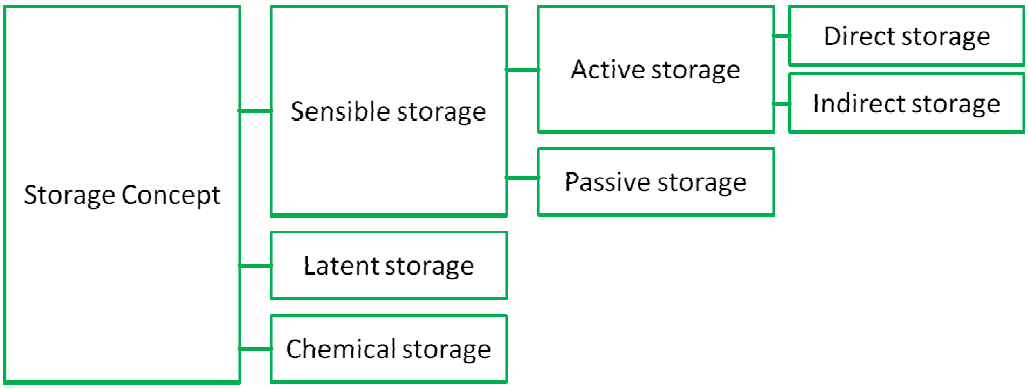

Figure 2-2: Thermal energy storage concepts

All of these TES layouts have been studied and/or realized. The developed systems together with the most promising systems are:

a) Sensible storage
   - Indirect two-tank system
   - Direct two-tank system
   - Direct thermocline system
   - Passive storage

b) Latent storage
c) Chemical storage

Further, each of those systems is briefly presented.

2.1 Thermal energy storage media

The choice of the storage medium is fundamental in the design of TES systems. Certain characteristics are required for storage medium. For instance, high specific thermal capacity is preferred because much energy is stored in little mass of storage medium. This limits the dimension and the cost of the storage. Also, the storage medium must be chemically/physically stable and it may stand many cycles of charge/discharge reversibly. This last parameter determines the lifetime of the storage medium. Besides, the storage medium must be compatible with the tank where it is stored, as well as with pipes, valves, pumps and, eventually, the HTF-to-storage medium heat exchanger. The storage medium should be environmentally benign, not flammable and not toxic. Substances with good heat transfer coefficient are to be preferred because heat transfer is performed more efficiently. Summing up, only few substances satisfy those characteristics and can be used for TES in CSP plants.

Until now, three main candidates have been tested for sensible TES systems in large-scale CSP plants [3][40]: steam, mineral/synthetic oil and molten salt. Other materials as concrete, air, ceramic, and sodium are considered as possible candidates, but they did not find large-scale application yet (Table 2-1). Steam is used in Direct Steam Generation (DSG) systems but only little storage are possible; for example for cloud passage or for supporting the turning-off procedure of the power block. Oil has been occasionally used in first plants as storage medium, but it is dangerous and expensive and it has recently been replaced by molten salt. Finally, molten salt offers the chance for great reduction of costs of TES systems, especially if employed in active direct storage systems. An overview of these three substances is presented.

Table 2-1: Characteristics of some possible storage media [3]

Material	Temperature range [°C]	Density [kg/m3]	Specific heat [J/kgK]	Total heat [MJ/m^3]
Water (1atm)	0-100	1000	4190	419
Molten salt	120-600	1680	1560	1043
Liquid sodium	100-760	750	1260	520
Cast iron	<1100	7200	540	2138
Aluminum	<650	2700	920	1366
Rock	-	2600	890	1271

2.1.1 Steam

Steam is employed in Direct Steam Generating (DSG) systems. In these CSP plants, steam flows directly in the solar field, is heated up and then sent to the power block, eventually after being superheated.

Steam is cheap and stable at high temperatures. Steam has no temperatures limitation because there are no problems of molecular stability; failure of materials happens before steam dissociate in hydrogen and oxygen.

Long term active direct storage at reasonable costs is not possible for DSG. Steam has very low density and the storage would need huge volumes. Usually, saturated water-steam storages are implemented to exploit the high vaporization heat of water. However, these storages are sized to only cover cloud passages (0.5-1h). Concluding, steam is very cheap and suitable for Direct Steam Generation in Fresnel or central receiver plants with little TES system.

2.1.2 Mineral/synthetic oil

The most employed HTF is mineral/synthetic oil although it is expensive and potentially dangerous. Oil is being used as HTF in the biggest parabolic trough CSP plants of the world like Extresol, Andasol, Nevada Solar One, SEGS, etc.

Oil is a good heat transfer fluid: it has good thermal properties such as thermal conductivity and specific heat; it has low viscosity and pumping consumption is contained.

Disadvantages concern mainly instability at high temperature, its harmfulness and its cost. Oil is heated until a certain critical temperature: above it, oil cracks. As a consequence, maximal temperature of the oil is limited. Typical employed oil is Therminol VP-1, which is an eutectic mixture of diphenyl oxide and biphenyl. Cracking temperature is at about 400°C. Therminol VSP-1 is never heated above 393°C in CSP plants and the power block works below this temperature. Another problem is that oil must be kept under pressure. At 393°C oil has a high vapor pressure and to avoid excessive formation of vapor the solar field is pressurized at 20-40 bars, which requires accurate design of the parabolic collectors. Also, freezing protection operation is required because oil freezing temperature is 15°C; however, it is occasionally activated only during winter nights [41].

Oil is harmful, flammable, toxic, polluting and very expensive (2€/kg). Due to its high costs, it is not convenient to be used as thermal energy storage medium. An example of oil TES system is the two-tank direct active TES system of SEGS I, 3h of full-load storage capacity. The cost of oil is the main share of the TES installation cost; also, the two tank are very expensive as they are pressurized [42]. Concluding, it is more convenient to store heat in a low cost material, such as molten salt. This is why in recent CSP plant oil is not anymore used as storage medium.

2.1.3 Molten salt

Molten salt is the third possible candidate as storage medium in CSP plant. Molten salts are very attractive as they are very cheap and they are stable up to 500-600°C [41]. Hence, operating temperature of the CSP plant can be raised to higher values. This increase in temperature is beneficial for both the power block and the thermal energy storage system. At the power block, thermal efficiency is improved. At the TES, larger temperature rise allows to store much more energy in littler amount of molten salt.

Three main molten salts are identified as suitable to be used in CSP plants: solar salt, Hitec and HitecXL. These molten salts are mixtures of nitrate and nitrite compounds. Potassium, calcium or sodium nitrates are the commonest salts. The composition and relevant physical properties of those three salt compounds are presented in Table 2-2. Summing up, molten salts are very attractive choice as thermal energy storage medium.

Table 2-2 : Molten salt and Tehrminol VP-1 physical properties [41]

Salt	Solar Salt	Hitec	HitecXL	Therminol VP-1
Composition [%]				biphenil/ diphenyl
$NaNO_3$	60	7	7	
KNO_3	40	53	45	
$NaNO_2$		40		
$Ca(NO_3)_2$			48	
Maximum temperature [°C]	600	535	500	400
Freezing temperature [°C]	220	142	120	13
Density @ 300°C [kg/m^3]	1899,2	1864,8	1992	815
Heat capacity @ 300 °C [J/kgK]	1391,4	1561,7	1447	2319

Molten salt is not toxic, not flammable nor polluting. Also, vapor pressure is very low also at high pressure; typically it is a fraction of Pascal [40]. Thus, operating pressure is of only few bars in order to prevent air infiltration in pipes or tanks. The main disadvantage of molten salt is the high freezing temperature, which is between 120°C and 220°C. Freezing is undesirable as it can damage pipes, storage, pumps, valves and other equipment. Also, re-melting frozen molten salt is quite complex. CSP plants using molten salt implements freeze protection operations and they are equipped freezing recovery systems. Also molten salts are corrosive and they could potentially damage valves, pipes, pumps, etc. Materials in contact with molten salt must be compatible in order to minimize corrosion. Large scale plants using molten salt have already

implemented, demonstrating the feasibility of handling corrosion and freezing issue.

Molten salt were used for the first time as HTF and thermal storage material in Solar Two plant. Here, molten salt blend “solar salt” was employed. Solar salt is stable below 600°C, and in Solar Two it has operated between 565°C and 290°C. The TES fared well, demonstrating the feasibility of molten salt active direct TES systems [42].

As solar salt freezing temperature is very high (200°C), other molten salt blends have been researched. Hitec and HitecXl are two blends of molten salt with low freezing temperature. Those mixtures include sodium nitrite and calcium nitrate. Their special compositions result in low freeze temperatures, respectively of 142°C and 120°C. Freezing protection operation is still required, but freezing issue is easier to handle than in the solar salt case. Hitec and HitecXL are stable below 535°C and 500°C, which is less than solar salt (600°C) [40]. However, temperature raise is still great compared to the oil case.

Concluding, molten salt use in CSP plants is very attractive. Thermal energy storage in molten salt is cheap and demonstrated technologically feasible. Molten salts are designed to be stable at very high temperature (500°C – 600°C). Compared to water and oil the maximal temperature of the heat collected at the solar field is sharply raised. A further increase in temperature is hindered by technological issues, such as materials resistance and corrosion because of high temperatures. Also, special freezing protection operations and recovery systems are necessary to avoid solidification of the salt. Despite of these two disadvantages, molten salt offers the chance to lower the cost of the thermal energy storage and to raise the maximal temperature of the power block, increasing its efficiency.

2.2 Indirect Two-Tank TES system

Active indirect sensible two-tank TES system is characterized by two tanks, one containing hot storage medium and the other one cold storage medium [42][43]. This system is indirect, which means that the HTF is a different fluid than the storage medium. Those two fluids are never in direct contact and heat transfer between them is performed through a HTF-to-storage medium heat exchanger. When heat is stored, the storage medium leaves the cold tank, is pumped to the heat exchanger and it is heated up by the HTF. Then, it is stored in the hot tank. When heat is withdrawn, the inverse process takes place.

Two-tank systems are low-risk and heat is efficiently withdrawn steadily at high temperature until the hot tank is emptied. This system is widely employed in CSP applications, and it is considered the state-of-art thermal energy storage (Figure 2-10).

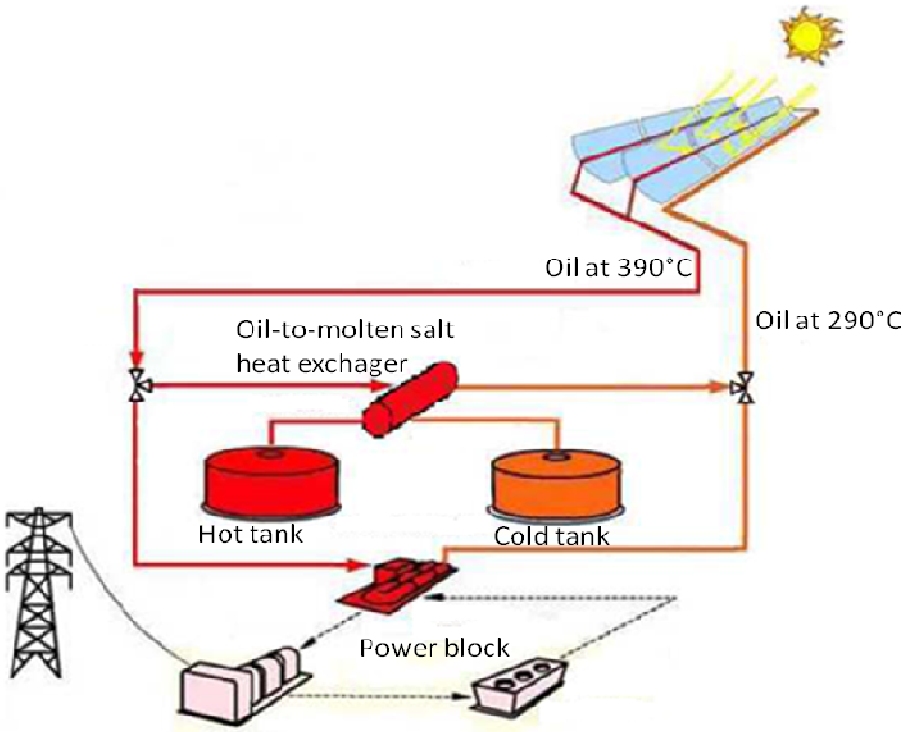

Figure 2-3: CSP equipped with an Indirect Two-Tank TES system

Examples of two-tank indirect storage systems are the CSP plants of Eextresol I-II and Andasol I-II. Extresol I has been inaugurated in 2009 at Torre de Miguel Sesmero, Spain. It is a parabolic trough plant with synthetic oil HTF. The storage is molten salt two-tank system sized to drive the power block for 12h at nominal power.

Andasol is another parabolic trough system (Guadix, Spain) (Figure 2-4). Andasol is placed on a plateau at about 1000 meter on the sea level. Here, scattering of radiation is decreased; also, the site enjoys good sunny weather for most of the year and available annual normal radiation reach easily 2000 kWh/m^2. In Andasol I, synthetic oil is used in the solar field at a temperature ranging 290°C – 390 °C. TES is a molten salt indirect two-tank system sizing 7.5h of full-load storage capacity. The temperature of the hot tank is 384 °C and the temperature of the cold tank is averagely 291 °C. Each tank sizes 37 meters of diameter and 14 meters of height. Annual average sun-to-electric efficiency is 14,7%.

Indirect storage is usual the TES system of parabolic trough. In this system, oil is used as the HTF and molten salt as storage medium. The use of molten salt in the parabolic trough solar field requires particular attention because molten salt would freeze during nighttime. Particular freezing protection, such as gas or electric heaters, is required; alternatively, recirculation of stored warm molten salt in the solar field is performed. The only example of

molten salt parabolic trough is the 5 MW plant Archimede, Italy [44]. However, if molten salt are used in the solar field, direct storage is rather preferred because no expensive HTF-to-storage medium heat exchanger is needed, as explained in section 2.3.

Figure 2-4: Andasol I and II. Power block and two-tank TES system surrounded by hectares of parabolic trough concentrators

2.3 Direct Two-Tank TES system

In direct storage systems the HTF is directly stored. When extra radiation is available, cold HTF leaves the cold tank of the two-tank storage [43][42]. Cold HTF is heated up in the solar field and then stored in the hot tank. When heat is withdrawn, hot HTF leaves the hot tank and it is pumped to the steam generator of the power block, cooling itself down. Then, it is re-injected in the cold tank (Figure 2-5).

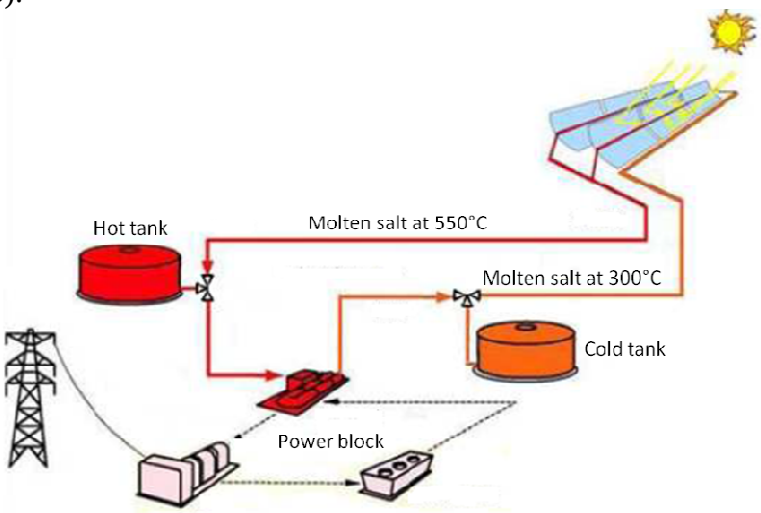

Figure 2-5: CSP equipped with a Direct Two-Tank TES system

Two tank active direct molten salt system has been employed with success at Solar Two Plant (Dagget, California, Figure 2-6) and Gemasolar (Seville, Spain). Both those systems are central receiver plants. Solar two worked between 1995 and 1999. Nominal power was 10 MW. Solar Two was the first CSP plant using two-tank direct thermal storage. The TES system had a 3-hours full-load capacity storage. Power generation during cloud passages and nighttime succeeded with great thermal efficiency (19%) and great storage discharge efficiency (97%); discharge efficiency is defined as the ratio of the amount of thermal energy injected in the hot tank and the amount of thermal energy withdrawn from the hot tank. High thermal efficiency was due to high operating temperature ranging 565 °C and 290 °C (solar salt). High discharge efficiency is so high because heat is injected and withdrawn at the same temperature (565 °C); efficiency is below 100% because a little amount of heat is lost to the environment.

Gemasolar (previously called Solar Tres) is a 19,9 MW central receiver plant completed in 2008. As Solar Two, Gemasolar uses solar salt between 565 °C and 290 °C. Solar field is sized to supply up to 120 MW of thermal power and its double-tank molten salt active direct storage is sized to supply the power block for 15 h without any solar radiation; so, 24 h per day electrical production is realized during summer. The equivalent working hours of this plant are about 6500 h per year, i.e. a capacity factor of about 75%.

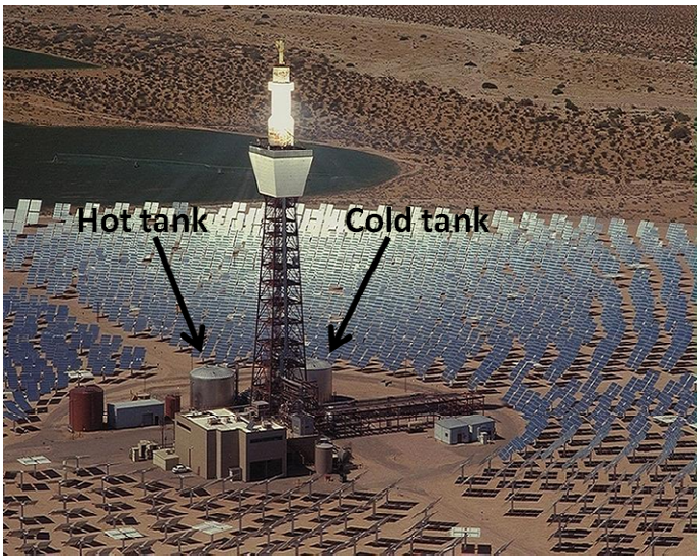

Figure 2-6: Solar Two, Mojave Desert, California. Two-tank TES is visible next to the tower

Another interesting example is SEGS I, the first of the nine parabolic trough plants installed in Mojave Desert, California (Figure 2-7). With 354 MW of nominal electric output, SEGS plant were built between 1984 and 1989 but it is still the biggest CSP facility in the world. The two-tank active direct storage

used in SEGS I directly stores the synthetic oil flowing in the parabolic trough solar field. The cost is very relevant because of the big quantity of oil required. It has been estimated that oil was responsible of 42% of the investment cost. This is why, SEGS I is the only plant in the world equipped with such TES system and why this kind of storage has not been repeated. Also, storage at high temperature cause high vapor pressure of the oil. As a consequence, tanks must be pressurized and, due to their dimension, their cost is very high.

Figure 2-7: SEGS facility, Mojave Desert, California

2.4 Direct Thermocline TES system

In a thermocline TES system HTF is stored at the top of the tank while cold storage medium remains at its bottom. The zone between the hot and cold regions is characterized by big temperature gradient, which is called thermocline: this is why one-tank storage is commonly said thermocline storage. As density of the fluid changes with temperature, buoyancy forces help keeping the thermal stratification. For this reason, there is no free convection and heat is transferred from the top of the tank to the bottom only via conduction [43][42][1].

Extra solar thermal energy collected at the solar field is stored in the thermocline tank. During the charging process, the HTF enters from a port located on the top of the tank. The HTF slowly flows through the packed bed displacing cold molten salt and heating up the packed bed. At the exit port located at the bottom of the tank, the HTF is completely cooled down. Reversely, when the tank is discharged the cold HTF slowly enters from the bottom port and it heats itself up flowing through the warmer packed bed. Hot HTF is displaced and leaves the tank form the upper port. At the exit port, the hot HTF flows toward the power block to drive it.

The tank can be divided in three zones. There is a lower region, where the storage medium is cold. There is an intermediate thermocline region, where there is a high temperature gradient. And finally, there is an upper region, where the storage medium is hot (Figure 2-8). During charging process, heat is stored and the upper hot region expands. As a consequence, the thermocline region moves from the top of the tank towards the bottom, shrinking the lower cold region. Reversely, when heat is withdrawn from the tank, cold HTF is injected, the thermocline moves towards the top of the tank and the hotter region shrinks.

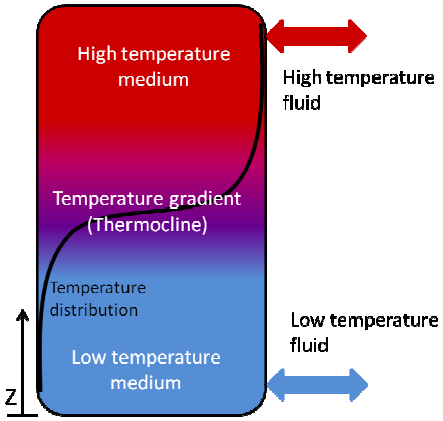

Figure 2-8: Schematization of Thermocline TES system

However, the only active direct thermocline thermal energy storage built is the 180 MWh_{th} TES system of Solar One, which was working with mineral oil. Solar One was the first large-scale CSP power plant, built in Dagget, California and it operated between 1982 and 1988. Solar One was a power tower system and mineral oil was used as both HTF and heat storage medium. Due to mineral oil, temperatures were limited and overall sun-to-electric efficiency was about 16%. The plant was a breakthrough because 8 h continuous electric generation was achieved during the summer [44].

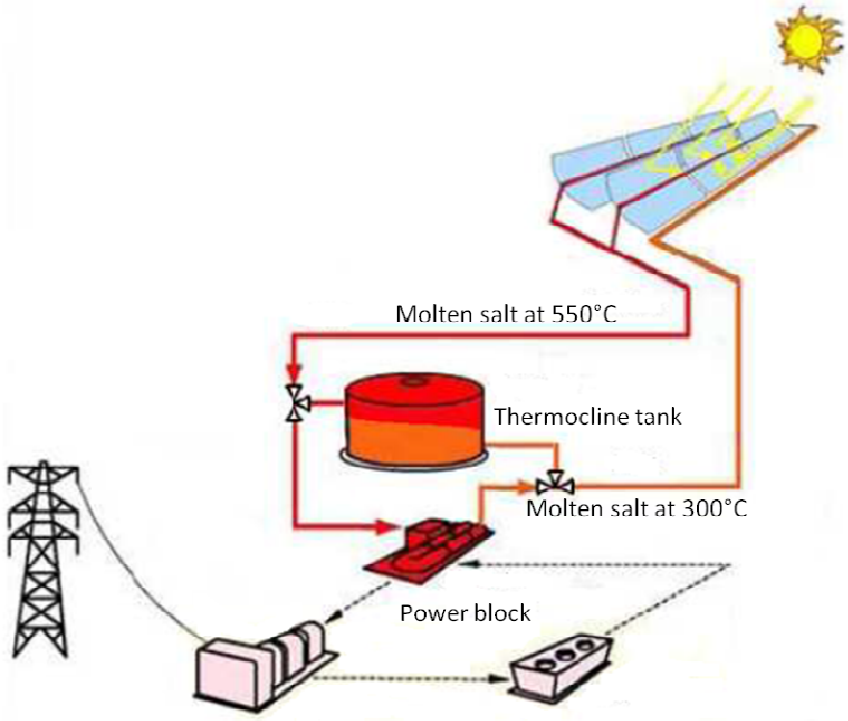

Figure 2-9: CSP plant equipped with direct thermocline TES system

Another example is the thermocline installed in the 30 MW CSP plant of Puerto Errado 2, Spain. The facility is a DSG plant with Fresnel concentrators. This plant is equipped with direct Ruth single-tank thermocline storage of 0,5 hours full-load capacity. The storage arranges steam buffering, covers cloud passages and supply steam during the turning off transient of the power block [44].

2.5 Passive storage

In passive storage, the HTF flows in an immobile storage material, which is usually solid [43][42]. Many tubes pass though the storage performing heat transfer. Heat transfer rate depends on the number and the diameter of the tubes in the solid body. Usually, the heat transfer rates are quite high. Passive storage behaves as regenerators, which is at the same time storage and heat exchanger (Figure 2-10).

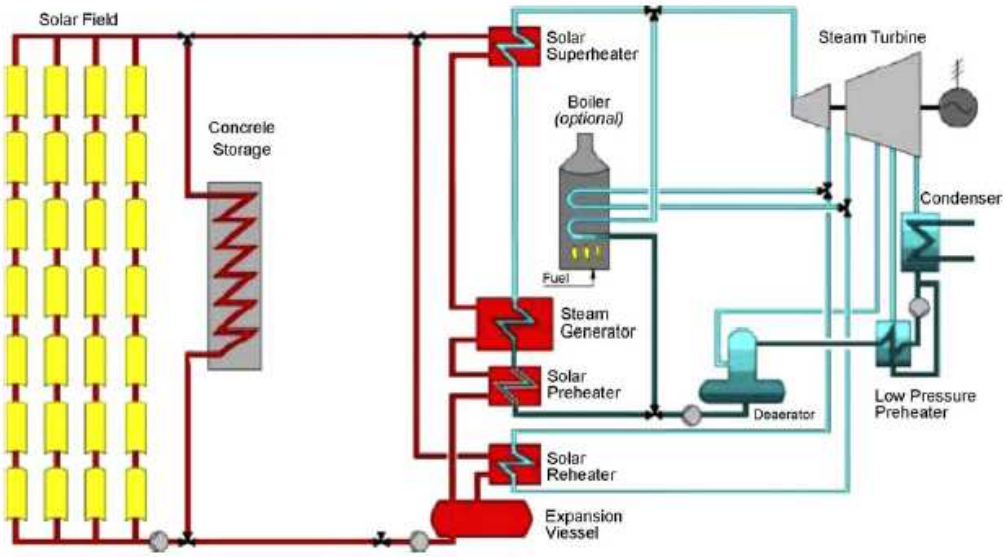

Figure 2-10: CSP plant equipped with a passive TES – concrete storage [43]

Passive storage is a promising low-cost TES system. Materials used are solid material like concrete, castable materials and phase change materials. Those materials are very cheap, available in bulky quantities and they are easy to handle. Besides, those materials have good thermal properties and they are enough stable for TES application.

Unfortunately, heat cannot be withdrawn steadily at high temperature. Indeed, the HTF flowing inside the solid passive storage leaves the storage at a temperature which decreases as the passive storage cools down. This hinders their utilization is CSP plants, because one of the most important requirement is the possibility of withdrawing heat at nominal temperature for the longest time possible. This requirement is dictated by the power block, which works efficiently when driven by heat at constant nominal temperature. An alternative solution would be a latent passive storage. In this case, the passive storage medium release heat at constant temperature during the phase changes of the storage medium. However, passive storage TES systems are still little development and no breakthrough are forecast in near term.

A passive system has been tested with success at Plataforma Solar de Almeria in between 2001 and 2006 with the collaboration of German company DLR. Concrete blast furnace cement was used with iron oxides, ashes and other materials in minor quantities. Also, other tests were made using ceramic materials. Storage size was 350kWh and temperatures of 325°C were attained in 160 thermal cycles. The test fared well for both concrete cement and ceramic. Especially, contact between the HTF tubes and the concrete matrix was still close and no signs of degradation were reported. This ensures good heat transfer even after several thermal cycles. Concrete was found to be the best choice,

basically because of its lower cost. Although, in some cases development of cracks in the solid matrix were observed [42].

Concluding, passive storage certainly offers the chance for reducing the costs of thermal energy storage. However, passive storages are not mature yet and the drop in temperature due to the cooling of the storage during discharge hinders passive storage to be used in CSP plants.

2.6 Latent TES system

Energy associated to a phase-change is called latent energy. More in detail, energy required to pass from solid to liquid and from liquid turning to gas is called respectively heat of fusion and heat of vaporization. Thermal energy associated to the phase change is called latent energy[42][43].

In latent thermal energy storages thermal energy is stored and withdrawn almost isothermally. Also, temperature storage might be controllable by changing the pressure of the storage medium. Liquid-solid transition is preferred because heat transfer coefficients of liquids and solids are several times higher than those of vapor substances. Hence, heat transfer is performed more efficiently by liquid and solid substances. Also, the change in volume from liquid to vapor is consistent and complicate to handle.

Latent energy storages are of little size because specific latent thermal energy is very high compared to specific sensible heat. For instance, heat of fusion and of vaporization of water are respectively 334 kJ/kg and 2272 kJ/kg, while water heated of 1°C absorbs only 4.18 kJ/kg of heat.

Thanks to the experience of decades in the thermoelectric power production with fossil fuels, little saturated steam direct thermal storages are implemented in DSG plants. Here, steam generated is directly stored in a pressurized tank, where steam is at equilibrium with liquid water. This help reducing the size of the storage, as heat vaporization is exploited and as water has great thermal capacity compared to steam. At the exit of the storage, steam is saturated. If superheated steam is needed, a second TES must be connected to the exit of the steam accumulator. However, this saturated steam storages are able to meet only little mismatch between steam production and electric output.

Examples of saturated steam storage are present in the DSG plant PS10 (Seville, Spain) and in linear Fresnel concentrator facility of Alba Nova I (Corsica). PS10 is a tower power system. Saturated steam from the central receiver is accumulated in a 45-bar pressurized reservoir. To improve thermal capacity of the reservoir, steam and water immersed in a ceramic alumina packed bed. Thermal storage has a capacity of 20 MWh_{th} and it has a discharge efficiency of 92,4%. This storage is though as buffer storage and it can drive the power block only for half an hour [42].

Another example is the CSP plant of Alba Nova I, 12 MW of nominal power, which will be inaugurated in late 2014 in Corsica. This plant has a solar field of Fresnel collectors and it is equipped with saturated water storage, as in the PS10 case, but there is no alumina packed bed. Also here, storage is sized for only 1h full-load capacity only (Figure 2-11) [42].

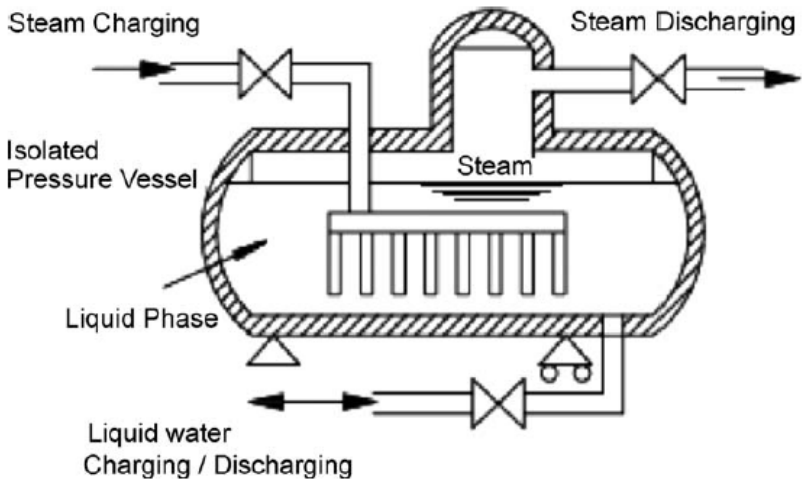

Figure 2-11: Saturated steam TES system [43]

Indirect latent TES systems are good candidates for large TES capacity but their design is complicate and selection of storage medium is difficult. Some experiments on molten salt with low melting point have been performed but results were quite poor. Indeed, molten salts became instable after few thermal cycles. Many efforts are addressed towards the development of latent thermal energy storage, but any breakthrough is forecast in the near future. Summing up, latent energy storage is nowadays not enough developed for CSP plants.

2.7 Chemical thermal energy storage

In chemical systems thermal energy is stored through reversible chemical reactions. When thermal energy is available, an endothermic reaction is induced. For example, a chemical specie is dissociated and this reaction absorbs heat, storing it. When heat needs to be withdrawn, the inverse reaction of synthesis is induced; the chemical specie is exothermically synthesized and heat is released. Obviously, the process must be perfectly reversible.

Chemical heat storages are very promising for the future, but they are nowadays almost undeveloped. Storing energy in chemical reactions offers great specific energy density and storage size is contained. Besides, heat is steadily stored for long periods at ambient temperature. Chemical storage is very attractive for long term studies, as it can significantly reduce the costs of thermal energy storage systems.

2.8 Thermal energy storage cost assessment

One of the main problems hindering CSP diffusion is the high specific cost of 3500 – 5000 € per kW installed[5]. Research is addressed in finding how to reduce this high cost. From the breakdown of costs (Figure 2-12)[5], the solar field is assessed to be the most expensive component of the plant, costing 40-50% the entire installation cost. Other big expenses are the power block (15-20%), the thermal energy storage (TES) (15-20%), engineering costs (10%) and other costs (10-15%). So, TES is one of the biggest share of CSP overnight cost system. The considered storage is a two-tank system, which is the state-of-art technology: it is low-risk, largely employed but costly. However, there are chances for sharp cost reduction.

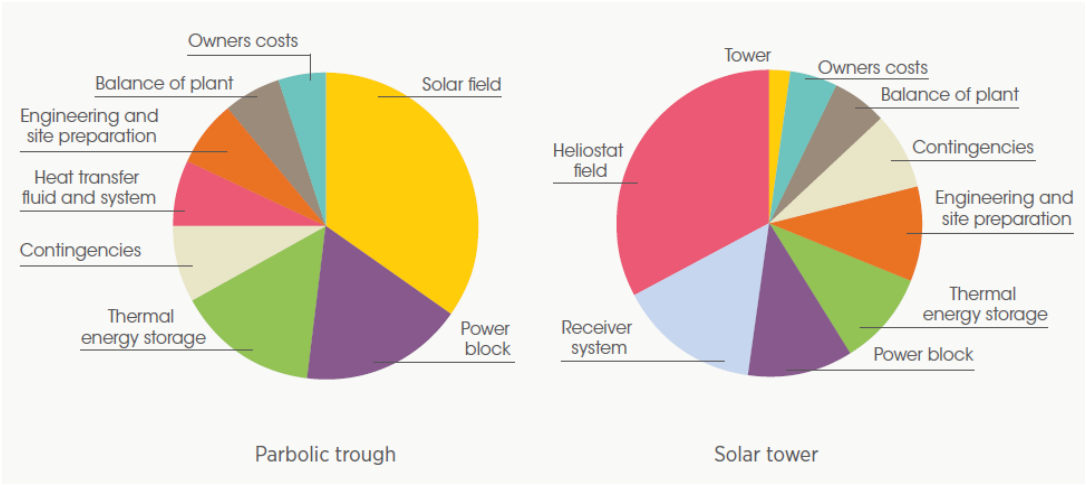

Figure 2-12: CSP Cost Breakdown [5]

Active direct molten salt thermocline TES is assessed to be cheaper than direct and indirect state-of-art TES for several reasons. First it is a direct storage: higher temperatures are reached limiting the size and the cost of the storage. Second, thermocline is very cheap because it can be filled with low-cost filler materials and besides just one tank is required, instead of two. Each of these advantages is discussed.

Direct molten salt storage requires littler tank and less storage medium than indirect systems. Indeed, temperature is limited to 390°C in indirect TES systems because synthetic oil cannot be heated above 390°C, or it would crack [40]. In direct systems, instead, molten salt is used as both HTF and storage medium and temperatures up to 565°C are attaint[42]. So, storage medium temperature rise is about 250°C in direct systems versus the only 100°C of indirect systems; as a consequence, in direct systems much more heat is stored in much less molten salt.

Thermocline tank is often filled with a low-cost solid material which is immersed in the liquid storage medium. This is economically convenient as the low-cost solid material replaces more expensive liquid storage medium. This low cost material occupies most of the tank and it acts as primary thermal storage.

Storage cost in oil, solar salt, Hitec, and HitecXL is compared: direct thermal energy storage in solar salt is the cheapest choice, especially if a packed bed is put in the thermocline (Table 2-3).

Table 2-3: Molten salt and Therminol VP-1 storage cost [40]

Salt	Temperature Rise [°C]	Cost per kg [$/kg]	Specific heat [J/kgK]	Storage Cost [$/kWh$_{th}$]
Hitec, Direct	200	0,93	1561	10,7
HitecXL, Direct	200	1,19	1447	14,8
Solar Salt, Direct	250	0,49	1391	5,1
Solar Salt and quartzite rock, Direct	250	0,14	970	2,1
Solar Salt, Indirect	100	0,49	1391,4	12,7
Therm. VP-1, Indirect	100	2,2	2319	34,2

Hitec or HitecXL thermal energy storage is much more expensive then when using solar salt. All salts have similar physical properties (c_p) but the cost of Hitec and HitecXl is much higher than solar salt one (0,93 – 1,19 $/kg versus 0,49 $/kg) [40].

Compared to indirect case, direct storage in solar salt is 2.5 times cheaper because of the 2.5 times higher temperature rise. Indirect storage in solar salt costs 12,7 $/kW$_{th}$ while direct storage in solar salt costs only 5,1 $/kW$_{th}$. Also, if a packed bed is put in the thermal energy storage, costs are further reduced. Indeed, packed bed of quartzite rocks/silica sand occupy 78% (porosity) of the volume of the storage, and their cost is about 0,07 $/kg [1]. The cost of the molten salt – packed bed mixture is evaluated to be 0,14 $/kg (eq. (2.1)). Direct storage in solar salt and quartzite rocks/silica sand packed bed is assessed to be the cheapest choice (2,1 $/kW$_{th}$).

$$Cost/kg = \frac{0{,}78 * 70\frac{\$}{ton} * 2{,}5\frac{ton}{m^3} + 0{,}22 * 0{,}49\frac{\$}{kg} * 1{,}8\frac{ton}{m^3}}{0{,}78 * 2{,}5\frac{ton}{m^3} + 0{,}22 * 1{,}8\frac{ton}{m^3}} = 0{,}14\ \$/kg \tag{2.1}$$

Concerning indirect storage in oil, it is assessed to be from 2 to 7 times more expensive compared to direct storage in molten salt. Oil specific thermal capacity is 50% higher than molten salt one but the temperature rise of oil is

2/2,5 less. So less energy is stored in a kg of oil than in a kg of molten salt. Besides, the cost per kg of oil is 2-4 times more expensive then molten salts. As a consequence, the cost per kWh_{th} stored in oil is between 2 and 7 times higher than in molten salt. Oil is confirmed to be a bad storage medium because of its high cost and little temperature rise [1].

Another advantage of active direct thermocline TES systems is that the TES require only one tank. The volume of this tank is marginally larger than the volume of one tank of the two-tank system. This is explained in the following way: during the discharge process of a two-tank TES system, the storage medium leaves the hot tank and it is collected in the cold one. When the hot tank is empty, the cold tank is full. Hence, the tanks of a two-tank system are both capable of storing the whole amount of storage medium. As a result, tank cost is much reduced in thermocline system [1].

Another advantage of direct storage is that no expensive oil-to-salt heat exchanger is needed. This device costs about 20-30% the whole cost of indirect TES systems [1][45].

The cost of indirect two-tank systems, direct two-tank systems and direct thermocline system are compared in Table 2-4. Energy stored is proportional to density, specific heat and temperature rise (eq. (2.2)). So, high density, specific heat and temperature rise allow storage in littler and less expensive tanks:

Table 2-4: TES cost comparison [1][42][3]

	Indirect two-tank (a)	Direct two tank (b)	Direct two-tank (c)	Direct Thermocline (d)
Storage medium	Solar Salt	Synthetic oil – Therminol VP-1	Solar Salt	Solar Salt and quartzite rock/silica sand
Medium cost [$/kWh$_{th}$]	12,7	2,2	0,49	0,14
Temperature rise [°C]	100	100	250	250
ρc_p[MJ/m^{3}K]	2,48	1,87	2,48	2,16
PB Thermal conversion [%]	37	37	41	41
Storage capacity [MWh$_{th}$]	1014	1014	915	915
1-Tank storage Volume [m^3]	14700	19500	5300	6100
Tank height [m]	14	14	14	14
Tank Diameter [m]	36,5	42,1	22,0	23,5
Tank Cost [M$]	12,5	16,5	6,0	4,8
Heat exchanger [M$]	5,8	-	-	-
Storage medium cost [M$]	12,8	34,9	4,7	1,9
Total [M$]	**31,2**	**51,4**	**10,6**	**6,9**
Storage technology of:	Andasol	SEGS I	Gemasolar	-

$$Q_{storage} = V\rho c_p \Delta T \qquad (2.2)$$

As expected, molten salt indirect storage (Andasol) is by far a better choice then direct oil storage (SEGS I). Tanks have almost the same cost of 17-18 M$, yet the huge difference in the overall cost is due to the different storage medium: solar salt costs about 12,9 M$, while oil cost is 34,9 M$.

Direct molten storage is remarked to be much more interesting then both indirect molten salt storage and direct oil storage. Storage volume is reduced of three-four times than the two previous cases and overall cost is only 10,6 M$. This kind of storage has been successfully implemented at Gemasolar central receiver plant.

However, direct molten salt thermocline thermal energy storage is even cheaper than this last. Indeed, total storage volume is almost halved because only one tank is required: 6100 m^3 versus 10600 m^3. Also, thanks to the packed bed, the investment in molten salt and quartzite rocks is much cheaper and overall cost is only 6,9 M$.

However, low cost of thermocline TES is paid with worse performance than the two-tank TES. In single-tank case, hot and cold storage medium are stored in the same tank. The hot region lies at the top of the tank while the cold is quiescent at its bottom. Natural thermal stratification is induced because of the difference in density between hot and cold storage medium. However, between the hot and cold layers there is a thermal gradient, which is called thermocline. In this region heat is stored at a temperature which is lower than the maximum temperature, so it is useless for electric conversion. Unfortunately, the thermocline occupies a big share of the tank height due to heat conduction and hot fluid charge-discharge processes: this cause depletion of a considerable quantity of injected heat. Summing up, low cost of thermocline TES is paid with lower performance compared to the two-tank TES [1][11].

Concluding, direct molten salt thermocline offers the possibility for reducing the cost of TES systems, but its performance must be further investigated to evaluate cost-effectiveness of such storage. Thermocline systems requires only one tank, no oil-to-salt heat exchanger and much molten salt are replaced by low-cost filler materials. Also, heat is stored at high temperature reducing the size of the tank and its cost; besides, high temperature allows the power block with greater thermal efficiency. However, large-scale utilization of packed-bed thermocline storage for CSP is hindered by several problems. Performance of a thermocline TES is lower than a two-tank system because most of heat in the thermocline region is considered as useless because not warm enough to superheat the steam of the power block. Thermocline TES system has been little studied, and performance prediction needs further investigations.

2.8.1 Choice of the filler material for molten salt thermocline TES

Quartzite rocks and silica sand have been identified as the best choice as filler material in molten salt thermocline tanks. [1][46][11]. Brosseau et al. proceeded with the screening of several materials. Authors consulted a team of geologists which suggested a set of 17 materials. Isothermal and cyclic thermal tests were carried out on those materials, to understand their behavior and compatibility with molten salt. During the isothermal test, some materials reacted with the salts, others crumbled. Again, some gained weight because they absorbed some molten salt, others partially dissolved in the molten salt. Only 8 materials passed the first isothermal test. Among those, 4 materials were quite rare and they were set apart. After the cyclic thermal test, only quartzite rocks and silica sands held up well. These materials well endured the 554 temperature cycles (several months of tests). Also, these two materials are largely available, easy to handle and cheap. They are the best choice as filler materials in a molten salt thermocline.

3 Previous studies on molten salt thermocline TES systems

In this chapter previous studies and publication on thermocline TES are scanned. Methodology followed by authors is presented and results concerning the correct design of thermocline TES are discussed.

The understanding of the thermal behavior of molten salt thermocline TES systems is fundamental in order to predict CSP plant performances. Indeed, thermocline TES system supplies thermal energy to the power block and it strongly affects the performances of the entire CSP plant. For example, a good thermocline have high discharge efficiency, which means that most of the heat stored in the thermocline can be withdrawn at high temperatures to drive the power block. Also, a good thermocline can remain in standby mode for several hours having little thermal losses to the environment. Thus, a well-designed thermocline TES system is fundamental to achieve high CSP plant performances [1][12][14].

Several factors influence thermocline performances. For instance, high tanks are preferred, as height helps stratification. On the other hand, high tanks are subject to greater thermal losses as the ratio of the surface exposed to the external ambient on storage volume is greater. So, there is a trade-off between discharge efficiency and tank height, and an optimal tank height could be found. Another example is molten salt mass flow rate in the thermocline. Low fluid velocity helps stratification, as thermal exchange between molten salt and packed bed is optimal. At the same time, discharging time is long and the thermocline tends to extend itself due to heat diffusion, compromising thermal stratification. Many other factors influence thermocline development: it is fundamental to understand how they affect the performance of thermocline TES systems [11][12].

Thermocline behavior can be predicted with a numerical model. Many authors developed numerical models of thermocline TES system: these models are easy to develop and results are available in short time. Also, predictions are accurate and it is possible to estimate their degree of precision. Numerical models are cheap, as they do not need any expensive physical asset. Hence, numerical modeling is a suitable methodology for the simulation of thermocline TES. However, comparison with experimental data is necessary to validate the numerical model and to confirm its correctness [1].

In order to develop their numerical models, all authors adopt a similar methodology, which can be divided into four major areas. First, authors identify fundamental equations which govern the problem. These equations are mass conservation, momentum conservation and energy yield for both molten salt and packed bed. Second, these differential equations are solved with a numerical

approach; for example a finite-difference approximation must be used. Third, equations are implemented and coded. Last, results are compared to experimental data to validate the model. Comparison of results with analytical solutions and with real data is indispensable to check the correctness of the model [12][14].

In the next subchapters previous models available are scanned. Advantages and disadvantages of each model are discussed and results of those researches are briefly presented. Afterwards, in chapter 4, a set of fundamental equation is chosen and discretized: a new thermocline TES model is developed and compared with four analytical solutions and with experimental data available in literature.

3.1 Previous thermocline TES models

Authors employed fundamental equations after making some assumptions. Basically, fundamental equations governing the heat transfer between a fluid and a packed bed are Schumann equations [10]. Those are used, for example, by Pacheco et al. [1] and Yang et al. [11]. Other authors use a set of equations which includes several terms neglected in the Schumann equations. For instance, Garimella et al. [14] and Xu et al. [12].

Together with Schumann equations, which describe energy conservation, also momentum and mass conservation are considered, depending on the assumptions made by authors. Two sets of equations have been mainly used, depending on the assumptions made by single authors. Those two set of equations are Schumann equations set and Schumann-Darcy-Brinkman-Forchheimer set.

3.1.1 Schumann equation set

Schumann equations govern energy conservation in the case of a fluid through a porous media [10]. The fluid and the porous media are at different temperatures. Therefore, the system is described by two equations, one for each phase. The first equation accounts the energy yield of the molten salt and it includes internal energy change, advection, diffusion and the heat exchange with the porous medium (3.2). The second equation concerns the energy yield of the porous media and it is composed by internal energy change of the porous media and heat exchange with the molten salt (3.3). Garimella et al. call it “two-temperature equations” because the first equation accounts for fluid temperature while the second for the packed bed one. Velocity is commonly defined depending on the porosity of the packed bed (eq. (3.1)).

$$u_m = u \cdot \varepsilon \tag{3.1}$$

$$\varepsilon\rho_{ms}c_{p,ms}\frac{\partial T_{ms}}{\partial t}+\rho_{ms}c_{p,ms}u_m\ \frac{\partial \mathrm{T_{ms}}}{\partial z}=\frac{\partial}{\partial z}\left(k_{eff}\frac{\partial T_{ms}}{\partial z}\right)+h_v\left(T_{pb}-T_{ms}\right) \tag{3.2}$$

$$(1-\varepsilon)\rho_{pb}c_{p,pb}\frac{\partial T_{pb}}{\partial t}=h_v\left(T_{ms}-T_{pb}\right) \tag{3.3}$$

where ε is the porosity (or void fraction); T_{ms} and T_{pb} represent the temperature of the molten salt and of the packed bed, respectively; $c_{p,ms}$ and $c_{p,pb}$ are the specific heat of the fluid and the filler, respectively; h_v is the volumetric interstitial heat transfer coefficient [W/m^{3}K]. As the surface of contact between molten slat and packed bed is hardly measurable, it is preferred to adopt a heat transfer coefficient which refers to the volume in which the heat transfer takes place. Basically, in an ideal packed bed of identical spheres, the control volume contains a number of spheres which depends on the porosity of the packed bed and on the diameter of the packed bed. Knowing that, it is possible to evaluate the area of thermal exchange per unit of volume, and, hence, it is possible to define a volumetric heat transfer coefficient.

In Schumann equations heat diffusion is accounted only in eq. (3.2). This is because the packed bed is immersed in the liquid matrix and contact between solid particles is poor.

The term $h_v(T_{ms}-T_{pb})$ is present in both equations and it differs only in the sign. This term behaves as a heat source and it couples the two equations. This means that energy extracted from the molten salt is compensated by an equal amount of energy absorbed by the porous media, or vice versa.

Pacheco et al. and Yang et al. used those two equations for their model [11]. Also, they included continuum equation. However, they consider physical properties of both fluid and packed bed were considered as constant and the continuum equation is simplified in:

$$div(\vec{v})=0 \tag{3.4}$$

Momentum conservation is neglected because the flow in thermocline TES systems is very slow (<10^{-4} m/s) and viscous/transient velocity effects are considered as negligible.

Summing up, Schumann equation set includes eq. (3.2), eq. (3.3) and eq. (3.4).

3.1.2 Schumann-Darcy-Brinkman-Forchheimer equation set

Another set of equations includes momentum equation with the Brinkmann-Forchenheimer extension to the Darcy law [14]. This model is more complete and it has the capability of forecasting viscous effects, vortex and transient velocity effects. Also, thanks to Darcy-Brinkman-Forchheimer extension, momentum conservation accounts for the porous-medium resistance.

Together with momentum equation, also continuum conservation for the fluid phase and energy conservation for both phases are considered. Hence, Schumann-Darcy-Brinkman-Forchheimer (SDBF) is a set of four equations [14]:

$$\varepsilon \frac{\partial \rho_{ms}}{\partial t} + div(\rho_{ms} u_m) = 0 \tag{3.5}$$

$$\varepsilon \frac{\partial \rho_{ms} u}{\partial t} + \nabla(\rho_{ms} u_m) = -\nabla p + \nabla \bar{\bar{\tau}} + \rho_{ms} \vec{g} \tag{3.6}$$

$$\begin{aligned} \varepsilon \frac{\partial \rho_{ms} c_{p,ms} T_{ms}}{\partial t} + \frac{\partial \rho_{ms} c_{p,ms} u_{ms}}{\partial z} &= \nabla\left(k_{eff} \nabla T_{ms}\right) - p \nabla \vec{u}_m \\ + tr[\nabla(\vec{u}_m)\bar{\bar{\tau}}] + \frac{\vec{u}_m \cdot \vec{u}_m}{2\varepsilon} \times \frac{\partial \rho_{ms}}{\partial t} &- h_v\left(T_{ms} - T_{pb}\right) \end{aligned} \tag{3.7}$$

$$(1-\varepsilon) \frac{\partial \rho_{pb} c_{p,pb} T_{pb}}{\partial t} = h_v\left(T_{ms} - T_{pb}\right) \tag{3.8}$$

Many terms of equation (3.7) have very little importance: the second, third and fourth terms at the right size of eq. (3.7)(3.11) account the heating of the molten salt due to compression work (volume expansion/shrinkage), viscous effects and kinetic energy changes. Those three terms are evaluated to be 10^4 smaller than the convection and conduction terms. For this reason, Xu et al. neglect those terms [12].

Thermal diffusion is accounted only in eq. (3.7). However, to account for packed bed heat diffusion the thermal conductivity of the fluid k_{ms} is replaced by an effective thermal conductivity k_e. This coefficient accounts for diffusion of both fluid and packed bed. Effective thermal conductivity coefficient k_e is evaluated as a combination of the thermal conductivity of the molten salt and of the packed bed, weighed on the porosity ε. Xu et al [12] summarize several correlations for the evaluation of the effective thermal conductivity coefficient.

SDBF set of equations is more complete than Schumann set. More in detail, it can forecast vortex in the porous media and it accounts for porous-medium resistance. However, they are more complex to discretize and implement.

3.1.3 Hypothesis and assumptions

Some assumptions are commonly made by authors when studying a thermocline TES application. These assumptions are summarized into the next seven points. Assumptions concern symmetry around the axis, flow mode and material properties.

1. The problem is axisymmetric. Thus, the problem is two-dimensional and properties change along the axis and the radius, but not angularly. Garimella et al. and Xu et al consider the problem as 2D [6][12]. Other authors consider that properties change only along the axis and not along the radius. So, they treat the problem as one-dimensional; for example Pacheco et al., Yang et al, Kolb et al. [1][11][2].
2. Diffusion along the porous media can be neglected. As particles are almost spherical, direct contact between filler grains is very poor and molten salt completely surround them. As a consequence, conduction in the packed bed is very little and it can be neglected ([1][10]). Although these observations, some authors include the thermal conduction in the energy equation of the packed bed (eq. (3.8)) ([12][11]). Other authors neglect also heat conduction of the molten salt ([47]). Indeed, Keays et al. found that the Peclet number is very high in the axial direction and diffusion could be reasonably neglected during injection and withdrawn of molten salt to/from the thermocline ([48]).
3. Molten salt flow direction is one-dimensional (Xu, Garimella, Pacheco). Practically, distributor zones are designed to ensure one-dimensional flow direction and to prevent unwanted mixing of molten salt. These distributors are regions between the packed bed region and the inlet/exit ports of the tank (Figure 3-1). Even though, some authors have modeled the flow as two-dimensional in the packed bed and also in the distributor ([14]).

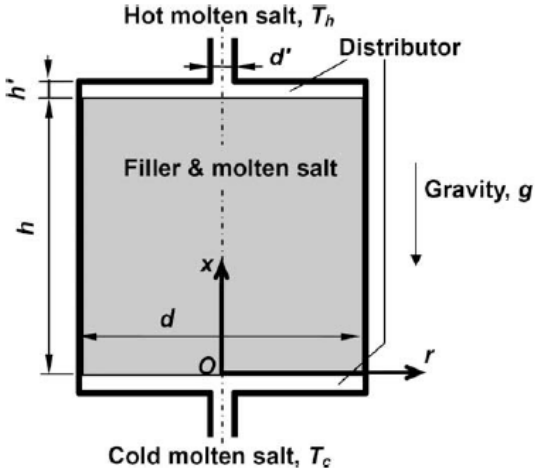

Figure 3-1: Schematic diagram of the thermocline TES [12]

4. Molten salt flow is assumed to be laminar in the packed bed region. Laminar flow is a consequence of the low molten salt velocity flowing in the packed bed [12].
5. The properties of the filler bed are constant. Also, the filler material is assumed to be homogeneous, isotropic and continuous [12].

6. Molten salt properties are assumed as constant by some authors, such as Yang et al[11]. Instead, others consider properties as temperature dependent, for example Garimella et al [14].
7. Temperature distribution in the particles of the packed bed is considered as uniform by all authors. This is true because the Biot number of the particles is little and the lumped capacitance method can be applied [49]. However, in some cases the Biot number is observed to be much greater than the threshold value of 0.1 [47]: in this case, Jefferson correction is applied. Jefferson correction consists in replacing the heat transfer coefficient with a modified heat transfer coefficient h':

$$h' = \frac{h}{1 + \frac{Bi}{5}} \tag{3.9}$$

This modified heat transfer coefficient allows using the lumped capacitance method with any Biot number, increasing accuracy of results.

3.2 Model implementation

After having discretized the governing equations of the thermocline TES systems, authors proceeded with the implementation of those equations. Numerical models developed by each author slightly differ between them because of different boundary conditions assumed, software chosen, discretization schemes applied and spatial discretization made. Equations are coded with several software. Each model will be briefly described.

3.2.1 Pacheco

Historically, the study of Pacheco and al. [1] is one of the first numerical models on molten salt thermocline available in literature. The heat transfer between a fluid and a packed bed porous material is described by the Schumann equations [10]. These equations are discretized with a finite difference method. Radial temperature distribution is taken as uniform, i.e. the model is assumed as one-dimensional. However, boundary conditions are implemented to account for heat losses to the environment. Thermal conduction is completely neglected for both the molten salt and the packed bed. The code was written in Visual Basic and executed as a macro in Microsoft Excel. The tank was divided in 80 equal volumes and time step was set at 4 seconds. Initial temperature for t=0 was imposed, and the inlet temperature in the tank was assumed as known at each time step. Pacheco and al. also tested a 5.9 meters tall and 3 meters diameter thermocline TES. The packed bed was of 3 cm diameter quartzite rocks and

silica sand with a porosity of 0.22 [1]. Data collected are the only data available in literature about temperature distribution in thermocline packed bed using molten salt as HTF. Most of authors use those data as point of reference.

3.2.2 Yang

Yang et al. [11] develop a thermocline numerical model which is based on Schumann equations, like Pacheco's one. Yang et al. also consider thermal diffusion along the packed bed. Hence, eq. ((3.3)) is modified into eq. ((3.10)).

$$(1-\varepsilon)\rho_{pb}c_{p,pb}\frac{\partial T_p}{\partial t} = (1-\varepsilon)k_{pb}\frac{\partial^2 T_{pb}}{\partial x^2} + h_v\left(T_{ms} - T_{pb}\right) \tag{3.10}$$

Although, Yang model is simpler than Pacheco's one because many strict assumption are made. For example, the tank is assumed adiabatic, so environmental thermal losses through cylinder walls are neglected. Furthermore, also Yang considers all the properties of both packed bed and molten salt as constant. Besides, as in Pacheco's case, radial temperature distribution is not accounted, i.e. the problem is one-dimensional.

Fundamental equations are discretized with a downwind-differencing scheme for time, centered-differencing scheme for conductivity and upwind-differencing scheme for advection [11].

To validate the model, Yang et al. built a little thermocline tank 0.55 meter tall and 0.263 meter diameter insulated with 0.1 m of fiberglass plus a thin aluminum sheet. Data collected during their experimentations are not available in literature [11].

3.2.3 Garimella

Equations drawn are the SDBF equations set (subsection 3.1.2). They include continuum, momentum and energy for both packed bed and molten salt. Equations are dimensionless and the spatial domain is discretized into centered finite volumes. Spatial domain is bi-dimensionally discretized and also distributor regions are included in the spatial discretization to examine molten salt mote in these zones. Second-order upwind scheme is used for convective fluxes, central-differencing for diffusive fluxes, second order implicit scheme for time and pressure-velocity coupling is implemented through PISO algorithm [50]. The computational are performed using the commercial software FLUENT. Compared to Pacheco's and Yang's model, Garimella's model is more performing and capable of more wide and precise simulations [14].

3.2.4 Xu

SDBF fundamental equations are chosen by Xu et al. [9]. However, some terms of those equations are neglected, as previously discussed. For example, heating of the molten salt due to compression work (volume expansion/shrinkage), viscous effects and kinetic energy changes is neglected. Governing equations are discretized using the finite volume method described by Patankar [51]. The spatial domain is discretized in a two-dimensional non-uniform mesh. Distributors are not included: uniform one-dimensional molten salt flow is considered at the entrance of the packed bed. Second-order differencing scheme is employed for convective fluxes, centered-differencing scheme for convective fluxes, implicit scheme for time and pressure-velocity coupling is solved with Patankar's algorithm SIMPLER. The numerical method has been implemented in a self-written simulation code [9].

3.3 Validation of the model – Pacheco's experimental data

Once the model is implemented it is fundamental to check its correctness comparing the results of the model with some experimental data. Pacheco et al. [1] carried out an experimental study of the thermocline. Pacheco and al. realized a small thermocline system to validate the technical feasibility of such storage. The tank was made of carbon steel, 5.9 m tall by 3.0 m diameter. It had an insulation of 23cm of fiber glass. The tank was designed by the American Petroleum Institute (API) for petrochemical issues. Solar salt were stocked at 390 °C, and withdrawn at 290 °C. The packed bed was made of quartzite rocks and silica sand, with a void fraction of 0.22. The nominal thermal capacity of the storage was 2.3 MWh_{th} [1]. Pacheco et al. collected data and they studied practical operational issues, such as compatibility of molten salt with mechanical components, and if the degree of thermal stratification was satisfying.

The test fared well, confirming the feasibility of a thermocline thermal storage using quartzite and silica sand as filler material (Figure 3-2). The thermocline is completely filled with molten salt at 390°C when molten salt at 290°C are injected at the bottom of the tank, starting the discharge process. Thermocline moves towards the top of the tank as molten salt at useful temperature are withdrawn. The experimental data fitted well the results evaluated with the numerical model previously developed by Pacheco et al., despite a certain deviation due to measurement incertitude [1].

Few other experimental tests on molten salt thermocline TES systems have been carried out since then. Yang built little experimental tanks of 0.55 meters tall and 0.263 meter diameter [11]. However, they did not publish data collected. Most of authors compare their model to Pacheco's experimental data; others use the data of the oil thermocline of Solar One. For example Kolb

validate its numerical model comparing its results with experimental data obtained during the test of the 180 MWh_{th} oil thermocline of Solar One [2].

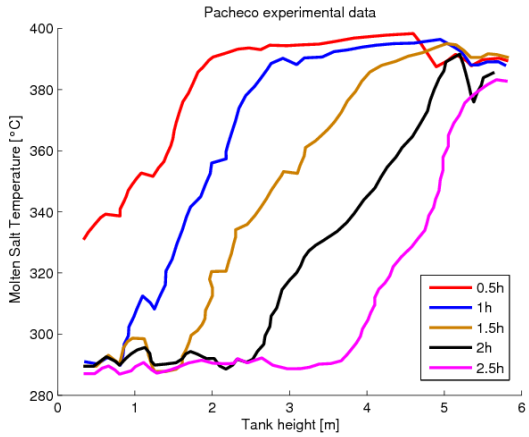

Figure 3-2: Pacheco experimental data. Temperature profile during discharge of a 2,3MWh_{th} thermocline tank filled with solar salt and quartzite rock/silica sand packed bed [1]

3.4 Previous findings on Thermocline Performances

Thermocline TES is designed to store and then supply molten salt at high temperature. High temperature molten salt is first injected in the storage during charge process. Afterwards, it is desired to withdrawn the maximum amount of molten salt still at this high temperature. To better understand the phenomenon, Figure 3-3 shows temperature distribution in a charged tank (on the left). Here, hot molten salt have been injected for 2 hours. Initially, the temperature in the tank was initially equal to 300 °C. From this charged tank, some thermal energy are withdrawn until the threshold temperature of 490°C is reached (on the right). Molten salt are withdrawn for 1.7h.

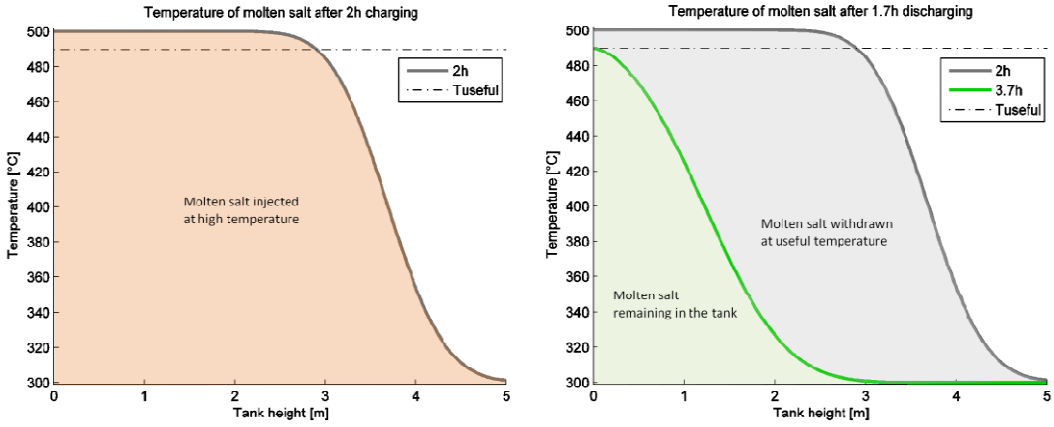

Figure 3-3: Thermocline TES charging (left) and discharging (right)

A certain quantity of heat is hence stored (highlighted in orange) and a certain amount is withdrawn (highlighted in light gray). It is observed that some molten salt are not withdrawn because at too low temperature (highlighted in light green). If the thermocline was steeper, more molten salt would have been withdrawn, and green area would be less extended. Hence, the steepness of the thermocline is fundamental and it deeply influences the performance of the entire TES.

Discharge efficiency is chosen as the thermocline performance indicator. Discharge efficiency is defined as the ratio of the useful energy withdrawn from the tank and the thermal energy initially stored (eq. (3.11)) [13]. Useful energy is the amount of heat discharged at a temperature greater to a threshold value. As high temperature is desired, this threshold value is arbitrarily assumed to be slightly lower than temperature of injected molten salt. For example, Garimella considers useful the molten salt above the threshold temperature defined in eq. (3.13) [13].

$$\eta_{disch} = \frac{Q_{with}@\ (T > T_{threshold})}{Q_{with,tot}} \tag{3.11}$$

$$Q_{with} = \dot{m}_{ms} c_{p,ms} (T_{hot} - T_{cold}) \tag{3.12}$$

$$T_{ms,threshold} = T_{ms,cold} + \left(T_{ms,hot} - T_{ms,cold}\right) \cdot 0.95 \tag{3.13}$$

In Figure 3-3, discharge efficiency is equal to the light gray surface (total energy that can be withdrawn) on the orange one (withdrawn useful energy). The threshold temperature chosen was 490°C (i.e., 5% temperature difference drop) and the corresponding discharge efficiency is about 65%.

As said, thermocline steepness directly influences the discharge efficiency. To achieve high performance, a steep and stable thermocline that guarantees good stratification is desired. Thus, thermocline behavior must be understood and parameters which could influence thermocline development have to be analyzed.

Thermocline development during charging and discharging is affected by a dozen parameters; during standby of the thermocline, i.e. when the molten salt is quiescent, it is influenced by only four parameters. The understanding of their effects on stratification phenomenon is fundamental to achieve high discharge efficiency. In the next subsection, these parameters will be singularly discussed and analyzed.

3.4.1 Inlet fluid velocity

According to Garmiella, Reynolds number affects thermocline development and an optimal Reynolds number is identified [14]. Garimella made several simulations changing molten salt velocity and keeping fixed the volume of the reservoir. It is found that Reynolds number affects thermocline expansion in three parallel ways. First, for low Reynolds number the thermocline expands due to thermal conduction. Indeed, the Péclet number is little and thermal conduction is significant. Heat flows from the hot region to the cold one, and thermocline region expands with time diffusively. Second, the heat exchange between molten salt and the packed bed is optimized at low Reynolds numbers. This is because molten salt remains long time in the thermal gradient zone and it manages to completely heat or cool itself up or down within the thermocline region. Contrarily, at high *Re* numbers, molten salt is faster and it needs a longer distance to be heated up. Consequently, the heat exchange zone, i.e. the thermocline, tends to extend. The third effect is heat loss to the environment. If Reynolds is little, more time is required discharge the tank and heat loss becomes more important. Summing up, an inlet velocity which maximizes the discharge efficiency can be found [14].

Garimella et al. observed this trade-off and they proposed an optimal range of Reynolds numbers for the inlet molten salt flow [14], [52]. Considering well-insulated tanks, optimal Reynolds numbers range between 50 and 100 [52] (Figure 3-4).

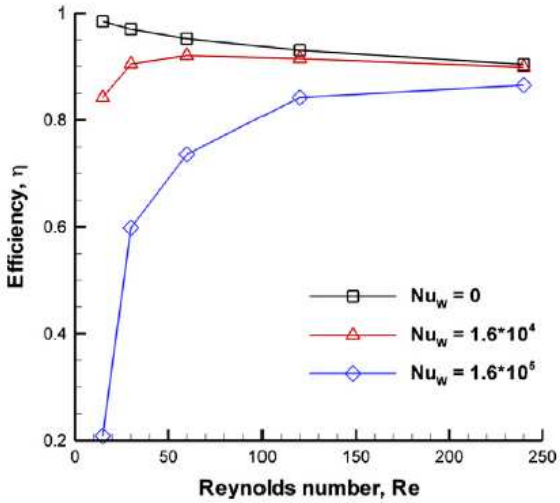

Figure 3-4: Discharge efficiency as a function of Reynolds under different heat loss rates (Nu) [14]

Also Xu et al. studied the effect of the inlet molten salt velocity on thermocline development [9]. Xu studied the change in discharge efficiency for an inlet Reynolds number range of 10-100 using a very well insulted tank. The tests were quite different from Garimella's. Indeed, Xu changed the diameter of the tank while keeping constant molten salt mass flow and the height of the tank.

So, he could control Reynolds number by changing the diameter. For large diameters Reynolds number was little and charging and discharging time was long. At low *Re*, expansion of the thermocline was slower but it lasted longer time. Xu found that thermocline was expanding quickly for high Reynolds numbers, but for just little time. This trade-off resulted in a very little influence of inlet molten salt velocity on discharge efficiency [12].

3.4.2 Porosity

Low porosity is desirable, but there is a critical value after which the discharge efficiency drops. Xu et al. [12] observed that an increase in porosity shrinks the thermocline. At high porosity, little heat has to be transferred from the molten salt to the packed bed. Thus, the fluid heats itself up (or cools down) easily within the thermocline, preventing the expansion of the thermocline itself. However, this is true only for very little porosity: thermocline steepness is almost unchanged for all porosities above ε=0.22.

Low porosity is also desired because it is economically convenient. Indeed, expensive molten salt are replaced by cheaper filler material. At the same time, too low porosity can spoil performances of the thermocline TES system. Concluding, a critical porosity around ε=0.22 is identified as the best compromise between effectiveness and costs of the storage [12].

3.4.3 Particle diameter

Little particle diameter are preferred because the contact area between molten salt and particle is increased. The dimensionless Biot number is littler and the packed bed is “readier” to absorb and release energy. Summing up, little particle enhance heat exchange with favorable impacts on discharge efficiency, which is increased [11][13][14].

3.4.4 Tank height

Once the volume of the storage is fixed, tall tanks are in general to be preferred. The thermal gradient occupies a certain height and displace itself upwards and downwards during charge and discharge processes. Obviously, if the height of the tank was doubled, the relative height occupied by the thermocline is halved. Hence, the thermocline appears as it was steeper, leading to higher discharge efficiency.

However, doubling the height reduces the diameter of the storage, as the storage volume is fixed. As a consequence, inlet area is littler and molten salt velocity results increased. However, this increase in velocity causes a slightly quicker extension of the thermocline. As a result, all authors agree that tall tank typically has greater discharge efficiency than a short one [14][1][9].

Unfortunately, maximum molten salt tank height is limited by structural and technical limits. Garimella assessed thermocline maximal height to 14 meters [13]; Pacheco limits the height to a similar value of 12 meters[1].

3.4.5 Inlet temperature

Inlet molten salt temperature has no influence on thermocline development and discharge efficiency. Xu et al. [9] simulated the discharge of a full charged thermocline TES system with several inlet temperatures. They compared dimensionless temperature profiles of each simulation finding that they were perfectly overlapping. Hence, discharge efficiency is independent on the inlet molten salt temperature [12].

3.4.6 Thermal conductivity

Low thermal conductivity is sought. Low thermal conductivity reduce heat diffusion from the hot region to the cold one, phenomenon which spoils thermal stratification. In these conditions, the thermocline extends quicker and outlet temperature drops early during a discharge, causing low discharge efficiency.

Xu et al. concluded that effective thermal conductivity below a certain threshold value has little influence on thermocline development [12]. Several fictive heat conductive coefficients were tried and temperature profiles compared. As advective heat transfer remains predominant, thermal conductivity has marginal effect until the critical value of 25 W/mK is reached. This value is very high: quartzite rock and silica sand and molten salt are characterized by typical thermal conductivity of, respectively, 5.3 W/mK and 0.5 W/mK. As a result, a change of typical heat conductive coefficients of molten salt and of packed bed little affect both thermocline expansion and discharge efficiency, if the value is below 25 W/mK [12][11].

Xu et al. also compared five relationships available in literature for the calculation of the effective thermal conductivity. Typical thermal conductivity coefficients evaluated with those correlations were different up to an order of magnitude. However, those thermal conductivity coefficients were always largely below the threshold value of 25 W/mK. Hence, any of those five correlations can be arbitrarily used to evaluate the effective thermal conductivity coefficient [12].

3.4.7 Interstitial heat transfer coefficient

Typical interstitial heat transfer coefficients are large enough to achieve quick heat exchange between molten salt and the packed bed [12]. The temperature difference between the molten salt and the packed bed is usually in the range 0.1 °C – 2.5 °C. These temperature differences are small and they have no effect on thermocline development. Xu et al. tested several fictive heat

interstitial coefficient and they found that thermocline is remarkably affected only by heat transfer coefficient which are 100 times lower than the typical values. With such poor interstitial heat transfer coefficient the temperature difference between the molten salt and the packed bed rises to 10 °C; as a result, the thermocline expansion is enhanced and the discharge efficiency decrease deeply [12].

Several correlations are available in literature for the evaluation of the interstitial heat transfer coefficient. Those relations predict almost the same coefficients. As the sensitivity of the thermocline on this coefficient is little, all correlations are considered as enough accurate [12].

3.4.8 Insulation of the tank

A good insulation of the tank limits heat loss and guarantees uniform cross sectional temperature distribution. On the other hand, poor insulation leads to important radial temperature gradients along the radius. Disuniformity of temperature can cause recirculation fluxes and local vortex which provokes unwanted molten salt mixing. The stratification is slightly ruined, and discharge efficiency decreases. Also, molten salt might freeze within few days in tanks with very thin insulating layers [9][52].

3.4.9 External air velocity

External air velocity has little impact on heat losses to the environment when the tank is well insulated. External air velocity does not affect much heat losses because most of thermal resistance is the wall conductive resistance. An increase of the velocity and, thus, a decrease of the convective resistance, is not much relevant on the total thermal resistance. Hence, the drop in molten salt temperature at the internal side of the tank wall is slow. At the same time, heat has enough time to diffuse from the center of the tank to the wall boundaries, compensating the temperature drop at the wall. Hence, radial temperature distribution remains always almost constant. Summing up, heat loss rate of well insulated tank is little dependent on external air velocity; also, radial temperature distribution is always constant [9].

On the other hand, if the tank is poorly insulated temperature distribution is not anymore uniform by the radius and heat loss rate depends strongly on external air velocity. The temperature at the wall drops readily in poor insulated tank and diffusion is slow due to low thermal conductivity: heat has not enough time to diffuse from the center to the wall regions. As a result, molten salt might freeze at the wall while the temperature at the center is almost unchanged [9].

Summing up, high tank insulation is needed to limit thermal losses at any external wind velocity. Also, high tank insulation prevents molten salt to suddenly freeze and ensure almost constant radial temperature distribution [9].

4 Development of the thermocline model

In this chapter a new numerical model which describes the thermocline TES system is developed. In the previous chapter, previous researches and studies on thermocline TES systems have been analyzed. It was found that Schumann equations have been widely employed for this purpose. These equations will be discretized with a finite difference method. Afterwards, the model will be implemented on Matlab and it will be finally validated with four analytical solutions and with experimental data.

4.1 Fundamental equations

The chosen set of equations is the Schumann equations set. It an accurate set of equations for the description of heat transfer between a fluid and a packed bed. Hypothesis made are:

1. The physical properties of the packed bed are assumed to be constant, while those of the fluid are temperature dependent.
2. Viscous effects and vortex are considered as secondary and negligible
3. Molten salt flow through the packed bed is one-dimensional and aligned with the tank axis.
4. Molten salt flow is laminar.
5. The filler is assumed to be isotropic, homogenous and continuous.
6. The problem is considered to be 2D, axisymmetric.
7. Thermal diffusion is accounted only in the molten salt energy equation. To do that, an equivalent thermal conductivity coefficient is considered. This coefficient is a combination of the thermal conductivity coefficient of the molten salt and of the packed bed.

Fundamental equations which describe the problem are mass conservation, molten salt energy yield and packed bed energy yield eq. (4.1)-(4.3). Molten salt velocity is defined as in eq. (4.4).

$$\begin{cases} \varepsilon \dfrac{\partial \rho_{ms}}{\partial t} + div(\rho_{ms} u_m) = 0 & (4.1) \\ \varepsilon \rho_{ms} c_{p,ms} \dfrac{\partial T_{ms}}{\partial t} + \rho_{ms} c_{p,ms} u_m \dfrac{\partial \mathrm{T_{ms}}}{\partial z} = \dfrac{\partial}{\partial z}\left(k_{eff} \dfrac{\partial T_{ms}}{\partial z}\right) + \dfrac{1}{r}\dfrac{\partial}{\partial r}\left(k_{eff} r \dfrac{\partial T_{ms}}{\partial r}\right) + h_v\left(T_{pb} - T_{ms}\right) & (4.2) \\ (1-\varepsilon)\rho_{pb} c_{p,pb} \dfrac{\partial T_{pb}}{\partial t} = h_v\left(T_{ms} - T_{pb}\right) & (4.3) \end{cases}$$

$$u_m = \varepsilon \cdot u \quad (4.4)$$

Where T_{ms} is the temperature of the molten salt and T_{pb} is the temperature of the packed bed. Thermal conductivity k_{eff} is the effective thermal conductivity of the molten salt and the packed bed (eq. (4.5), exponential averaged, [12]).

$$k_{eff} = k_{ms}^{\varepsilon} + k_{pb}^{1-\varepsilon} \tag{4.5}$$

h_v is the volumetric heat transfer coefficient (see subsection 3.1.1). Xu et al [12] compare several relationships for the evaluation of h_v. According to their research, the following formula is chosen (eq. (4.6)) [53][12]. According to Xu, equation is valid for Reynolds and Prandtl numbers typical of thermocline thermal energy storages. For the detail on these correlations it is suggested to consult books such as "Heat transfer in packed beds" [54] or the paper of Xu[12].

$$h_v = 6 \cdot h \cdot \frac{1-\varepsilon}{D_c} \tag{4.6}$$

$$h = \left(2 + 1{,}1 * Pr_{ms}^{\frac{1}{3}} \cdot Re_d^{0.6}\right) \cdot \frac{k_{ms}}{D_s} \tag{4.7}$$

where k_{ms} is the molten salt thermal conductivity.

4.2 Discretization

Authors develop their model choosing finite difference approximations. Usually, they replace differential terms applying a centered-scheme for diffusion, upwind schemes for advection and implicit schemes for time.

Finite difference method consists in replacing the derivates of a differential equation by finite difference approximations according to a discretization scheme [55]. The spatial domain is divided into several discrete nodes: each node is surrounded by other nodes and properties of each node are taken as constant. For example, temperature, pressure, density, etc. Mass, momentum and energy yield are accounted at the interfaces between nodes. So, properties at a certain node are evaluated according to the properties of its surrounding nodes and according to the mass/energy yield through the control volume [55][51].

The control volume of the thermocline tank is divided into *Nx* nodes along the axial direction and *Nr* nodes along the radial direction (Figure 4-1). To increase accuracy of results, the mesh is finer next to the wall surface, where molten salt temperature is affected by heat loss to the environment. Conventionally, the node 1 is on the top of the tank while the node *Nz* is at the bottom, while the node 1 is at the center of the tank and the node *Nr* is at the boundary of the tank. Mass and energy yields have to be satisfied around each

volume. It is chosen to represent temperature in the center of the nodes and velocity at the boundaries of the control volumes.

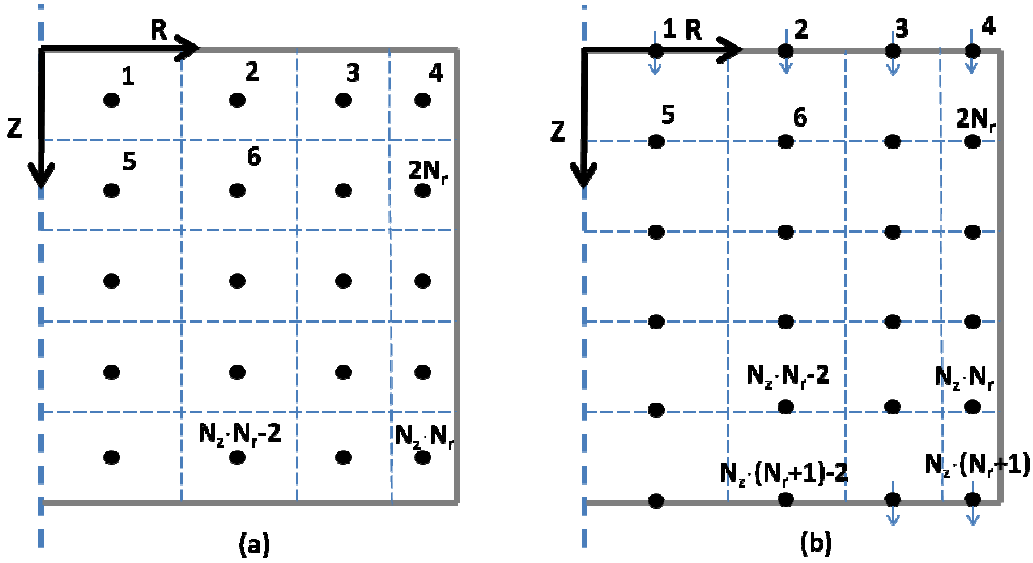

Figure 4-1: Discretization of spatial domain. Temeprature is stored at the center of the nodes (left); velocity at the interface of control volumes (right). Node 1,1 is at the top of the tank, at the centerline. Node Nz,Nr is at the bottom of the tank, in contact with wall surface

Discretization consists in two steps. First, equations are integrated in each volume in order to simplify second-order spatial differential terms. Afterwards, discretization schemes are applied to replace differential terms with approximate difference terms.

Several discretization schemes exist. Diffusion at the interface is usually approximate with a centered-difference scheme [51]. For example, northern diffusion is approximated after integration as follows:

$$\left(k\frac{\partial T}{\partial z}\right)_n \cong \frac{k_n(T_{i-Nr}-T_i)}{\Delta z} \qquad i=1,2,\dots,N_r\cdot N_z \qquad (4.8)$$

Here convention N, S, O, W is used to represent northern node (*i-Nr*), southern node (*i+Nr*), western node (*i+1*) and eastern node (*i-1*); P indicates the studied node (*i*). Concerning advection, the most natural approximation is the centered-difference scheme. Assuming that interface lies midway between nodes, centered-differencing approximation for northern advection gives:

$$\left(\rho c_p u * T\right)_n \cong \left(\rho c_p u\right)_n \cdot \frac{T_{i-Nr}+T_i}{2} \qquad (4.9)$$

Unfortunately, this scheme suffers instability when applied to advection. A stable alternative is the upwind-differencing scheme. This scheme considers that the fluid flows from a node to the adjacent one. So, in the upwind scheme, temperature at the interface is equal to the temperature of the upwind node. For instance, northern advection becomes [51]:

$$\left(\rho c_p u * T\right)_n \cong \left(\rho c_p u\right)_n \cdot T_{i-Nr} \tag{4.10}$$

This scheme is unconditionally stable and authors use it to develop their thermocline models. Other schemes are also available in literature, such as power-law scheme, exponential scheme and the hybrid scheme [51].

Finally, time derivates can be approximated with an explicit (eq. (4.11)) or implicit scheme (eq. (4.12)). In the explicit-differencing scheme temperature at the following time step is evaluated from known temperatures at the present time step. So, T_{ms}^{t+1} and T_{pb}^{t+1} are calculated straight-forwardly. In the implicit-differencing scheme, temperatures at the following time step are calculated together with temperatures at the following time step [51]:

$$\rho c_p \frac{\partial T}{\partial t} \cong \frac{\left(\rho c_p T\right)^{t+1} - \left(\rho c_p T\right)^{t}}{\Delta t} \tag{4.11}$$

$$\rho c_p \frac{\partial T}{\partial t} \cong \frac{\left(\rho c_p T\right)^{t} - \left(\rho c_p T\right)^{t-1}}{\Delta t} \tag{4.12}$$

Implicit scheme is computationally more complex, but it is to be preferred because it is unconditionally stable, while the explicit is not [51].

Summing up, centered-differencing scheme is used for diffusion, upwind-differencing scheme is chosen for advection and implicit downwind-differencing scheme is used for time.

4.2.1 Discretization of mass balance equation

The mass conservation equation has to be included in the set of equation when variable physical properties are considered. If density is temperature dependent, there might be a density gradient in the volume: mass conservation determines the velocity of the molten salt depending on this density gradient. In the mesh, velocity points are taken as in Figure 4-1.

$$\varepsilon \frac{\partial \rho_{ms}}{\partial t} + div(\rho_{ms} u_m) = 0 \tag{4.13}$$

$$u_m = \varepsilon \cdot u \tag{4.14}$$

No second order differential terms are present, so discretization can take place directly without any integration. An implicit downwind scheme is considered for the change in density with time; an upwind scheme is applied for the advective term in the equation. According to the convention assumed:

$$\frac{\rho_{ms,i}^{t} - \rho_{ms,i}^{t-1}}{\Delta t} + \frac{\left(\rho_{ms} u_m\right)_S^t}{\Delta z} - \frac{\left(\rho_{ms} u_m\right)_N^t}{\Delta z} = 0 \tag{4.15}$$

$$\frac{\rho_{ms,i}^{t} - \rho_{ms,i}^{t-1}}{\Delta t} + \frac{\rho_{ms,s}^{t} u_{m,s}^{t}}{\Delta z} - \frac{\rho_{ms,n}^{t} u_{m,n}^{t}}{\Delta z} = 0 \tag{4.16}$$

Equation (4.16) is rearranged. Also, subscript P, N and S are replaced by *i*, *i-Nr* and *i+Nr*. Inlet velocity is know, as the mass flow at the entrance is imposed. So, the unknown is velocity at the southern side of the tank ($u_{m,i}$):

$$\frac{\rho_{ms,i}^{t} - \rho_{ms,i}^{t-1}}{\Delta t} + \left(\frac{\rho_{ms,i-Nr} u_{m,i}}{\Delta z}\right)^t - \left(\frac{\rho_{ms,i} u_{m,i+Nr}}{\Delta z}\right)^t = 0 \tag{4.17}$$

$$\left(u_{m,i+Nr} - \frac{\rho_{ms,i-Nr}}{\rho_{ms,i}} \cdot u_{m,i}\right)^t = \frac{\Delta x(\rho_{ms}^{t} - \rho_{ms}^{t-1})}{\Delta t \rho_{ms,i}^{t}} \tag{4.18}$$

Defining the following coefficients, equation (4.18) is rearranged:

$$a_i = -\frac{\rho_{ms,i-Nr}^{t}}{\rho_{ms,i}^{t}} \tag{4.19}$$

$$a_{i+Nr} = 1 \tag{4.20}$$

$$c_i = \frac{\Delta x(\rho_{ms}^{t} - \rho_{ms}^{t-1})}{\Delta t \rho_{ms,i}^{t}} \tag{4.21}$$

$$a_{i+Nr} u_{m,i+Nr}^{t} - a_i u_{m,i}^{t} = c_i \tag{4.22}$$

Eq. (4.22) recalls a matrix product. Indeed, coefficients *a* can be collected in matrix A, and the coefficients *c* in vector C. So, the molten salt velocity can be obtained solving the linear system:

$$\boldsymbol{A} * \boldsymbol{u_m} = \boldsymbol{C} \tag{4.23}$$

In this case, molten salt was considered to flow from north to south. Obviously, if the molten salt was flowing from south to north the discretization of the mass conservation equations must be revised opportunely.

4.2.2 Discretization of energy equations

In this case, second order differential terms constrain to integrate along the z-axis and r-axis before applying discretization schemes (2D problem). The integration and discretization passages are long and complex. They are explained in detail in Appendix-A. After the double integration, time is discretized with an implicit downwind-differencing scheme, thermal diffusion with a centered-differencing scheme and advection with an upwind-differencing scheme. This equation is rearranged and several groups are identified. As a result, a linear system is found (4.25). For molten salt, temperature at the node *i* depends on the temperatures of the neighbor nodes, on the temperature of the packed bed and on the molten salt temperature at the previous time step:

$$a_{i,i}\, T^t_{ms,i} + a_{i,i-1}\, T^t_{ms,i-1} + a_{i,i+1}\, T^t_{ms,i+1} + a_{i,i+Nr} T^t_{ms,i+Nr} + a_{i,i-Nr} T^t_{ms,i-Nr} = c_i \tag{4.24}$$

The definition of those groups and the passages that led to those equations are presented in Appendix-A. Eq. (4.24) recalls a matrix product. Indeed, coefficients *a* can be collected in matrix **A**, and the coefficients *c* in vector **C**. Thus, molten salt temperature can be simply obtained:

$$\boldsymbol{A} * \boldsymbol{T} = \boldsymbol{C} \tag{4.25}$$

The boundaries conditions imposed are:

- $\left.\frac{\partial T}{\partial r}\right|_{r=0} = 0$ at the center of the tank, because of symmetric considerations,
- convection with the environment through the wall at the tank wall,
- imposed velocity at the entrance of the tank,
- adiabatic conditions at the top and the bottom of the tank.

Unfortunately, the particle temperature $T^t_{pb,i}$, which shows out in the coefficient c_i (eq. (4.24)), is not know a priori and the problem cannot be solved straight forwardly. Besides, temperature dependant coefficients (ρ, c_p, k) should be

calculated on temperature T_{ms}, which is the unknown. Thus, an iterative procedure is needed to overcome this problem.

Iterations are composed of four steps. First, packed bed temperature is guessed in each node. For example, it can be assumed equal to the particle temperature at the previous time step. Also, physical properties are evaluated on the fluid temperature at the previous time step. Second, molten salt temperature is calculated with equation (4.25). Third, the packed bed temperature is calculated. To do that, eq. (4.3) is discretized with an implicit scheme for time:

$$\frac{(1-\varepsilon)\rho_{pb}c_{p,pb}}{\Delta t}\cdot(T_{pb,i}^{t}-T_{pb,i}^{t-1})=h_v(T_{ms,i}^{t}-T_{pb,i}^{t}) \tag{4.26}$$

$$T_{pb,i}^{t}=\frac{h_v T_{ms,i}^{t}+\frac{(1-\varepsilon)\rho_{pb}c_{p,pb}}{\Delta t}\cdot T_{pb,i}^{t-1}}{h_v+\frac{(1-\varepsilon)\rho_{pb}c_{p,pb}}{\Delta t}} \tag{4.27}$$

Finally, packed bed temperature T_{pb} is updated and another iteration take place. At each iteration residuals φ are evaluated. Residuals are defined as the relative variation of a certain quantity between two iterations. For example, considering molten salt temperature, at the iteration *n* the residuals at the node *i* is:

$$\varphi_{T_i}=\frac{T_{i,n}^{t}-T_{i,n-1}^{t}}{T_{i,n}^{t}} \tag{4.28}$$

Residuals are evaluated for molten salt velocity, molten salt temperature and packed bed temperature at each node. When the maximum residual among those drops below the value of 10^{-5}, convergence is attained and the iterative process stops.

4.2.3 Flow chart of the thermocline model

The model is schematized as in Figure 4-2. First, tank properties, molten salt properties and packed bed properties are set. Also, mesh dimension and time step length are to be chosen as well as many other parameters. Main parameters that can be are:

- Vessel characteristics:
  - height [m],
  - storage capacity [h of full-load capacity],

  - wall structure (number of layers, thickness and thermal conductivity of each layer, emissivity of external surface),
  - porosity [-],
  - packed bed particle average diameter [m].
- External conditions;
  - wind velocity [m/s],
  - environmental temperature [°C].
- Molten salt and packed bed properties:
  - functions which describe the change in viscosity, density, thermal conductivity and heat capacity of molten salt with temperature,
  - packed bed constant properties (density and heat capacity).
- Discretization parameters:
  - number of axial nodes [Nz],
  - number of radial nodes [Nr],
  - spatial distribution of radial nodes (non-uniform mesh along the radius),
  - time step length [s].
- Simulation conditions:
  - molten salt mass flow rate at all time steps [m/s],
  - temperature of injected molten salt at any time step [°C],
  - initial temperature of the molten salt and packed bed in the tank [°C],
  - length of the simulation [s].

Molten salt mass flow rate, temperature of molten salt at any time step and initial temperature are set as constant or read from a .xlsx file.

Simulation starts at $t_1 = 0$. Temperature of molten salt, velocity of molten salt and temperature of packed bed is iteratively evaluated in all nodes until residuals reach the imposed value (default value is 10^{-5}). Once residuals are attained, time is increased $t_i = t_{i-1} + dt$ and iterations restarts.

Once $t_i = t_{end}$ the simulation ends and results are displayed and printed in .xlsx file (Results.xlsx).

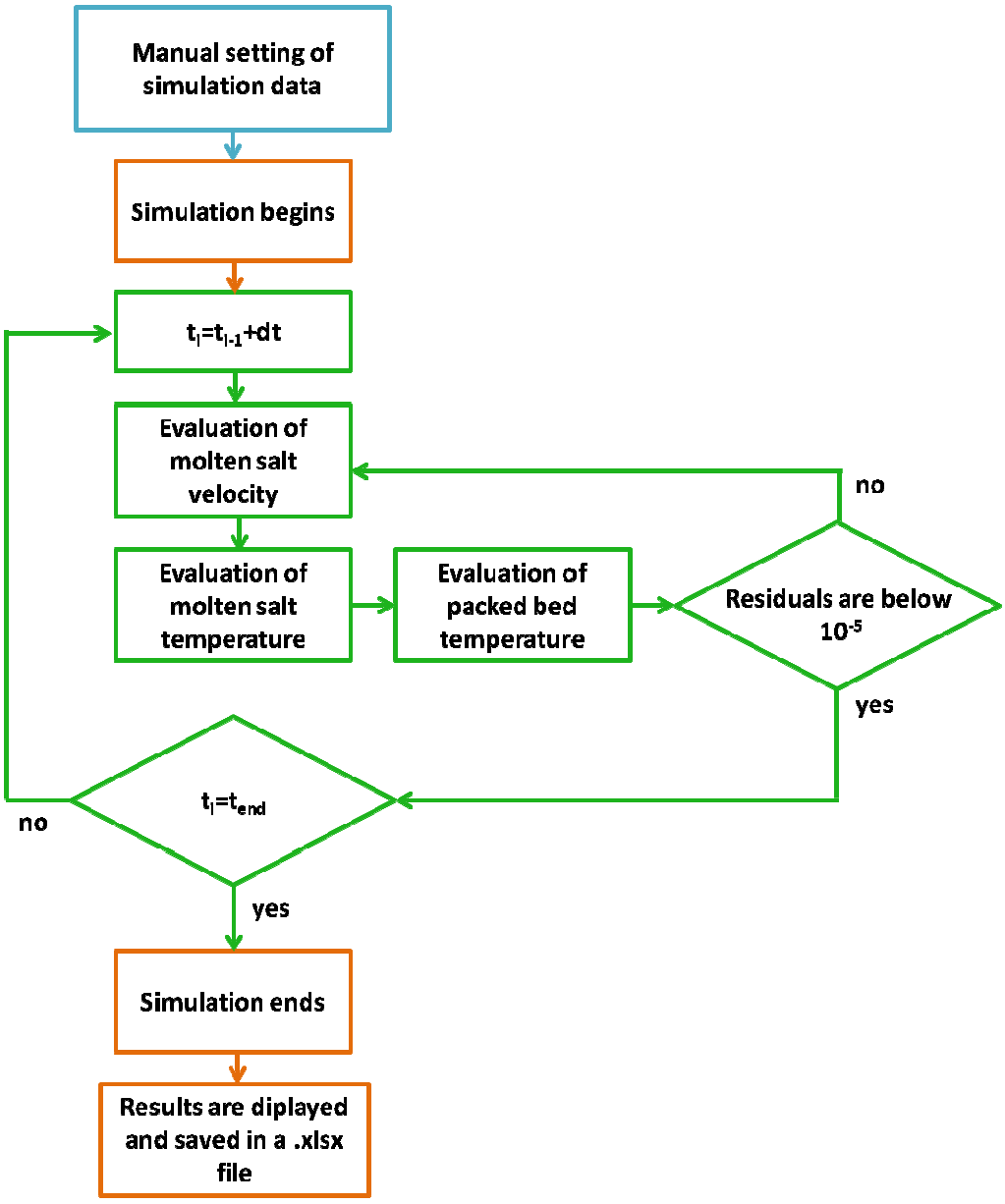

Figure 4-2: Flow chart of the thermocline model

4.3 Comparison with analytical solutions

The numerical model is implemented in Matlab and is compared with some analytical solutions. Fundamental equations are a system of differential partial equations and there is no analytical solution to the entire problem. However, it is possible to find some particular analytical solutions. For example,

it is possible to study molten salt transient radial diffusion only; in this case, axial diffusion and advection are neglected and the packed bed is removed. This problem has an analytical solution and the developed model must agree with it. In the next sections, the model is compared with four analytical solutions:

- transient radial diffusion,
- transient axial diffusion,
- heat transfer between molten salt and packed bed,
- axial advective-diffusive transport.

4.3.1 Transient radial diffusion

Only radial transient diffusion of the molten salt is considered. Axial diffusion, axial advection and heat transfer with the packed bed are neglected. This problem is described by partial differential equation eq. (4.29). Boundary conditions are convection with the environment and axisymmetric condition at the center of the tank ($r = 0$):

$$\begin{cases} \rho c_p \dfrac{\partial T_{ms}}{\partial t} = \dfrac{1}{r}\dfrac{\partial}{\partial r}\left(k\, r \dfrac{\partial T_{ms}}{\partial r}\right) \\ T(r, t = 0) = T_0 \\ -k \left.\dfrac{\partial T_{ms}}{\partial r}\right|_{r=0,t} = 0 \\ -k \left.\dfrac{\partial T_{ms}}{\partial r}\right|_{r=R,t} = h(T_{ms} - T_{amb}) \end{cases} \tag{4.29}$$

T_{amb} is the external temperature of the environment. The mathematical passages to draw the solution of the partial differential equation are here briefly presented as they are long and complex. It is recommended to consult a book on heat conduction for further details [56]. In brief, the resolution strategy redefining and regrouping the variables:

$$r' = r/R \qquad \vartheta = \frac{T - T_{amb}}{T_0 - T_{amb}} \qquad \alpha = \frac{k}{\rho c_p} \qquad H = \frac{h}{k} \tag{4.30}$$

Mathematical passages are exhaustively presented in Appendix-B. Finally, the solution of the radial transient diffusive problem is:

$$\vartheta(r', t) = \sum_{m=1}^{\infty} \frac{2}{R} \frac{H}{H^2 + \beta_m^2} \exp(-\alpha \beta_m^2\, t) \cdot \frac{J_0(\beta_m\, r')}{J_0(\beta_m\, R)} \tag{4.31}$$

This analytical solution is compared with the developed numerical model. Physical properties are assumed as constant. The analytical solution and

the numerical one are almost perfectly overlapped (Figure 4-3). The maximal temperature difference between the numerical and analytical solutions is below 2.5°C (Figure 4-4): the numerical solution is considered as correct and enough accurate.

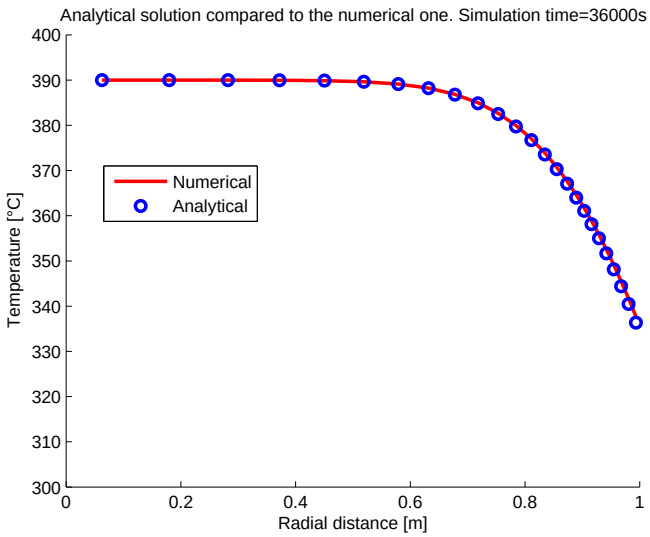

Figure 4-3: Radial diffusion. Analytical solution compared to the numerical one

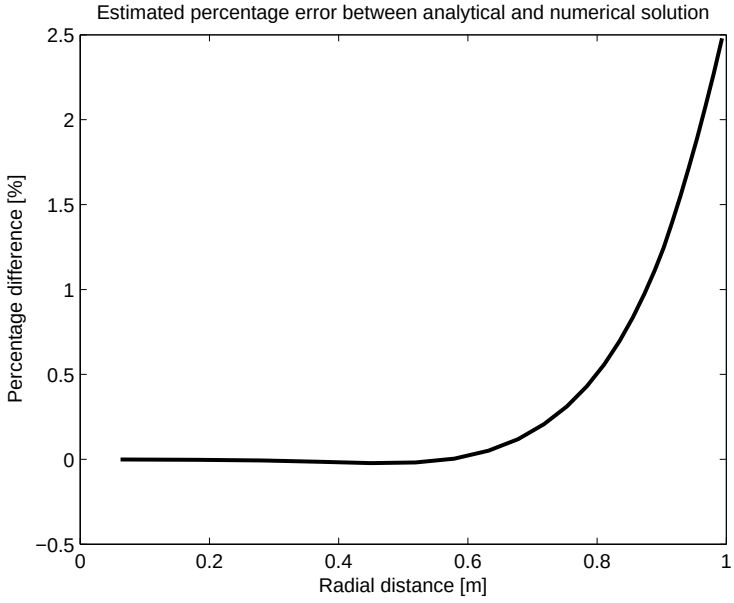

Figure 4-4: Radial diffusion. Estimated error

4.3.2 Transient axial thermal diffusion

Now, only axial transient diffusion of the molten salt is considered. This means that radial diffusion, axial advection and heat transfer with the packed bed are neglected. Low initial temperature T_1 is assumed in the lower half of the cylinder and high initial temperature T_2 is set in the upper half.

The problem recalls heat transfer in semi-infinite medium. The problem can be modeled as two semi-infinite regions of temperature T_1 and T_2 put in contact. As the two semi-infinite regions are of same medium, the contact temperature at the interface is the average temperature $T_1/2+T_2/2$ [49]. Just one of the two semi-infinite regions is studied: temperature in the other half region is symmetrical. The problem is described by this partial differential equation with these boundary conditions:

$$\begin{cases} \rho c_p \dfrac{\partial T_{ms}}{\partial t} = \dfrac{\partial}{\partial z}\left(k \dfrac{\partial T_{ms}}{\partial z}\right) \\ T(z > 0, t = 0) = T_1 \\ T(z = 0, t) = \dfrac{T_1 + T_2}{2} = T_m \\ T(z \to \infty, t) = T_0 \end{cases} \tag{4.32}$$

The mathematical passages to obtain the solution of this partial differential equation are not presented as they can be found in literature [49]. In brief, this problem can be solved defining a variable of similitude η eq. (4.33) and temperature distribution is found to be a function of the Gauss error function (eq.(4.35)):

$$\eta = \frac{z}{\sqrt{4\alpha t}} \tag{4.33}$$

$$\vartheta_{ms} = \frac{T - T_0}{T_m - T_0} \tag{4.34}$$

$$\vartheta_{ms} = erfc(\eta) \tag{4.35}$$

However, the hypothesis of semi-infinite region is constraining and more accurate solution is developed. Indeed, the assumption of semi-infinite region is valid until a certain time, i.e. until $\eta<3$ [49]. In our case, the assumption is vanished when the thermocline reaches the bottom (or the top) of the tank. So, a more complete analytical solution is drawn using the method of separation of variables. The problem is the same as for the semi-infinite medium except for the last boundary condition which is replaced by adiabatic boundary conditions (eq.(4.36)), as heat loss with the environment are neglected for this analytical solution.

$$\begin{cases} \rho c_p \dfrac{\partial T_{ms}}{\partial t} = \dfrac{\partial}{\partial z}\left(k \dfrac{\partial T_{ms}}{\partial z}\right) \\ T(z, t=0) = T_1 \\ T(z = H/2, t) = \dfrac{T_1 + T_2}{2} = T_m \\ \left.\dfrac{\partial T_{ms}}{\partial x}\right|_{z=0} = 0 \end{cases} \tag{4.36}$$

The solution of this problem is [49][56]:

$$\vartheta(X, \tau) = \sum_{n=1}^{\infty} \frac{4}{(2n+1)\pi} * \exp\left(-(2n+1)\frac{\pi}{2}\tau\right) \cdot \sin\left((2n+1)\frac{\pi}{2}X\right) \tag{4.37}$$

$$\tau = \frac{\alpha t}{H^2} \qquad x = \frac{X}{H} \qquad \vartheta = \frac{T - T_m}{T_0 - T_m} \tag{4.38}$$

This analytical solution is compared with the developed numerical model. Physical properties are assumed as constant. As in Figure 4-5, the analytical solution and the numerical one are perfectly overlapped. Precision is great, and it gets better with time, even when the thermocline occupies all the tank height. The temperature difference between the analytical and numerical solution is always below 0.1%, which is very accurate (Figure 4-6).

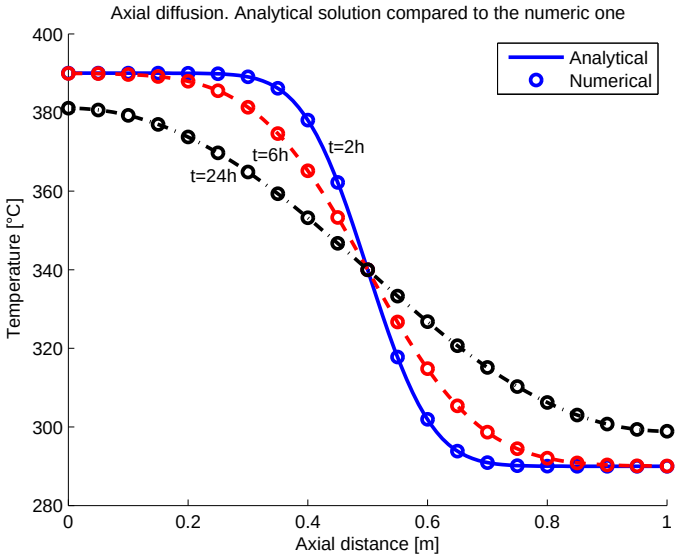

Figure 4-5: Axial diffusion. Numerical results compared to the analytical ones

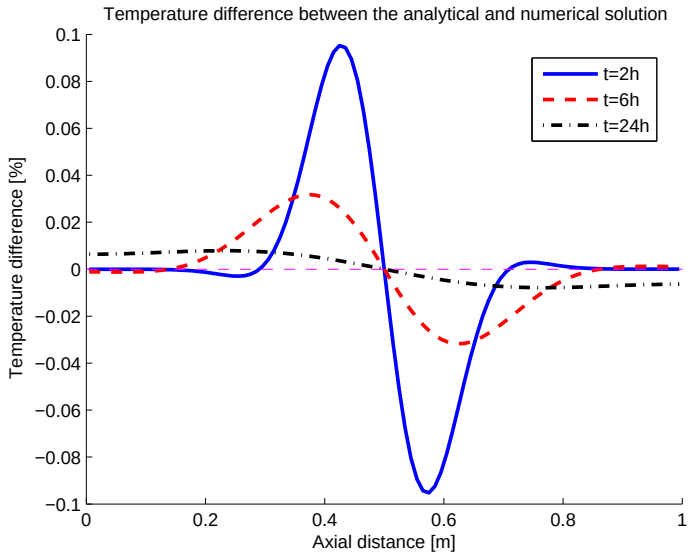

Figure 4-6: Axial diffusion, estimated error

4.3.3 Heat transfer between molten salt and packed bed

Heat transfer between molten salt and packed bed can be studied analytically if advection and diffusion are neglected. The equations to be solved are two, one for molten salt temperature and one for packed bed temperature (eq. (4.39)-(4.40)). There are no boundaries conditions, except for initial temperature at $t = 0$.

$$\begin{cases} \varepsilon \rho_{ms} c_{p,ms} \dfrac{\partial T_{ms}}{\partial t} = h_v \left(T_{par} - T_{ms}\right) & (4.39) \\ (1-\varepsilon) \rho_{par} c_{p,par} \dfrac{\partial T_{pb}}{\partial t} = h_v \left(T_{ms} - T_{par}\right) & (4.40) \\ T_{ms}(z, t=0) = T_{ms,0} \\ T_{pb}(z, t=0) = T_{pb,0} \end{cases}$$

The Biot number of this problem is little but sometimes above 0.1. Jefferson correction is applied and the problem is treated with the lumped capacitance method [57]. The problem recalls the scholastic problem of certain number of spheres (i.e. particles of the packed bed) immersed in a fluid (i.e., the molten salt) at a different temperature. In this case, the problem is more complex because both solid and fluid temperatures vary with time.

The mathematical passages to draw the solution of this ordinary differential equation system are exhaustively presented in Appendix-C. After several mathematical passages, dimensionless packed bed temperature is found:

$$\vartheta_{pb}(t) = \vartheta_{pb,0} \cdot \exp\left(-\frac{h_v \lambda}{C_{pb}} t\right) \tag{4.41}$$

Knowing the temperature of the packed bad, the temperature of the molten salt is readily drawn:

$$T_{ms}(t) = \frac{C_{pb}}{C_{ms}}\left(T_{pb,0} - T_{pb}(t)\right) + T_{ms,0} \tag{4.42}$$

The analytical solution is compared to the numerical one. Maximal Biot number is found to be 0.33: hence, Jefferson correction is still valid. Both temperature of the molten salt and packed bed found with the numerical model well fits temperature predicted by the analytical solution (Figure 4-7). Error between the analytical and the numerical solution is always below 1.0 °C, which is a satisfying value (Figure 4-8).

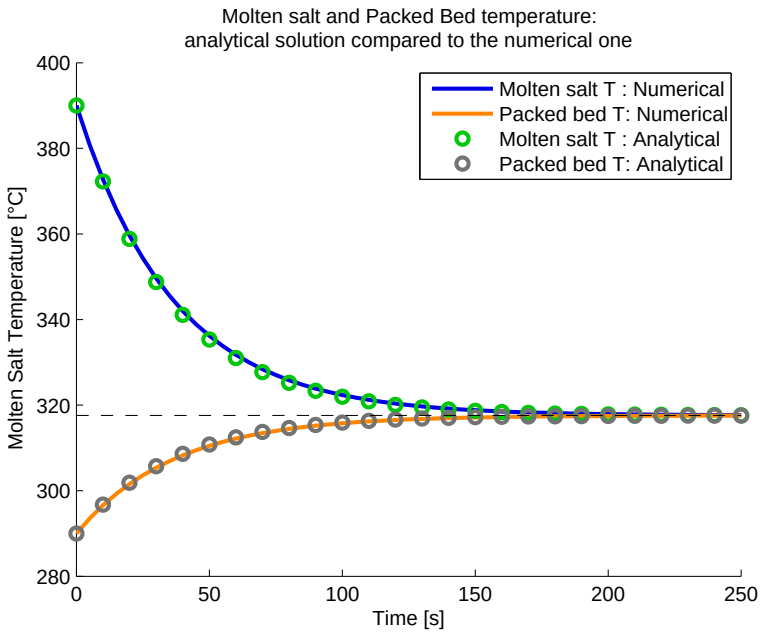

Figure 4-7: Molten salt - packed bed heat transfer. Analytical solution compared to the numerical one

Velocity of the molten salt in thermocline TES system is enough slow to ensure complete heat transfer between molten salt ad packed bed. Indeed, in typical TES molten salt velocity is about 0.5 mm/s [12]: it is expected that in nominal working conditions the temperature of the packed bed will always be very close to the temperature of the molten salt.

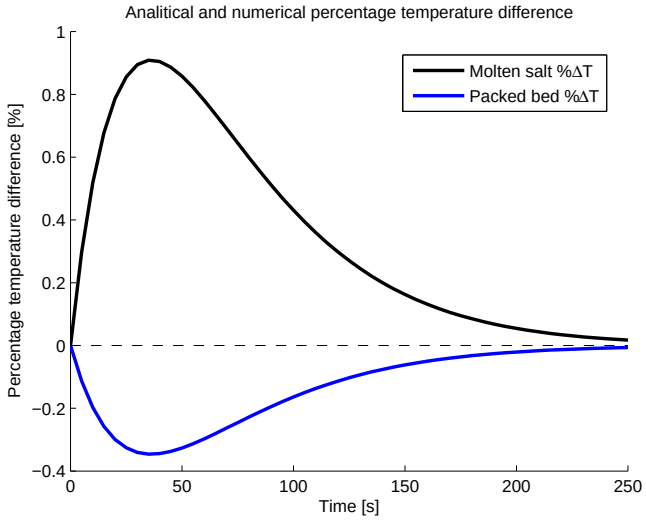

Figure 4-8: Molten salt - packed bed heat transfer. Estimated error

As a proof, the packed bed temperature and the molten salt temperature are tracked during the simulation of the Pacheco experiment (section 3.3) (Figure 4-9). Temperature difference between the molten salt and the packed bed is very little: the maximal temperature difference after 2 hours of discharge is just 1.16 °C (Figure 4-10). This result is also in agreement with the results of Xu et al., who founded that temperature difference between molten salt and is usually in the range $0{,}1\ °C < \Delta T < 2{,}5\ °C$ [12].

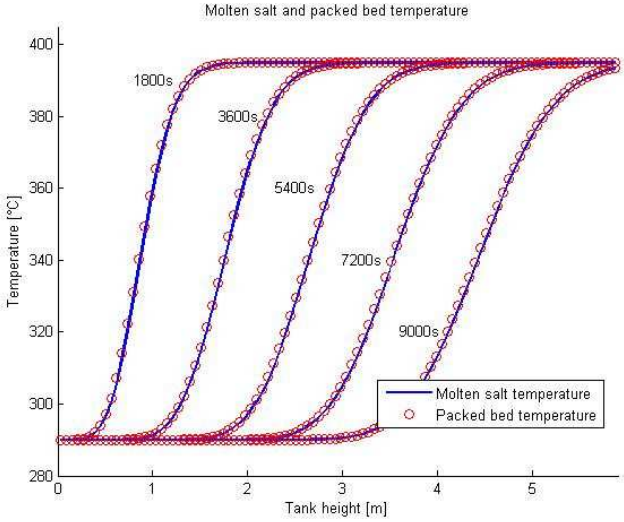

Figure 4-9: Temperature of the molten salt and of the packed bed during withdrawing of hot molten salt at 0,5h, 1h, 1,5h, 2h and 2,5h

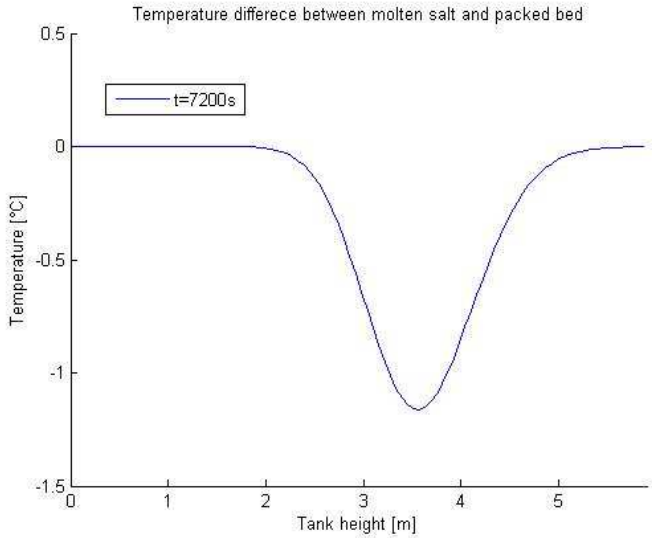

Figure 4-10: Temperature difference between packed bed and molten salt at t=2h

4.3.4 Axial advective transport and axial diffusion

Only axial advective transport and axial diffusion of the molten salt are considered. So, radial diffusion and heat transfer with the packed bed neglected. This problem is called advection-diffusion equation eq. (4.43). Adiabatic boundaries conditions are imposed at $z \to \infty$; also initial temperature is known.

$$\begin{cases} \rho c_p \dfrac{\partial T_{ms}}{\partial t} + \rho c_p u \dfrac{\partial T_{ms}}{\partial z} = \dfrac{\partial}{\partial z}\left(k \dfrac{\partial T_{ms}}{\partial z}\right) \\ T(z, t=0) = T_0 \\ T(z=0, t) = T_{in} \\ \left.\dfrac{\partial T_{ms}}{\partial z}\right|_{z\to\infty, t} = 0 \end{cases} \tag{4.43}$$

T_{in} is the temperature at the entrance of the tank and T_0 the temperature of the molten salt at $t = 0$. This problem has an analytical solution found by Ogata-Banks in 1961 [49]. The Ogata-Banks equation is largely used for hydrological purposes, such as contaminant diffusion and advection underground. Thanks to the similitude between heat and mass transfer, the Ogata-Banks equation can be applied also in our heat transfer problem [49]:

$$T_{ms} = \frac{T_{in} - T_0}{2}\left[erfc\left(\frac{x - ut}{\sqrt{4\alpha t}}\right) + e^{\frac{ux}{\alpha}} \cdot erfc\left(\frac{x + ut}{\sqrt{4\alpha t}}\right)\right] + T_0 \tag{4.44}$$

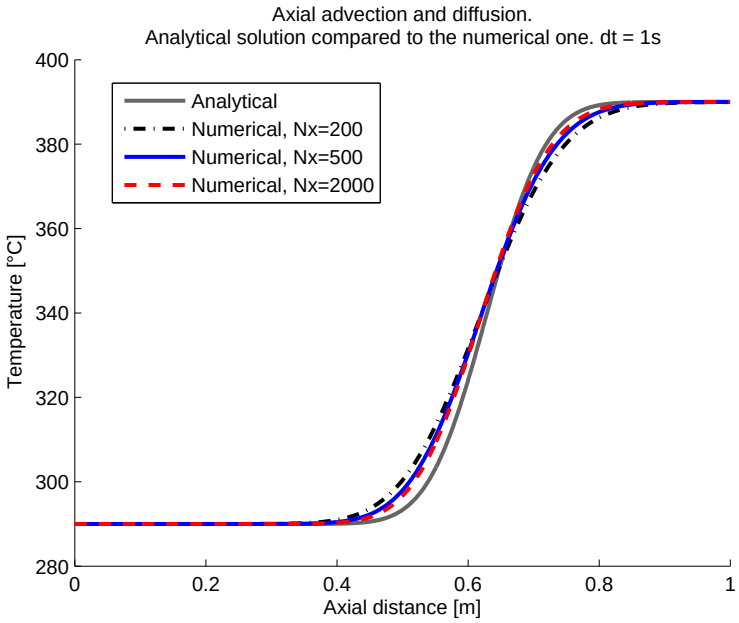

Figure 4-11: Axial advective transport and axial diffusion. Analytical and numerical solution

The analytical solution is compared to the numerical model. Physical properties are assumed as constant. Convergence is obtained when the number of nodes is above a certain threshold value. In this case, it can be seen that 500 nodes are sufficient to achieve satisfactory precision (Figure 4-11): the difference between the numerical and the analytical solution is below 8°C (Figure 4-12) but finer meshes are pointless as they are computationally onerous and they do not add much precision.

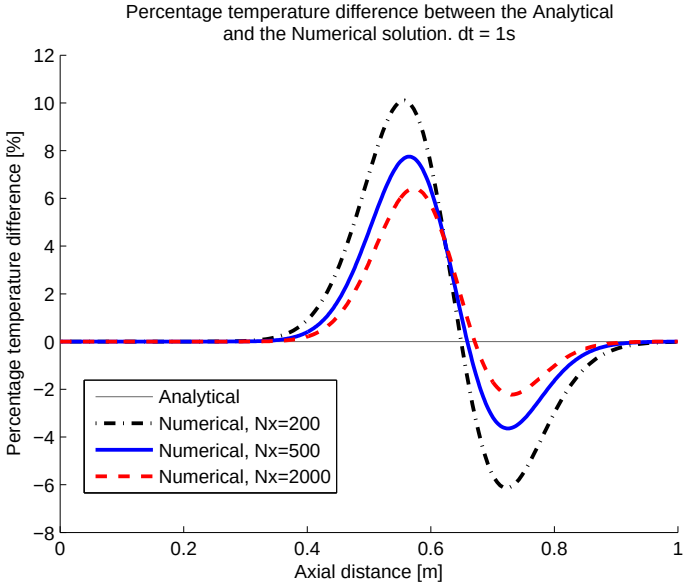

Figure 4-12 : Axial advective transport and axial diffusion. Estimated error

The dependence of the solution on mesh size accords with the researches of Zurigat and al. [58]. Zurigat developed a model, called Sharp, for thermocline water tanks. Zurigat observed that a decrease in the number of nodes lead to a less precise results. With few nodes mixing of molten salt in enhanced and stratification worsened (Figure 4-13).

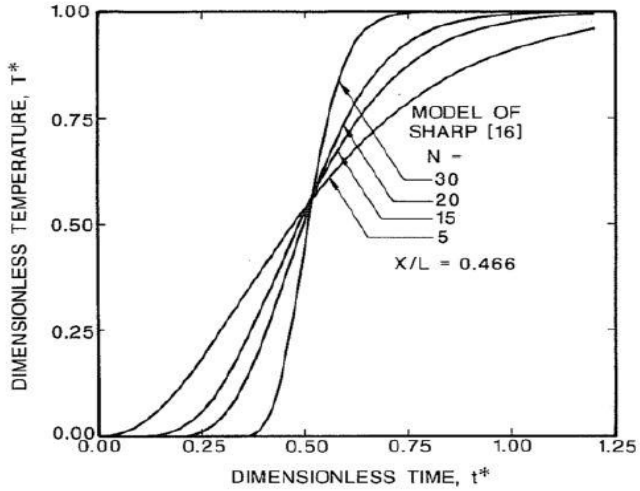

Figure 4-13: Mesh dependence – Sharp model [58]

An infinite number of nodes is required to perfectly simulate the thermocline. As the choice of an infinite number is not realistic, a mesh of 500 nodes is considered as enough accurate.

4.4 Molten salt physical properties – Sensitivity analysis

Molten salt physical properties are studied to understand how they affect thermocline development. Physical properties involved in the model are four: viscosity, density, thermal conductivity and specific heat. These properties are studied for three molten salts: solar salt, Hitec and HitecXL. Properties appear to vary much with temperature (Figure 4-14, Table 4-1). The temperature range of 300°C – 500°C is chosen because it is the target temperatures rise of a molten salt in thermocline TES systems in CSP plant. The analytical formulae for the evaluation of physical properties are presented in Appendix-D.

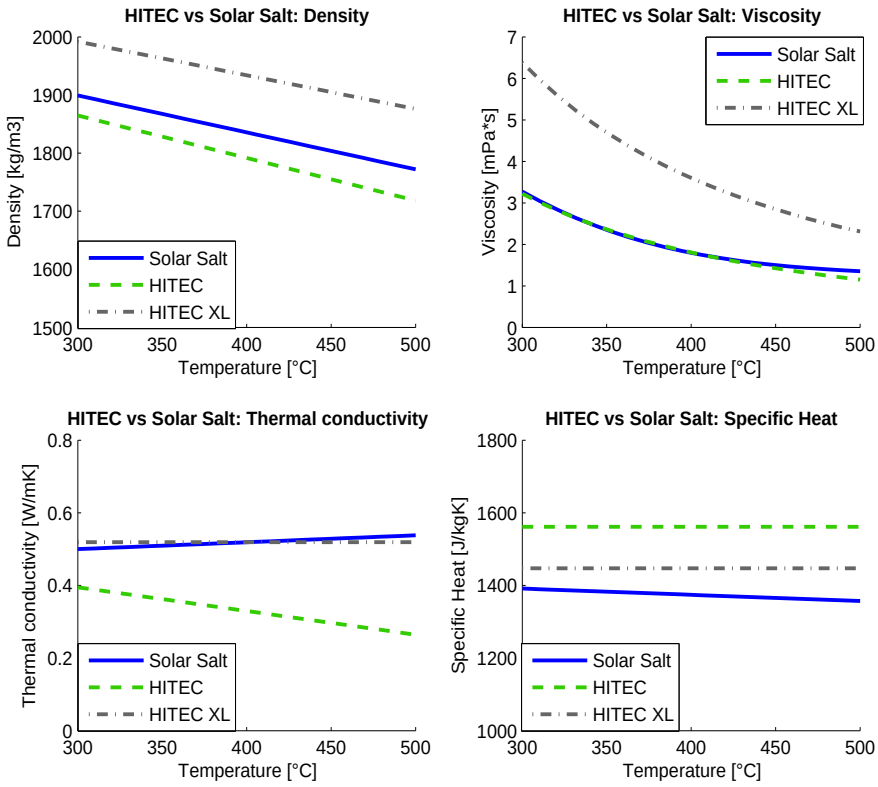

Figure 4-14: Comparison of solar salt, Hitec and HitecXL physical properties at temperature ranging 300°C – 500 °C

Table 4-1: Solar salt, Hitec and HitecXL physical properties at temperature of 300°C and 500 °C

		Solar Salt		Hitec		HitecXL	
Density [kg/m3]	@300°C	1899		1865		1992	
	@500°C	1772	-6,7%	1718	-7,9%	1876	-6,1%
Viscosity [mPa*s]	@300°C	3,27		3,22		6,38	
	@500°C	1,35	-58,7%	1,15	-64,2%	2,31	-63,8%
Thermal conductivity	@300°C	0,5		0,395		0,519	
[W/mK]	@500°C	0,538	+7,6%	0,264	-33,1%	0,519	0%
Specific heat	@300°C	1391		1562		1447	
[J/kgK]	@500°C	1357	-2,5%	1562	0%	1447	0%

Among these four properties specific heat shows very little dependence on temperature. This is why authors always consider specific heat as constant [12][11][14].

Viscosity is more than halved between 300°C and 500°C. However, in thermocline calculations viscosity is accounted only in the calculation of the Reynolds number, which is required for the volumetric heat transfer coefficient evaluation (h_v). Reynolds little influences h_v for two reasons. First, Reynolds is raised to the power of 0,6 when evaluating h_v. So, changes in viscosity are softened by this factor. Second, changes in h_v up to an order of magnitude little influence heat transfer between packed bed and molten salt and hence thermocline development (subsection 3.4.7). Summing up, viscosity could be reasonably assumed as constant.

Thermal conductivity of solar salt drops of one third, while the change for Hitec and HitecXL is little. Thermal conductivities below 25 W/mK little influence thermocline development, as discussed in subsection 3.4.6. As thermal conductivity of molten salt is always below 1 W/mK, it is reasonable to assume constant thermal conductivity.

Concerning density, the change in density is below 8%, but it cannot be considered as constant. To understand why, three simulations are performed:

1. @300°C: constant density of molten salt at 300°C is imposed (1865kg/m^3);
2. @500°C:, constant density of molten salt at 500°C is imposed (1718kg/m^3);
3. @VAR: temperature dependent density is considered.

Hitec molten salt is chosen. Mass flow rate of 0.8 kg/s of cold molten salt at 300°C is injected in the storage for one hour. Initial temperature of hot molten salt in the storage is 500°C. When properties are considered as temperature dependent, some mass is stored in the tank and the outlet mass flow might be slightly different than in the other two simulations at constant density.

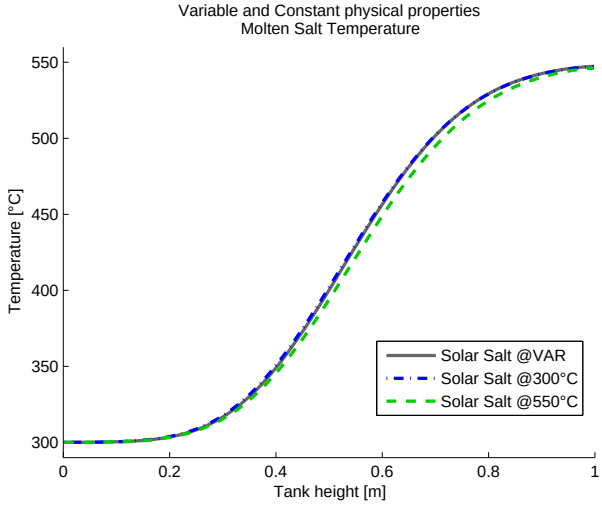

Figure 4-15: Temperature evaluated when density is considered as 1) constant: 1865 kg/m^3 2) constant 1718 kg /m^3 3) variable with temeprture

Density influences strongly thermocline development. The two constant-properties thermoclines are close, but the gap between the two increases with time (Figure 4-15). This is because the simulation @500°C is characterized by higher molten salt velocity. Indeed, molten salt has @500°C has low density and higher molten salt velocity is required to satisfy mass conservation. Concluding, density influences thermocline velocity and, thus, its position in the tank.

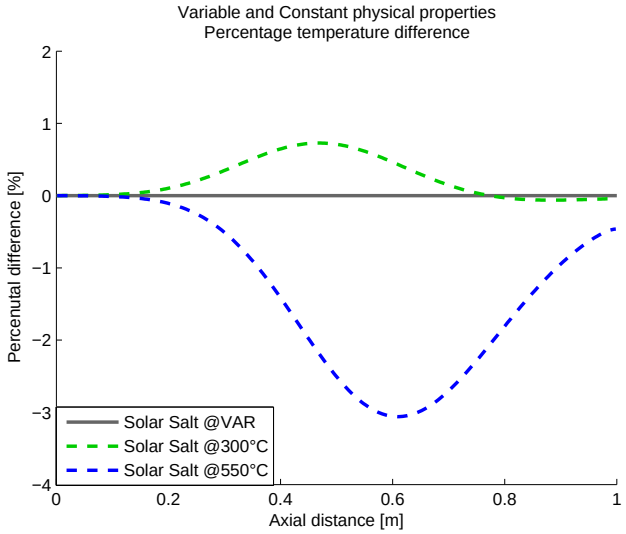

Figure 4-16: Temperature difference between @300°C, @500°c and @VAR simulations

The simulation @VAR is interposed between the two thermoclines of maximal and minimal density. More in detail, @VAR thermocline is very close to @300°C thermocline because inlet molten salt density and inlet molten salt velocity are equal for @VAR and @300°C; the maximum temperature difference between the two is less than 0.2% (Figure 4-16). At a certain point the thermocline @VAR is not anymore interposed between the other two: this is due to the change in density, the consequential mass stored in the tank and local change in molten salt velocity.

Besides, considering density as temperature dependent is very important on energy yields because energy stored in a thermocline TES is proportional to density. A difference in density of 8% between hot and cold molten salt corresponds to a difference of 8% in the energy stored (see Appendix-D). So, density is fundamental when studying energy stored in the thermocline and energy yield at thermocline boundaries.

Concluding, heat capacity, viscosity and thermal conductivity have little influence on thermocline development. However, density must be considered as variable because it influences the velocity of the molten salt in the tank and hence the shifting velocity of the thermocline. Moreover, density has a key role

when studying the amount of energy stored in the tank or the amount of energy withdrawn from it. All properties but density can be considered as constant.

4.5 Comparison with Pacheco experimental results

The numerical model is compared to the experimental data published by Pacheco [1]. Also Xu and Garimella compared their model with the experimental results of Pacheco [12][14]. Despite of that, they ran their models with different assumptions. For instance, Xu used solar salt while Garimella used Hitec. Further, packed bed properties were different: particle diameter was equal to 0.01905 m for Xu and to 0.091 m for Garimella. To double check our numerical model, two simulations are run: in the first one, data used by Xu are imposed; in the second one, data used by Garimella are taken. Both simulations are run with residuals of 10^{-4}, 5s time steps and a mesh of 500 axial nodes and 15 radial nodes.

On the left of Figure 4-17, the model of Xu et al. (red squares) is compared to Pacheco experimental data (scattered blue line). On the right of Figure 4-17, the new developed model (solid lines) and Pacheco experimental data (scattered lines). The lines of the developed model are practically identical to those of Xu et al. The developed numerical model fares very well and results are coherent with experimental data and Xu numerical work [12].

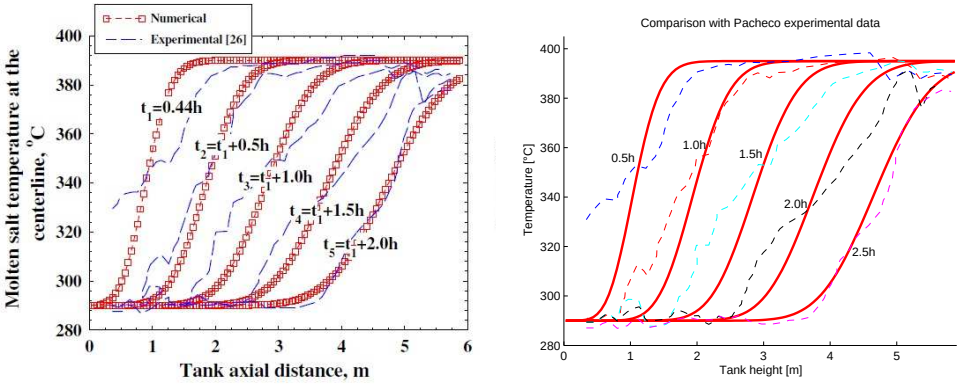

Figure 4-17: Pacheco experimental data compared to Xu's model (left) [12] and Pacheco experimental data compared to the new developed model (right)

Garimella gives only some of the parameters he set and some assumptions are made. However, estimated temperature distribution (red lines) well accords with both Garimella's model (black lines) and Pacheco's data (dashed lines) (Figure 4-18) [14].

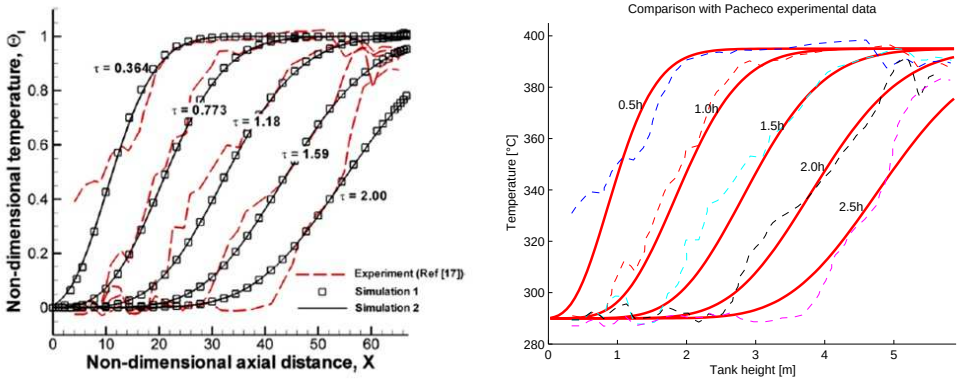

Figure 4-18: Pacheco experimental data compared to Garimella's model (left) [14] and Pacheco experimental data compared to the new developed model (right)

Summing up, the developed numerical model is in good agreement with both experimental data and numerical models previously developed by both Xu and Garimella. The numerical model is assumed to be correct.

4.6 Order of convergence of the numerical model

The model well agrees with both experimental data and analytical exact solutions. However, fundamental equations are solved through a numerical approximation and it is important to understand the dependence of the solution with mesh dimension and time step length. The study of the global error and of the degree of convergence helps estimating the maximum error committed in each simulation. The question is, is there any limitation on mesh dimension or time step length to obtain enough accurate results?

The numerical model intrinsically leads to inaccuracy. Analytical solutions showed that both axial heat diffusion and heat transfer between molten salt and particles are evaluated with very high degree of precision; global error is below 1% in both those two cases. Radial heat diffusion and advective transport were instead affected by higher errors. Radial heat transfer was characterized by very little local error, except near the wall where error boosted to 2.5%. Advective transport had great errors, ranging between 4% and 8%: the degree of precision depends on the mesh size.

4.6.1 Order of convergence - mesh dimension

Mesh dimension influences strongly the degree of precision. Indeed, an infinite number of nodes is required to fit the analytical solution (subsection 0). However, this is not possible because of computational limits and a number of 500 nodes is chosen as enough accurate.

To understand the degree of convergence of the solution when increasing the number of nodes, several simulations are performed with different mesh dimensions. Error is estimated as the maximum deviation between temperature evaluated with a certain mesh and temperature evaluated with the finest mesh tested. The order of convergence is O(Δz) (Figure 4-19, left). Thus, error is halved when the number of nodes is doubled (Figure 4-19, right). This was expected as discretization schemes are of the first order.

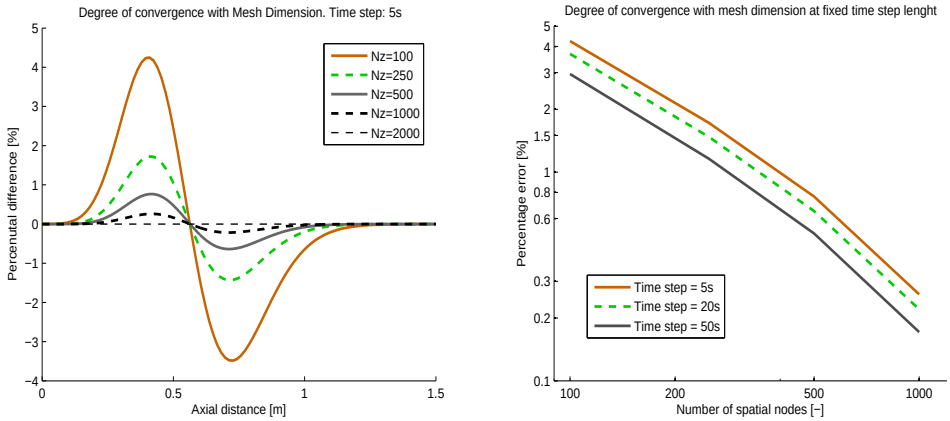

Figure 4-19: Left: estimated error at several mesh dimensions. Right: mesh dimension: estimated degree of convergence

4.6.2 Time step length

Also the effect of time step length must be analyzed. Indeed, fundamental equations are discretized in time with an implicit method. This allows setting the time step length with freedom, but nothing is known about the accuracy of results. Thus, which is the order of convergence for time discretization? Several simulations are performed changing only the time step length and the simulation with the littlest time step is supposed to be the most precise and it is taken as reference solution. Other simulations are compared to that one and the local error is estimated as their temperature difference. Maximum local error is used as a good approximation of the global error [55].

It is found that the order of convergence for time discretization is O(Δt) (Figure 4-20, left). This was expected as time is discretized with a first order implicit method. Global error drops below 2% for time step length below 20 s (Figure 4-20, right). All time step lengths below 20 s are then satisfying.

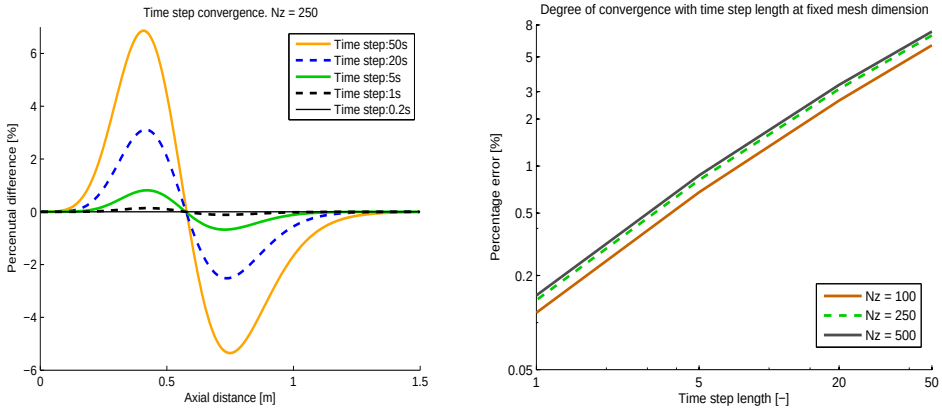

Figure 4-20: Left: estimated error for several time step length. Right: time step length: estimated degree of convergence

5 Thermocline TES issues

5.1 Thermal ratcheting

Thermal ratcheting is a critical phenomenon in thermocline thermal energy storage for CSP plant. Molten salt are daily injected at high and low temperature. This temperature swing induces great thermo-mechanical stress in the steel envelope (shell) of the thermocline tank. When heat is stored, the tank is heated up and the steel wall tends to enlarge itself due to thermal expansion of the metal: the internal volume of the tank increases. The particles of the packed bed can settle down in the void spaces left because of the tank dilatation, as showed in Figure 5-1. Maximum possible radial dilatation is 2,5 cm for direct molten salt thermocline TES of 10 meters of radius (linear expansion of solids, eq. (5.1)). When heat is withdrawn, the tank is cooled down but the steel shell is prevented to shrink because the particles hardly move back to their original position due to gravity. The steel shell is constrained and subjected to mechanical stress (traction) (Figure 5-2) [6]. If the strain overtakes the yield strength, plastic deformation occurs. As temperature changes cyclically, it might happen that plastic deformation propagates at each cycle reaching, eventually, the fracture point. This can lead to the failure of the tank because the steel envelope acts as primary structural support of the tank. Hence, tank must be designed in order to prevent plastic deformation of the steel [6].

$$\Delta R = R \cdot \alpha_{steel}\left[T_{max,steel} - T_{min,steel}\right] = \\ = 10\ m * 10^{-5}/K\ * (250\ °C) = 2{,}5\ cm \tag{5.1}$$

Only steel is considered, because stress in the insulation layers can be neglected. Indeed, those firebricks and ceramics are a set of blocks dispersed in a matrix and they give no structural support [6].

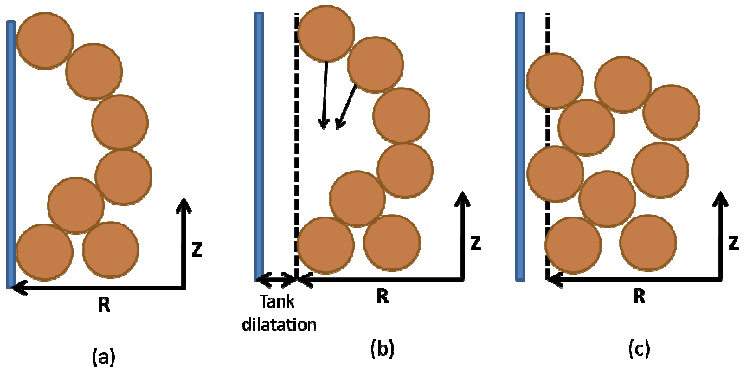

Figure 5-1: Fall of packed bed particles because of tank dilatation

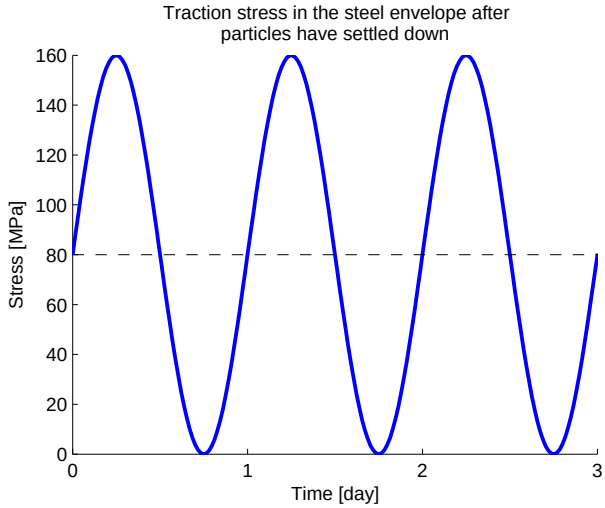

Figure 5-2: cyclic stress in the shell envelope

Hence, the tank is subjected to daily cyclical stress: when the tank is at maximum temperature, the shell tank is at its normal position and stress is zero. As the tank cools down, traction stress is induced in the metal (Figure 5-2).

Previous tests on thermocline storage energy systems showed that thermal ratcheting was under control and failure of the thermal storage did not occur. In Solar One solar tower power plant stresses were monitored confirming that thermal ratcheting was not a threat [59]. Also the test made by Pacheco and al. showed that thermal ratcheting was under control [1]. However, thermal ratcheting has to be considered when designing a thermocline TES and thermal stresses have to be carefully estimated in order to avoid an eventual failure of the tank.

The problem is simplified making three assumptions. First, fatigue is negligible. Each cycle lasts one day: as the tank is designed to last about 20 years, it is subjected to about 7000 stress cycles, which does not deeply decrease the yield stress of the material. Second, particles never go back to their original position after they occupied void space left by tank expansion. Also, packed bed is assumed to have infinite rigidity. This is conservative, as the shell tank is constrained to its new position and it cannot shrink anymore. Third, the wall is studied in order to stand thermal ratcheting but in order to structurally support the tank. Further studies are required to assess if the tank wall is a proper structure, or not.

Strain acting on the steel wall can be predicted with analytical strain relations [6]. The steel shell is constrained to the diameter it reached at the maximum temperature. In this condition, mechanical strain is composed of two parts: a mechanical strain connected to hydrostatical pressure of molten salt and packed bed in the tank and a mechanical stress induced by the thermal ratcheting

phenomenon (eq. (5.2)). The evaluation of the former requires the study of strain within the thin steel wall in axisymmetric coordinates. However, this mechanical stress can be neglected because it is 100-1000 times less significant than the stress induced by thermal ratcheting [6].

$$\sigma_s = \sigma_M + \sigma_T \tag{5.2}$$

To evaluate strain induced by thermal ratcheting, the maximal and minimal temperature of the steel wall during a charge/discharge cycle must be known (eq. (5.3)). The resulting stress must be lower than the yield strength in order to prevent plastic deformation. The ratio of the yield strength on thermal stress is named safety factor (eq.(5.4)) [6]. This factor of safety must be sufficiently lower than the value of one to ensure that thermal ratcheting is under control preventing the failure of the thermocline tank.

$$\sigma_{max} = \alpha_{steel} E\left[T_{max,steel} - T_{min,steel}\right] < \sigma_{lim} \tag{5.3}$$

$$f_{safety} = \frac{\sigma_{max}}{\sigma_{lim}} < 1 \tag{5.4}$$

The variation in temperature of the steel shell is assessed to be the critical parameter. A limitation of the temperature variation would correspond to less thermal stresses in the steel envelope and high safety factors. Hence, the design of the insulation layers must be accurately studied. For example, very thick internal layer of firebrick or thermal wool should be considered: this internal layer would represent most of the thermal resistance of the wall and most of the drop in temperature occurs in it. Thus, the steel shell is slightly affected by the temperature swing of the molten salt in the tank. Reversely, an increase in the thickness of the external layer or a decrease in external convection is not desired. Indeed, in this case the temperature of the steel would be higher and much closer to the temperature swing of the molten salt. Summing up, thick layers of internal insulating and thin layer of external insulating are preferred.

Garimella made accurate simulations in order to find the temperature of the steel wall at each axial location during several cycles of charge and discharge of the thermocline [6]. The wall studied by Garimella is structured by three layers: an internal layer of insulating firebricks or thermal wool, the stainless steel envelope and an external insulating layer made of ceramic. Properties of the wall are presented in Table 5-1. Garimella found that the maximum temperature variation in time of the steel shell occurs at about middle height of the tank, i.e. the zone where the thermocline is used to be located.

According to these results, the factor of safety was found to lie between 2 and 8 for the wall structures he tested [6].

Table 5-1: Wall tested by Garimella [6]

Layer	Material	Thickness [m]	Density [kg/m3]	Thermal conductivity [W/mK]
#1	Firebrick	0,2	2000	1
#2	Steel	0,02	8000	60
#3	Ceramic	0,1	1000	1

Unfortunately, the results of Garimella are neither transportable to other walls nor for thermoclines working under different conditions. Garimella imposed hot molten salt temperature at 450 °C and cold molten salt temperature at 293 °C [6]. Another temperature gap would lead to different thermo-mechanical stress in the wall, which cannot be directly evaluated. Moreover, Garimella used to charge and discharge molten salt to/from the thermocline every 12h. Obviously, a realistic thermal cycle would be of 24h: the thermocline is averagely hot for 12h and cold during the remaining 12h. As thermal cycles are longer, the wall has more time to warm up/cool down, i.e. there is more time to overcome the thermal inertia of the wall. Hence, littler factors of safety are expected when considering realistic 24h thermal cycles. Also, the factor of safety should decrease if the temperature gap between the hot and cold molten salt is increased, for example when using solar salt between 550 °C and 300 °C. Further, a change in the wall structure and wall materials would give different temperature distribution in the wall and consequently different thermal stresses. Concluding, an instrument to evaluate the factor of safety for any walls structure and any working condition of the thermocline TES is needed. To do that, the maximal temperature and minimal temperature of the steel shell have to be estimated. Once these values are found, eq. (5.3)-(5.4) are used to estimate the risk of thermal ratcheting.

Wall structures proposed further in this thesis are checked to have a factor of safety of at least 1. To forecast the factor of safety, an analytical method and a numerical method are developed. Both are compared with Garimella's results.

5.1.1 Thermal ratcheting safety factor - Analytical method

The analytical solution assumes that thermal capacity of the wall is negligible. This is a conservative method, because the temperature variation of the molten salt in the tank is not softened by the thermal inertia of the firebrick insulating layer. Neglecting the thermal capacity of the wall the problem becomes a simple stationary heat conduction problem. This method estimates

the factor of safety in the worst possible case, i.e. each temperature swing lasts an infinite time. Maximal and minimal temperature of the steel wall and the factor of safety are evaluated as in Figure 5-3 and in eq. (5.5). Young's modulus is set to 200GPa, thermal expansion coefficient of steel is set to 10^{-5} K^{-1} and yield strength is assumed as 200MPa (according to Garmiella's paper [6]).

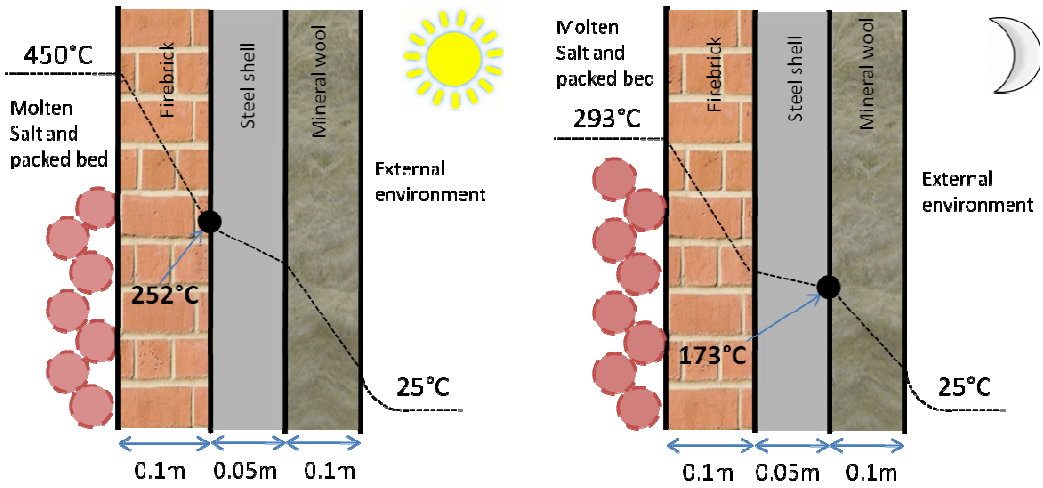

Figure 5-3: Maximum and minimum temperature of the steel envelope. Wall #1, Table 5-2

$$f_{safety} = \frac{\sigma_{lim}}{\sigma_{max}} = \frac{\sigma_{lim}}{\alpha_{steel} E \left[T_{max,steel} - T_{min,steel} \right]} = \tag{5.5}$$

$$= \frac{200\ Mpa}{\frac{10^{-5}}{K} \cdot 200GPa[252°C - 173°C]} = \frac{200MPa}{158MPa} \cong 1.26$$

Results are compared to Garimella's results in Table 5-2.

5.1.2 Thermal ratcheting factor of safety - Numerical method

The numerical model consists of including the wall structure in the thermocline finite volume model. The boundary conditions of the wall are: contact with the molten salt in the internal side of the tank; convection (free and forced) and radiation of external wall with the environment. Factor of safety of the analytical and numerical models are compared to those estimated by Garimella (Table 5-2). The percentage differences between the factor of safety estimated by Garimella and the factor of safety estimated by the developed model are always below 11%, which is considered as sufficient. This deviation is due to differences in the taken assumptions. Garimella made a more accurate simulation: Garimella considers a thermocline moving upwards and downwards

the tank every 6h. Instead, the developed numerical model imposes a constant molten salt temperature of 450°C for 6h and of 293°C for the following 6h (Figure 5-4). This is computationally simpler and less accurate. Besides, the model developed uses an approximation of the irradiative heat exchange with the environment, which affects results. As a result, estimated factors of safety (FS) show a deviation of 5-11% compared to the results of Garimella.

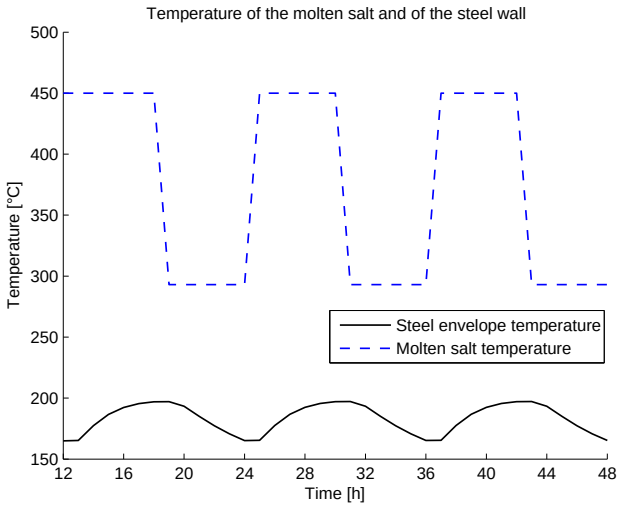

Figure 5-4: Temperature of the molten salt inside the tank and average temperature of the steel envelope. Wall #1

Table 5-2: Factor of safety (FS) estimated by Garimella, estimated with the numerical model and with the analytical method

	Thickness of: Fire brick [m] Steel [m] Ceramic [m]	Garimella FS [6]	Estimated FS, numerical model	Estimated FS, analytical model
Wall #1	[0.1; 0.02; 0.05]	2.44	2.64 (+7.6%)	1.26 (-48%)
Wall #2	[0.2; 0.02; 0.05]	7.75	8.72 (+11.1%)	1.79 (-77%)
Wall #3	[0.1; 0.02; 0.025]	2.57	2.64 (+2.7%)	1.52 (-41%)

The effect of the thermal inertia of the wall affects temperature profiles, which are not straight lines (Figure 5-5). This explains why the simple analytical evaluation of the wall temperature is not accurate enough. Indeed, factors of safety from the analytical solutions are very low quality. The analytical solution overestimates the temperature gap perceived in the steel wall, giving very conservative factor of safety. Analytical method was suitable if cycles are very long. Indeed, the factor of safety drops as temperature swing lasts longer. For example, for Wall #1, the analytical and numerical factor of safety are very close as the temperature half-cycle lasts 96h (Figure 5-6), which

is not the case for a thermocline TES. The factor of safety of 2.64 previously evaluated by Garimella (12h cycles) drops to 1.98 when 24h temperature swing is imposed. Thus, factors of safety need to be reevaluated for more realistic 24h thermal cycle.

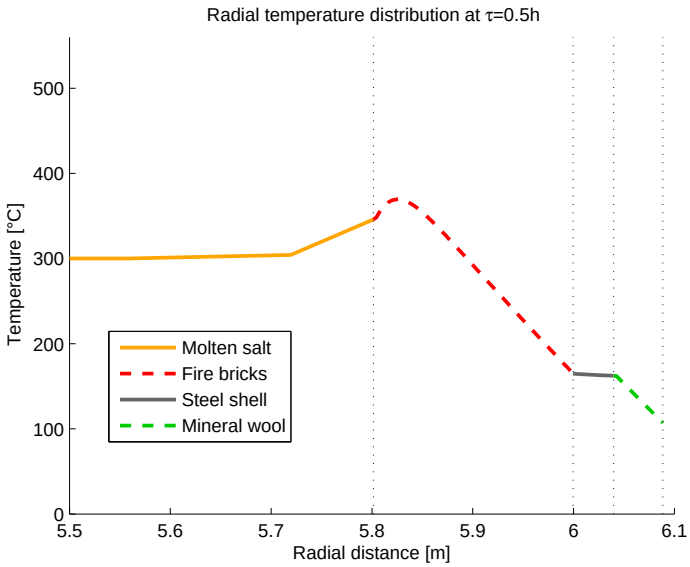

Figure 5-5: Temperature distribution in the wall at 0.5h after molten salt temperature passed from 450 °C to 300 °C. Temperature is far from being linear because of the thermal inertia of the wall. Wall #2.

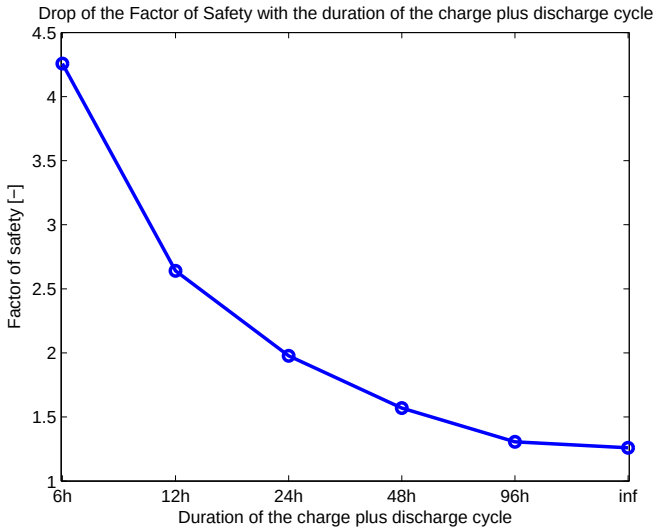

Figure 5-6: dependence of the factor of safety with the duration of temperature cycles. Wall #1

5.1.3 Proposed wall structures

The numerical model has been validated and now it is possible to study the thermo-mechanical stresses induced in several new wall structures and different molten salt temperatures. Solar salt are chosen and the new operational temperature is 550°C (charge) and 300°C (discharge). Cycles of charge/discharge last 24h. External wind speed is fixed at 2 m/s and emissivity of the external surface of the tank is set to 0.5. Diatomaceous bricks can be proposed as suitable candidate for the very low thermal conductivity and, hence, high thermal insulation: their thermal conductivity ranges between 0.11-0.23 W/mK [49] [60]. This is probably the material with the lowest thermal conductivity suitable for thermocline TES tank. Also, stainless steel AISI 302, 304, 316 and 347 have thermal conductivities ranging from 15.2 W/mK to 20 W/mK for temperatures between 127 °C and 327 °C. In Table 5-3 some wall structures and their corresponding factor of safety are listed.

Table 5-3: Estimated factor of safety of three proposed wall structure

		Layer 1	Layer 2	Layer 3	**Factor of Safety**
Wall #1 Low insulation	t [m]	0,1	0,04	0,05	**1,3**
	k [W/mK]	1	20	1	
Wall #2 Medium insulation	t [m]	0,1	0,04	0,05	**3,9**
	k [W/mK]	0,2	20	1	
Wall #3 High insulation	t [m]	0,3	0,04	0,15	**7,4**
	k [W/mK]	0,2	20	0,2	

Concluding, to avoid thermal ratcheting it is sufficient to add improve the insulating properties of the internal wall. The effectiveness of those walls as insulating structures is analyzed in subsection 5.3.2.

5.2 Thermal Stability of the thermocline - Fingering

It has been observed that the phenomenon of fingering and channeling is likely to occur in thermocline tanks [7]. This phenomenon is undesired as it causes molten salt mixing. Optimal thermal stratification in thermocline thermal storage tank is obtained if stability conditions are satisfied. The stability criterions are of two kinds: hydrostatical criterions and hydrodynamic criterions. Hydrostatical criterion concerns the different density between the hot fluid and the cold fluid. Hydrodynamic criterions limit molten salt velocity depending on the viscosity, density and permeability of the molten salt and packed bed [7].

5.2.1 Hydrostatical criterion

In thermoclines, the cold molten salt region is below the hot molten salt one: molten salt density is higher in the cold region and lower in the upper hot region and gravity prevents the formation of free convection vortex and vertical movement of the molten salt. Summing up, thermal stratification is naturally ensured by gravity and buoyancy forces [7].

5.2.2 Hydrodynamic criterion

Hydrodynamic criteria concern movement of molten salt in the porous medium. Those criteria limit molten salt velocity during charging or discharging process in order to avoid the fingering phenomenon [7].

The phenomenon of fingering is observed when a fluid immersed in a porous media displaces another fluid with different temperature and/or physical properties. For example, fingering might occur when hot molten salt displace cold molten salt. Due to different density and viscosity, less viscous hot molten salt tends to penetrates in more viscous cold molten salt, as in Figure 5-7. This creates a pattern of hot molten salt in a colder region, causing unwanted mixing of the molten salt and consequent depletion thermal energy. To optimize thermal stratification it is necessary to ensure that fingering happens only marginally in thermocline TES [7].

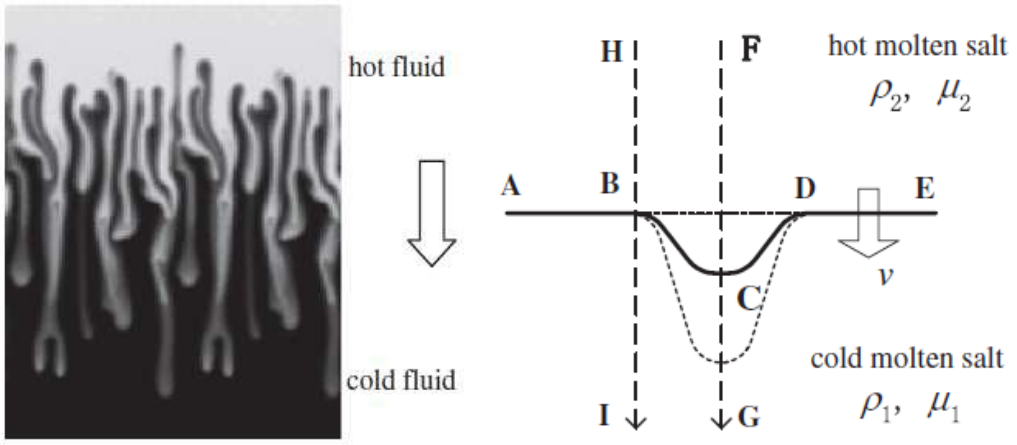

Figure 5-7: fingering phenomenon. Left: photo of the phenomenon: hot fluid penetrating in cold fluid. Right: schematization of the phenomenon [7]

Fingering and channeling are not observed if the mobility ratio is below the value of one [7]. The mobility ratio is the ratio between the momentum of the displacing and displaced fluid (eq. (5.6)). If the ratio is little, this means that the displacing fluid is more viscous and behaves as a “solider” medium, preventing fingering to take place.

$$M = \frac{K_2/\mu_2}{K_1/\mu_1} < 1 \tag{5.6}$$

When the tank is charged, the mobility ratio is above the value of one because the displacing fluid is the hotter and less viscous molten salt. Thus, fingering is supposed to happen. Contrarily, when the tank is discharged the mobility ratio is below one and fingering will not occur. Then, injection of hot molten salt (charging) is the critical process. However, fingering happens only under some conditions relied to the hydrodynamics of the flow [7].

When hot molten salt displace downwards cold molten salt (charging mode), random small bulges of hot fluid are formed at the interface between cold and hot molten salt (Figure 5-7, on the right). As hot molten salt are less viscous than cold molten salt, the bulge offers less flow resistance and behaves as a preferential path for hot molten salt. On the other hand, this path is in depression as it is full of light hot molten salt. As a consequence, gravity and buoyancy forces tend to move upwards and shrink this hot molten salt channel (Archimede's law). It must be determined which of the two factors is predominant, i.e. determining if channeling is supposed to take place. Qin analyzes the problem using the Darcy's law and Bernoulli's law (eq. (5.7)) [7]. As a result, Qin finds out that channeling is supposed to disappear quickly if the molten salt velocity (v_{ms}) is below a critical velocity v_c, as described in eq. (5.8).

$$\frac{P_{ms,hot} - P_{ms,cold}}{\delta x} = g\left(\rho_{ms,hot} - \rho_{ms,cold}\right) - \frac{v_{ms}\left(\mu_{ms,hot} - \mu_{ms,cold}\right)}{K} \tag{5.7}$$

$$v_{ms} < v_c = gK \cdot \frac{\rho_{ms,hot} - \rho_{ms,cold}}{\mu_{ms,hot} - \mu_{ms,cold}} \tag{5.8}$$

As above mentioned, during discharge process there are no limitation on molten salt velocity. Bulges randomly formed at the interface between hot and cold molten salt contains cold viscous molten salt. Contrarily to the previous case, bulges offer greater flow resistance and the cold molten salt is prevented to further penetrate the bulges. Furthermore, bulges of cold molten salt are heavier than the neighbor hot molten salt: thus, the bulges tend to flatten because of both gravity forces and buoyancy forces. To sum up, there is no molten salt velocity limit during a discharge process.

Some critical velocities are presented in Table 5-4. Critical velocity depends on the temperature difference between hot and cold molten salt, on the physical properties of molten salt chosen and on the permeability of the packed bed. The permeability is evaluated with the Kozeny-Carman formula, which depends on the porosity of the packed bed and on the diameter of the filler particles [7]. In a typical thermocline TES with a porosity of 0.22 and a particle average diameter of 2 cm, the critical velocity is found to be one hundred times

greater than the molten salt velocities typical of large-scale real thermocline TES system (respectively, 3,6 x 10^{-2} m/s and 4 x 10^{-4} m/s [12]). Such little molten salt velocities are required to optimize heat transfer between the molten salt and the packed bed and to prevent the thermocline to excessively expand. Summing up, fingering and channeling might occur only in packed beds with low porosity and very low particle diameter.

$$K = \frac{d_s^2 \varepsilon^3}{175 * (1-\varepsilon)^2} \tag{5.9}$$

Table 5-4: Fingering critical velocities for several particle diameters (D_s) and porosity (ε)

	D_s [m]	$\boldsymbol{\varepsilon}$	K x 10^7	v_c [m/s]
Solar Salt, 300-550°C	0.02	0.35	2.32	0.208
Solar Salt, 300-550°C	0.02	0.22	0.40	0.036
Solar Salt, 300-550°C	0.035	0.22	1.23	0.110
Solar Salt, 300-550°C	0.01	0.22	0.10	0.009

Concluding, buoyancy forces and gravity help natural thermal stratification in thermocline TES. Fingering is an unwanted phenomenon and it might occur when heat is stored in the thermocline TES. However, it occurs only if molten salt velocity overtakes a critical value. Instead, during discharge mode, channeling is prevented to occur and there is no molten salt velocity limitation. When designing a thermocline, preliminary evaluation of the critical velocity has to be done in order to ensure that fingering phenomenon is avoided.

The developed numerical model of the thermocline TES tracks the speed of the molten salt, controlling that the critical velocity is not reached. In that case, a warning message will be displayed but the simulation will not be interrupted.

5.3 Standby behavior of thermocline TES system

During nighttime the power block is turned off and molten salt are quiescent in the TES system. In this phase the thermocline TES is in standby mode and no mass flows through its boundaries. This standby phase lasts several hours, or even some days if the sky is overcast and little heat is collected at midday.

Two main effects are observed in standby thermocline TES. First, the thermocline tends to expand itself spoiling thermal stratification because heat at hot temperature naturally flows from the hot region towards the cold region. Second, heat flows through the wall of the TES towards the environment. Summing up, a study on both thermocline expansion and heat losses during standby mode is carried out [9].

5.3.1 Thermocline expansion during standby mode

Some assumptions have to be made to instigate thermocline expansion. The temperature distribution at the beginning of the simulations is set at 550°C in the upper half of the tank and at 300°C in the lower half. The choice of the temperature is arbitrary: thermocline expansion depends only on physical properties of molten salt and packed bed and not on the absolute value of the temperature [9]. Concerning the tank, a 14 m tall tank and a 21 m diameter is chosen. The tank is filled with solar salt and quartzite rocks with a vacuum grade of 0.22. Thermocline extension is defined as the region of the tank where molten salt temperature falls between 545°C and 305°C, i.e. the temperature gradient region.

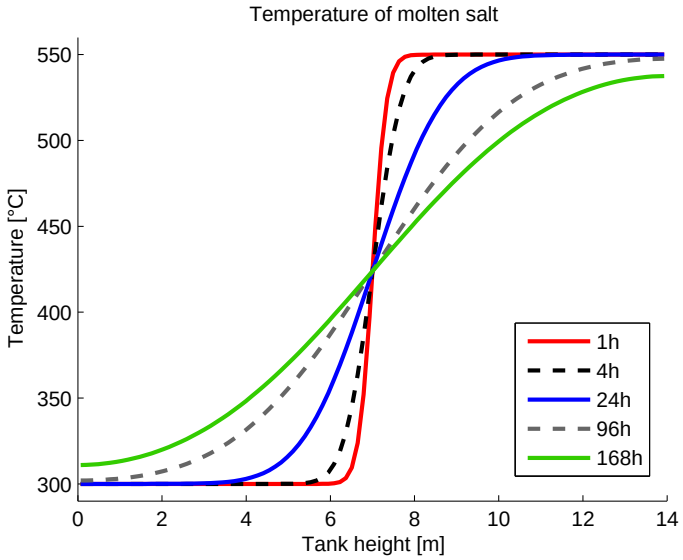

Figure 5-8: Thermocline expansion with time

Thermocline expands slowly and it is very steep for several hours (Figure 5-8). After four hours, the extension is quite little and most of heat is still available above the threshold temperature of 545°C. It is only after a 24 hours that the extension becomes significant. However, useful heat is still available after several days. It is only after a week that the thermocline occupies the entire height of the tank; at this point, no more useful energy is available.

The extension of the thermocline develops quite quickly during the first 10 hours of standby (Figure 5-9). Afterwards, the thermocline is fully developed and the expansion proceeds at almost constant speed. From interpolation, the expansion velocity is approximated to 6.6 cm/h. The thermocline occupies the entire height of the tank after about 7-8 days of standby: of course taller tanks would results in longer times, but 14 m have been assessed as the maximum height that can be achieved for a molten salt TES (subsection 3.4.4).

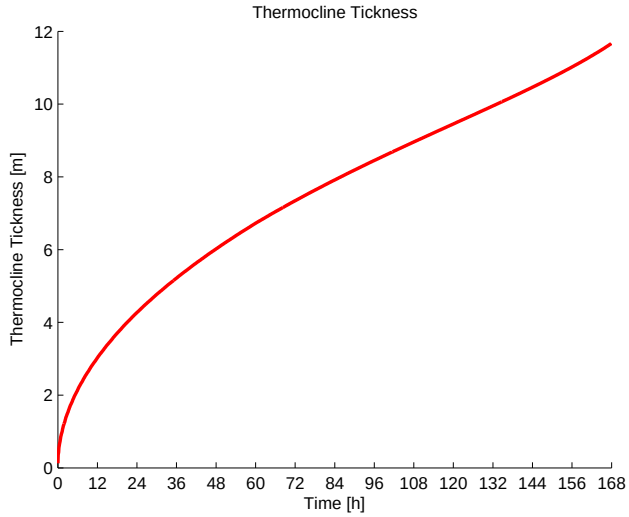

Figure 5-9: Thermocline thickness with time

The thermocline expands almost linearly with time during nighttime. For example, assuming 12 hours of nighttime standby, the thermocline will expand of about 0.8 meters:

$$\Delta x = v_{expansion} * t = 6.6\ cm/h\ * 12h = 0.8\ m \qquad (5.10)$$

To sum up, thermocline TES is left in standby mode for several hours during nighttime. In this period, the thermal gradient region expands itself because of heat diffusion. However, the overnight expansion of the thermocline region is

evaluated to be of about 0.8 m, which causes relatively little loss of the stored useful energy.

5.3.2 Heat loss to the environment

Thermocline TES is surrounded by the external environment, for it is subjected to heat loss. Molten salt temperature drops, especially near the tank wall, and useful heat is progressively lost. Heat loss rate depends on the wall structure and on external environmental conditions. Very thick layers of insulation limit heat loss, but they are expensive. At the same time, too poor insulation cause early depletion of the stored thermal energy. Also, wall must endure stresses caused by thermal ratcheting.

Three wall structures resistant to thermal ratcheting has been previously obtained in section 5.1 (Table 5-3). In this subsection, the insulation capacity of these three wall structures is investigated. Assumptions made are listed in (Table 5-5).

Table 5-5: Assumption made in simulations on environmental heat loss

External temperature	25 °C
Emissivity coefficient of external surface	0.5
Tank height	14 m
Tank radius	10.5 m
Porosity	0.22
Molten salt	Solar Salt
Freezing Temperature	220 °C
Initial temperature	Constant at 550 °C
Wind velocity	3 m/s

The work of Xu et al. [9] is taken as reference, however their results are considered as poor. Xu evaluates the convective heat transfer coefficient at the external surface of the tank with a correlation which is suitable for laminar flow. Instead, the flow is usually completely turbulent and characterized by very high Reynolds numbers. The tank is a cylinder but it can be properly considered as a flat plane because the radius is very large and specific correlations for cylinder result improper: Nusselt correlation for turbulent flow over a flat plate is chosen[49]. Besides, Xu considers only forced convection and he neglects both radiation and free convection heat transfer. Instead radiation can be even greater than forced convection, especially if the wall is poorly insulated. Concerning convection, it is found that heat transfer at the external surface of the tank is mixed, because:

$$\frac{Gr}{Re^2} \cong 1 \tag{5.11}$$

Hence, free convection cannot be neglected, especially when the tank is poorly insulated and the external wall heats up. Summing up, all forced turbulent flow, turbulent free convection and radiation heat transfer must be accounted.

Heat loss rate and radial temperature distribution of the molten salt in the tank are studied for all the three wall structures (Table 5-3). The "low insulation" wall is a poor choice because heat loss rate is great and molten salt temperature drops quickly near the wall. Temperature profile is steep because heat loss rate is great and energy stored in the middle of the tank has not enough time to be transferred towards the boundaries of the tank: in brief, heat diffusion is too slow compared to convective energy flux (Figure 5-10). Molten salt reaches freezing temperature after 138 h. So, "low insulation" wall is not recommended for thermal energy storage systems.

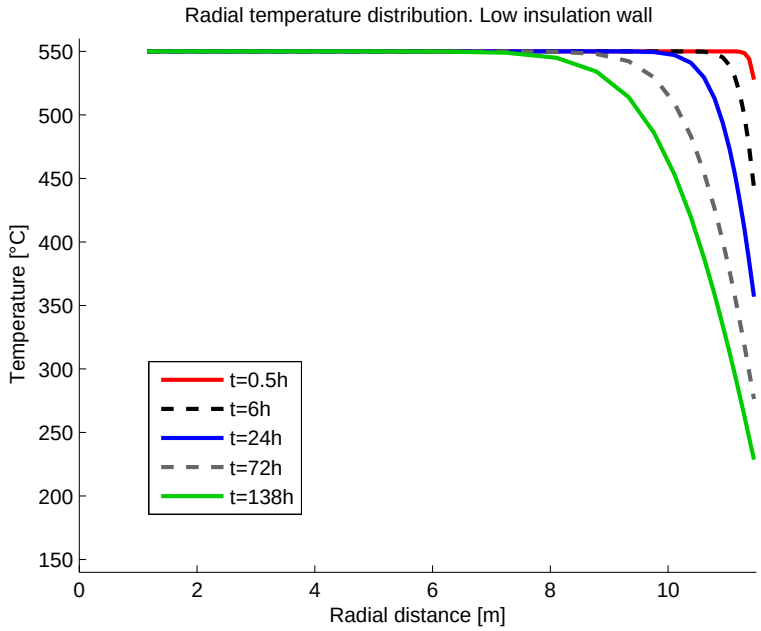

Figure 5-10: Radial temperature distribution. Low insulation

The "medium insulation" wall fares better (Figure 5-11). Radial temperature profile is almost flat after 24 hours. Salt is still molten after a week (168h), but radial average temperature is about 480°C, which is 70°C less than the initial temperature. The "medium insulation" wall structure is a possible candidate for TES systems.

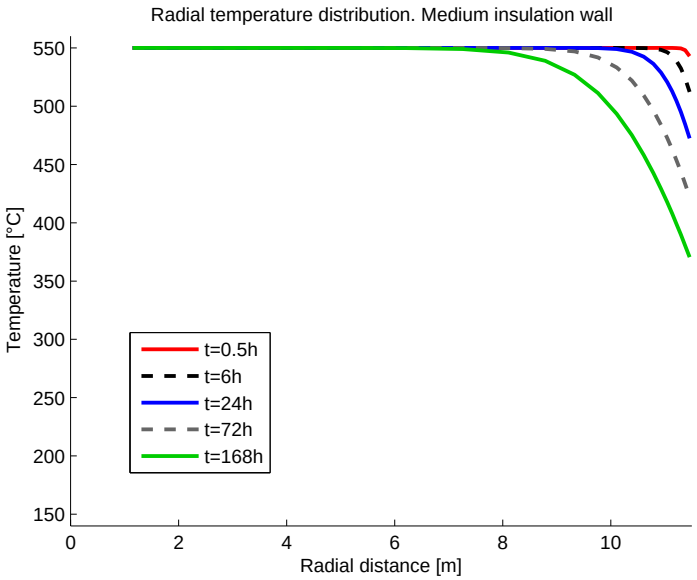

Figure 5-11: Radial temperature distribution. Medium insulation

Last, the "high insulation" wall structure is tested. This wall performs very well (Figure 5-12). Almost all thermal energy is still at very high temperature after 24h and radial temperature profile is almost still flat after a week. This is because heat loss rate is little.

For the "high insulation" wall the Biot number is close to 1, which means that diffusive heat conduction is as relevant as external convective heat transfer eq. (5-12) [49]. So, heat has enough time to be transferred from the centerline of the cylindrical tank towards the cool molten salt near the wall of the tank: as a result, temperature at the tank boundaries drops slowly.

$$Bi_{tank} = \frac{h_{conv}}{\frac{R_{tank}}{2} * k_{ms}} = \frac{2.82 \frac{W}{m^2 K}}{\frac{11.5}{2} m * 0.54 \frac{W}{mK}} = 0.91 \qquad (5\text{-}12)$$

However, the lumped capacitance method cannot be applied for $Bi > 0{,}1$ and radial temperature distribution cannot be considered as uniform. Concluding, this third wall structure gives very good insulation and it is definitely a good choice for thermocline TES systems.

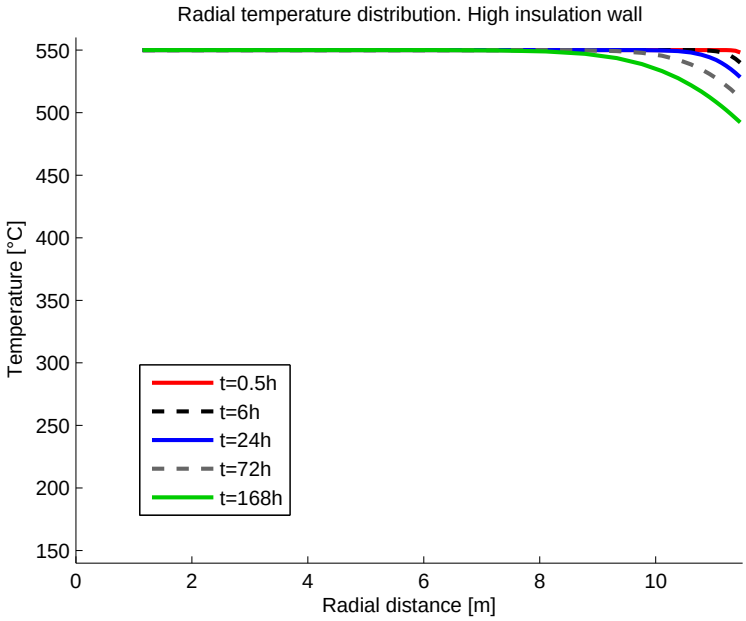

Figure 5-12: Radial temperature distribution. High insulation

5.3.2.1 Wind effect

Wind velocity affects slightly radial temperature distribution of well insulated tanks. Heat loss rate increases with wind speed velocity because forced convection boosts. To evaluate the effect of wind speed on heat loss rate, the three simulations are repeated increasing wind speed velocity from 3 m/s to 10 m/s.

Well insulated walls are almost not affected by the increase in external wind velocity. This is because the decrease in external convection and external thermal resistance is little compared to the total thermal resistance of the wall. The increase in wind velocity affects remarkably only the “low insulation” wall: in this case, molten salt freezes after 116.5 hours. Summing up, an increase in velocity little affects heat loss rate and radial temperature distribution in the tank. This result accords with Xu’s considerations [9].

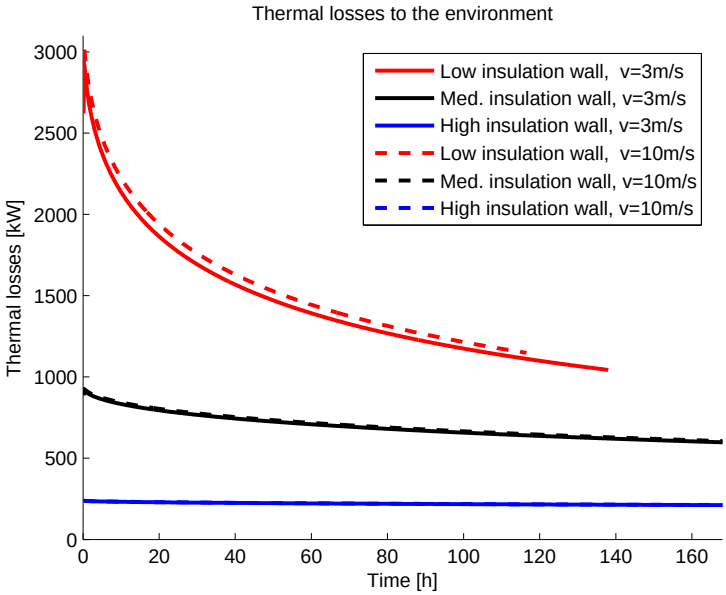

Figure 5-13: Heat loss rate for the three tested wall structures and its dependence on wind velocity

6 Optimal design of the thermocline

Compared to state-of-art two-tank TES, direct molten salt thermocline TES systems are cheaper compared to two-tank configuration because just one vessel is required and because the molten salt inventory is much reduced. However, performances of thermocline TES are expected to be poorer because a share of injected heat is depleted as hot and cold molten salt are in contact. The understanding of thermocline TES performance is fundamental to estimate the cost-effectiveness of the TES and to assess if thermocline TES could be more convenient than the state-of-art two-tank system.

A thermocline TES system is compared to a two-tank system. Data of molten salt mass flow rate in a CSP plant equipped with a two-tank storage are obtained from [8].Then, the two-tank TES of this CSP is replaced with a thermocline TES and the quantity of molten salt injected and withdrawn to/from the TES is kept unchanged. Hence, it is possible to simulate how a thermocline TES system behaves compared to a two-tank TES system.

The performance of the thermocline is evaluated defining a performance indicator: discharge efficiency. Discharge efficiency is the ratio of heat which is withdrawn above a certain threshold temperature on the total withdrawn heat (eq. (6.1)).

$$\eta_{disch} = \frac{Q_{with}@\ (T > T_{threshold})}{Q_{with,tot}} \tag{6.1}$$

Threshold temperature is arbitrary. In two-tank systems heat is steadily withdrawn at 550°C; hence, to compare the behavior of thermocline system with the two-tank system, a threshold temperature of 545°C is set. This temperature is very conservative, as the power block can elaborate heat also much below this value: a good sliding-pressure Rankine thermal cycle can accept heat up to 90°C below the nominal value (SEGS I, [2]). Thus, heat withdrawn from thermocline TES could be theoretically considered as useful if above the temperature of 460°C. However, as the goal is the comparison with a two-tank system, threshold temperature is set to 545°C.

In order to identify the thermocline which shows performance close to two-tank system, several simulations are performed. As starting point, simulations are run over a typical summer week with very high solar irradiance. As molten salt flow rate is given, it is tried to find the thermocline TES size which maximize the discharge efficiency, i.e. the size which maximize heat withdrawn at very high temperature.

Then, simulations are run on a typical early-spring week, when radiation is less intense and the weather is characterized by a couple of cloudy days. It is

important to understand if thermocline efficiency decays severely in these conditions. Winter season is not tested, as in those weeks little radiation is little available and TES systems are marginally used. In these conditions, discharge efficiency is too weather-dependent and hardly comparable with two-tank system efficiency.

Last, tests are run on thermocline tanks with fictive characteristics. As previously discussed, thermocline discharge efficiency is closely interconnected with the extensions of the thermal gradient: hence, several tests are performed to understand which parameters could limit thermocline expansion, hence increasing its efficiency. For example, thermocline expands due to thermal conduction: it is tried to set to zero thermal conduction of both molten salt and packed bed. Also, there is choice on molten salt type: solar salt, Hitec and HitecXL are compared. Again, tank height is changed over the maximum limit to assess how tank height affects the discharge efficiency. To summarize, it is tried to understand how the performance of the thermocline could be improved.

6.1 Simulation on a typical summer week

Simulation is ran on 9^{th} – 16^{th} July. Temperature of injected and withdrawn molten salt is tracked, as well as many other variables:

- Mass injected and withdrawn from the tank
- Temperature of injected and withdrawn molten salt
- Energy injected
- Energy stoked at useful temperature and total energy stored
- Heat loss to the environment
- Thermal energy prevented to be stored due to defocusing
- Energy withdrawn at useful temperature
- Injected and withdrawn exergy

Assumptions of the simulation are presented in Table 6-1. Heat loss is included in the simulations.

Table 6-1: Assumptions

Tank	
Molten salt	Solar salt
Physical properties	Temperature dependent
Filler	Quartzite rock + silica sand
Molten salt temperature range	300 °C – 550 °C
Full-load capacity	7.5 h
Thermal Capacity	914 MWh_{th}
Tank height	14 m
Diameter	23,6 m

Wall structure	High insulation (Table 5-2)
Emissivity of external tank surface	0.5
Other assumptions	
Mesh	400 x 10
Time step	15s
Temperature of external environment	25 °C
Week	09th -15th July
T threshold	545°C
P_{gross} of the power block	50 MW
Power block thermal efficiency	41%

An initial arbitrarily temperature is set in the tank. Afterwards, simulations are performed for 3-5 days until temperature stabilize and become cyclic. At this point, simulation on the desired week is ran (9th – 15th July).

Energy and mass fluxes are presented in Figure 6-1 and Figure 6-2. The weather is sunny all the week, except on 13th July and on 15th July afternoon when some clouds partially overcast the sky.

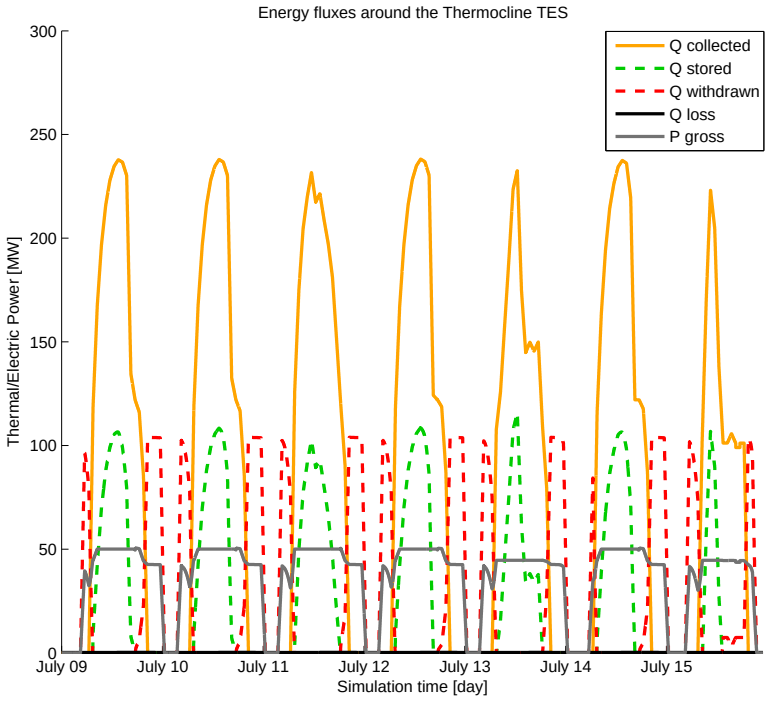

Figure 6-1: Energy yield in the CSP. 09th – 15th July

Every day, heat is withdrawn early in the morning to turn on the power block. When the sun rises on the horizon, the power block is driven by both thermal energy supplied form the solar field and thermal energy withdrawn from the

TES. At midday hours, extra thermal energy is available and it is stored in the tank, while the power block works at nominal power. Finally, late in the afternoon, withdrawing restarts and power supply continues for several hours, thanks to thermal energy stored at midday. The thermocline tank is not completely discharged when the power block is turned off: some thermal energy is left. So, the power block can be switched on the following morning before the sunrise. The same discussion can be extended to mass flow rates (Figure 6-2).

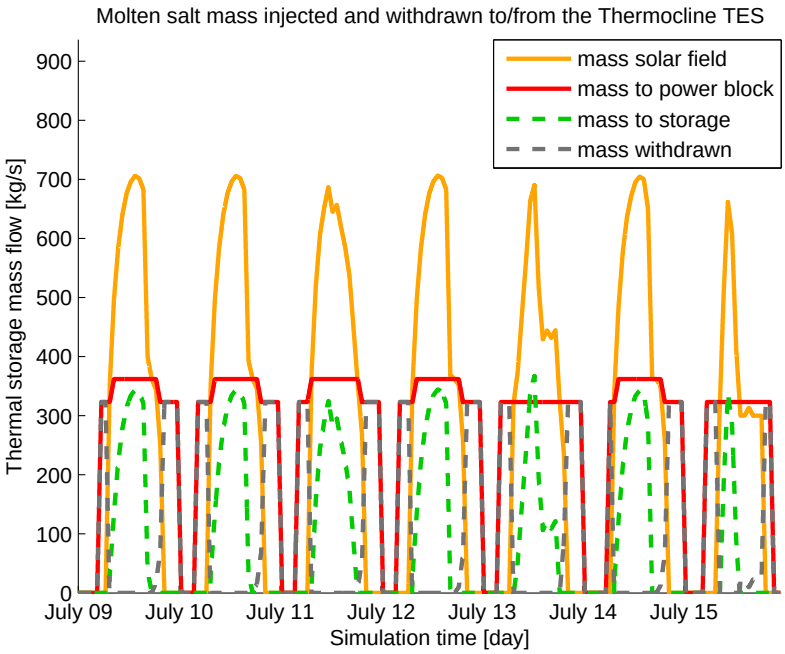

Figure 6-2: Molten salt mass flow. 09th – 15th July

Temperature profiles in the thermocline are presented for a typical day: 10th July (Figure 6-3). At 00:01, the power block is still on and molten salt are being withdrawn (yellow solid line). At 1:30, the power block is turned off and withdrawing is stopped; some molten salt is still above the threshold temperature of 545°C (green dashed line). Now, thermocline remains in standby and the thermal gradient region slightly expands (from green dashed line to gray solid line). Early in the morning molten salt are again withdrawn (around 4:30) to warm up and switch on the power block. At 8:30 solar radiation becomes sufficient to drive the power block and withdrawing is interrupted: thermocline tank is almost completely discharged (red dashed line). Since 8:30, extra thermal energy is available at the solar field and it is stored in the tank. Storing continues until 18:30, when the radiation becomes too poor and withdrawing restarts. The tank is almost fully charged (black solid line) and withdrawing of energy continues until 23:30, when the power block is turned off. During this period, the power block works at about 80% partial load (right plot, gray line). Again,

some thermal energy is left in the tank and it will be used to turn on the power block the following day before the sunrise (purple dash-dot line).

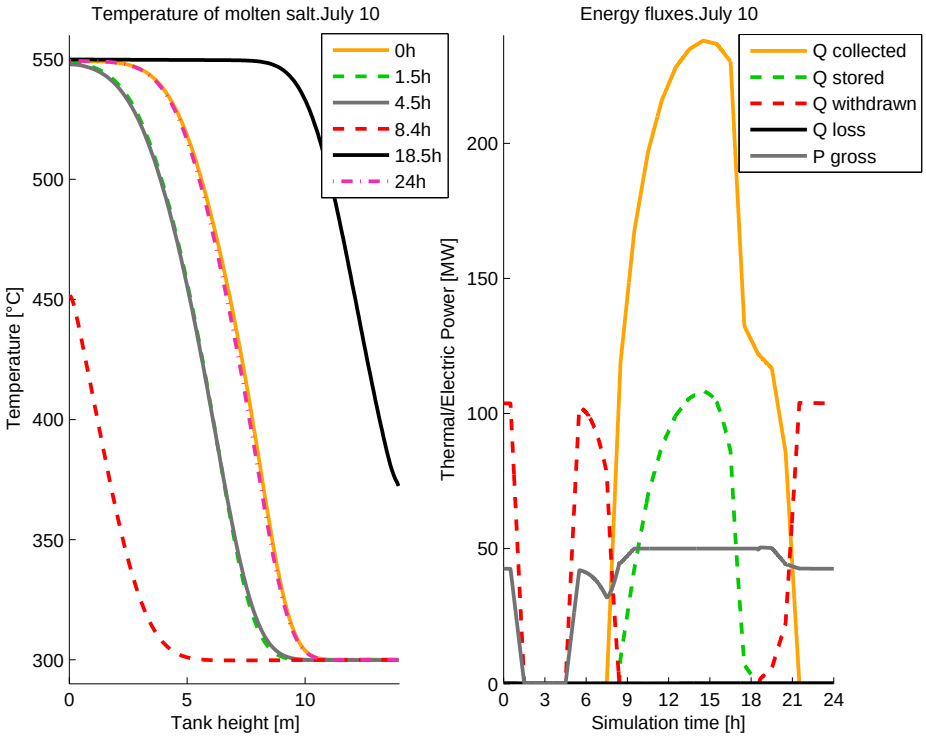

Figure 6-3. Left: Temperature distribution on 10th July in the thermocline at midnight, at the beginning of energy withdraing early in the morning, at the beginning of energy storage, at the beginning of energy withdrawn in the evening and again at midnight. Right: energy yield on 10th July.

This TES management, which was optimized for two-tank TES, is not correct for the thermocline: the power block is switched on too early in the morning and the thermocline does not manage to supply enough thermal power to drive it at nominal power from 4:30 to 8:30. Indeed, the thermocline reaches quickly the top of the tank and temperature drops. As a result, electrical power output decreases (right, P gross, gray line).

Thermocline extension is about 6 meters at midnight. The thermocline is quite steep because it has been partially reshaped twice: during discharge early in the morning the upper part of the thermocline partially left the tank (Figure 6-3, 8:30). When injection restarts, the thermocline reenters in the tank with a steep thermal gradient. So, the thermocline is partially reformed. The same happens late in the afternoon: at the end of hot molten salt injection the tank is almost fully charged (18:30); when withdrawing restarts, cold molten salt enters in the thermocline, the thermocline is reshaped and become steeper.

It is desired that the thermocline leaves the tank because the thermal gradient zone remains narrow and thermal stratification can be improved. However, when the thermocline leaves the tank temperature at the bottom or at the top varies much (Figure 6-4), causing problems in the rest of the CSP plant. On one hand, when tank is emptied, molten salt temperature drops progressively and the pressure of generated steam at the Rankine power block must be decreased progressively. For example, on 10th July morning (8:30) inlet molten salt temperature at the power block is as low as 450°C. On the other hand, when the tank is filled, temperature at the outlet of the tank increases. This warm molten salt is re-injected in the solar field, increasing average temperature of the solar field: this causes loss in performance of the solar field and the necessity of defocusing to avoid overheating of the solar field. Hence, the change in molten salt temperature must be controlled and some mirrors must be placed in stowed position. Temperature at exit of the TES reaches the maximum value of 370°C on 10th July afternoon (18:30).

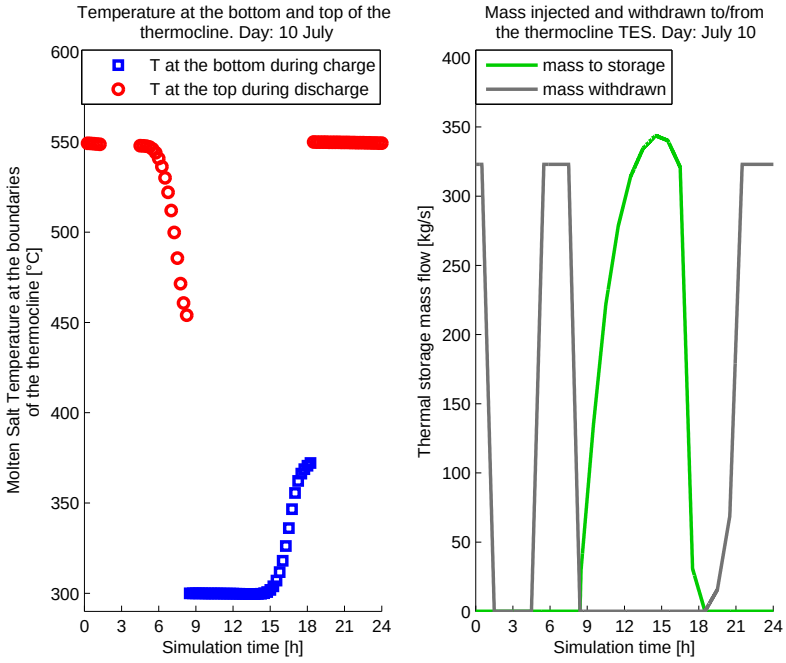

Figure 6-4. Left: Temperature at the inlet and at the exit of the thermocline TES.

Right: mass flow rate of injected and withdrawn molten salt to/from the thermocline TES

Energy yield are schematized in Sankey diagram (Figure 6-5). About 32% of the energy collected at the solar field is stored and used to extend electrical power supply. Thermocline TES has a significant impact on CSP operation: indeed, capacity factor of the plant is 77% and if there were no TES, it would be just 52%.

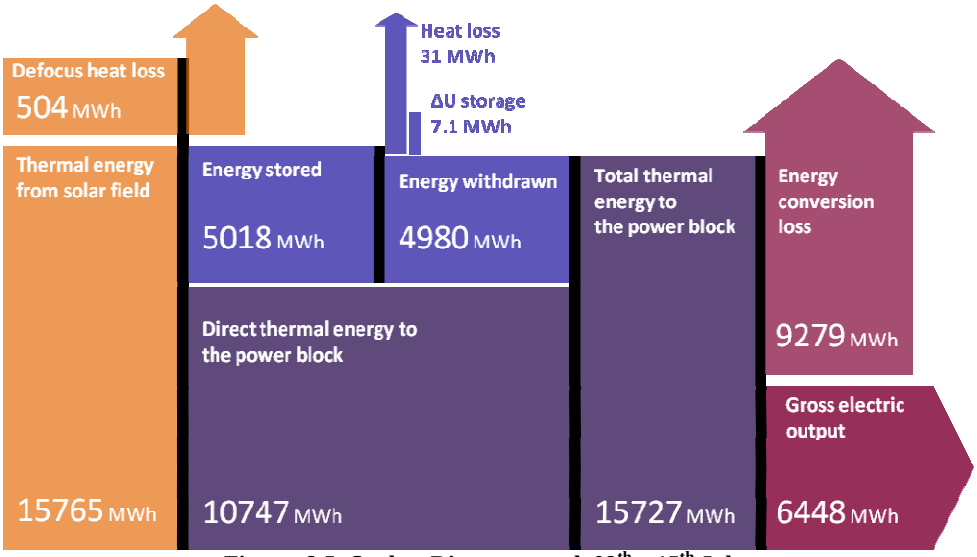

Figure 6-5: Sankey Diagram: week 09th – 15th July

Thermocline TES stores 5018 MWh_{th}. Of those, 4980 MWh_{th} are withdrawn and converted to electricity, 31 WMh_{th} are lost to the environment and 7 MWh_{th} are stocked in the tank over the simulation, i.e. the internal energy of the tank has changed between the beginning and the end of the simulation. Of those 4890 MWh_{th}, 3518 MWh_{th} are withdrawn at useful temperature ($T > 545°C$). Heat loss is assessed to be little relevant on overall energy yield: it is less than 1% of the total energy stored in the tank. Hence, the tank behaves almost as an adiabatic tank.

6.1.1 Optimal tank size

There is an optimal tank size and an optimal "solar multiple" (SF) which minimizes the levelised cost of electricity. To allow thermal storage the solar field must be oversized of a SF factor. In this way, some extra thermal energy is available at mid-day hours and it can be stored. A big field multiplier allows great thermal energy availability: this increases equivalent operating hours and lowers the levelised cost of electricity because the cost of the power block is better amortized. However, for a given TES size, the equivalent hours are not increased if the solar field is too much oversized: once the TES system is filled, defocusing takes place and extra thermal energy is wasted. To sum up, there is an optimal field multiplier for each TES size.

Also the size of the TES influences the levelised cost of electricity. Oversized thermal energy storage is pointless because it is rarely entirely filled and its potential little exploited. On the other hand, a little thermal energy storage forces to defocus frequently, wasting much useful thermal energy.

Hence, there is an optimal couple of values for "field multiplier" and thermal energy storage size which minimize the levelised cost of electricity.

The optimal SF and optimal TES size depend on several factors such as latitude, average solar radiation, CSP technology, solar field type, HTF, thermal storage type and configuration, etc. For example, the parabolic trough plant of Andasol I has field multiplier of 2 and a two-tank TES of 7h full-load capacity tank. It has been demonstrated that this FM and this TES size minimize the levelised cost of electricity [3].

In the simulation of section 6.1, tank size was assumed equal to 7.5h. In this section, the same solar field size is kept while the tank size is optimized.

Several simulations are performed on week 09th – 15th July changing thermocline tank size. The height of the tank is fixed to 14 meters and the size of the storage is determined by changing the diameter of the thermocline TES tank.

Interestingly, performance is worsened as the tank becomes larger. In little tanks, thermocline is very steep because it is reshaped frequently after fully discharge and charge of the tank, as previously explained. So, most of withdrawn energy is extracted at temperature above 545°C. For example, 80% of energy is withdrawn above 545°C from a 4h full-load capacity thermocline tank (aFigure 6-6). As the tank is larger, thermocline is less steep and the percentage of heat above 545°C decreases percentually.

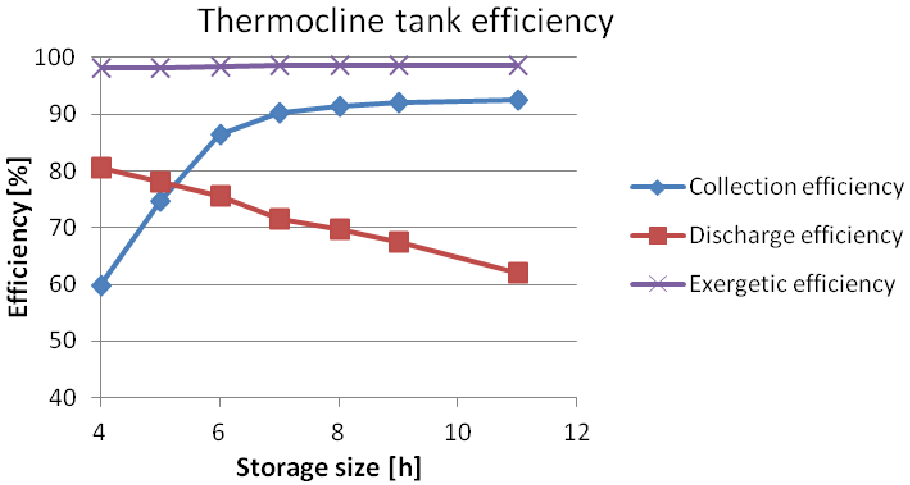

aFigure 6-6: Discharge efficiency and collection efficiency. 09th – 15th July

At the same time, little tanks are early filled with hot molten salt and many mirrors of the solar field must be defocused early. So, much energy is wasted and collection efficiency is low. Collection efficiency is defined as thermal energy stored on maximum thermal energy storable:

$$\eta_{coll} = \frac{Q_{sto}}{Q_{sto} + Q_{defocus}} \tag{6.2}$$

It is interesting to note that for big tanks, such as the 9h and as the 11h, collection efficiency is in the range 92-94%. This is because the thermocline occasionally reaches the bottom of the tank during charge process. When this occurs, molten salt leave the tank at temperature above 300°C ($T_{ms,out}$) (Figure 6-4) and this heat is dissipated at the solar field through defocusing:

$$Q_{defocus} = \dot{m}_{ms} * c_p * (T_{ms,out} - 300°C) \tag{6.3}$$

Instead, in a two-tank system molten salt are extracted from the cold tank steadily at a temperature of 300°C, and collection efficiency is 100%.

Little tanks have high discharge efficiency but they have a marginal role in the plant as little heat is stored; instead, bigger tank have higher collection efficiency of 92-94%, lower than the 100% of the two-tank system, but lower discharge efficiency. As a result, there is an optimal tank size which maximizes the amount of heat withdrawn above 545°C. This size 6h, but also bigger tank of 7h and 8h are good candidates (Figure 6-7).

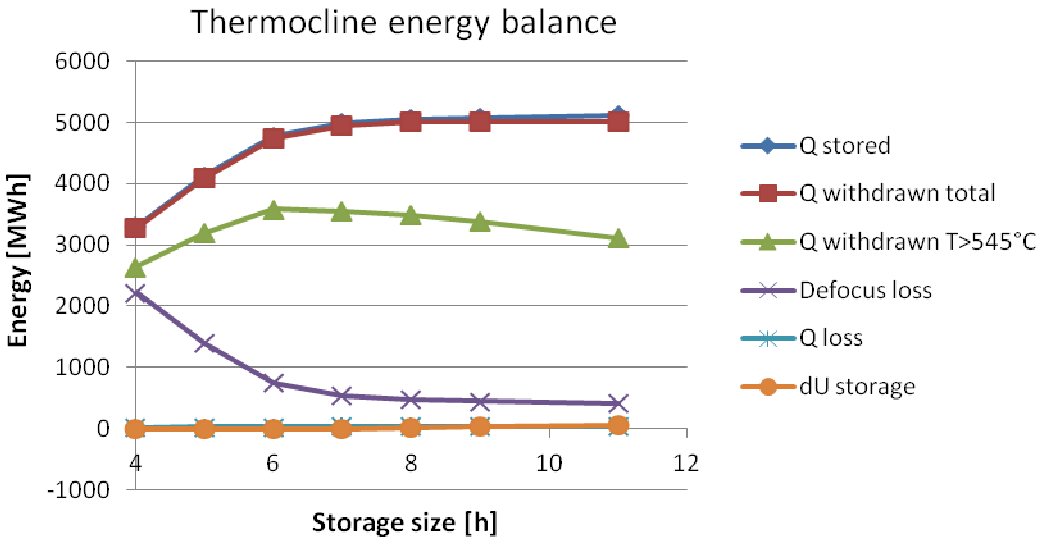

Figure 6-7: Energy yield of the thermocline TES for different thermocline sizes. 09th – 15th July

Besides, little tanks induce thermal stress in the solar field. The outlet temperature of the tank rises sharply when the thermocline reaches the bottom of the tank. This hot molten salt is mixed with the cold molten salt leaving the power block. However, average molten salt temperature increases and some

mirrors of the solar field are turned in stowed position. Moreover, the temperature withdrawn from little tank drops readily when the thermocline reaches the top of the tank, causing a sharp decrease in the available thermal energy and requiring a quick change in power block load factor. 7.5h is assessed as the best compromise between discharge efficiency, storage efficiency, and thermal stress at the solar field and at the power block.

Concluding, the two-tank TES system of a CSP plant is replaced with thermocline TES systems. Molten salt mass flow is unchanged; hence, thermocline is subjected to the same molten salt mass flow rates of the two-tank system. Optimal thermocline size is found to be 7.5h, which corresponds to a discharge efficiency of 70,6% and a collection efficiency of 90,9%. In this thermocline, stored energy is 5018 MWh_{th} and useful thermal energy is 3550 MWh_{th}. To compare, a two-tank system of the same size would store 5522 MWh_{th} and withdraw 5450 MWh of useful energy.

6.2 Simulation on a early-spring week

A second simulation is performed over an early-spring week. The week 23rd – 29th March is chosen. This is the first week after the spring equinox and it is characterized by much less radiation than in summer season. Also, during this week there are a couple of cloudy days and a day of zero solar radiation, because the sky is totally overcast; in this day the power block is not even switched on.

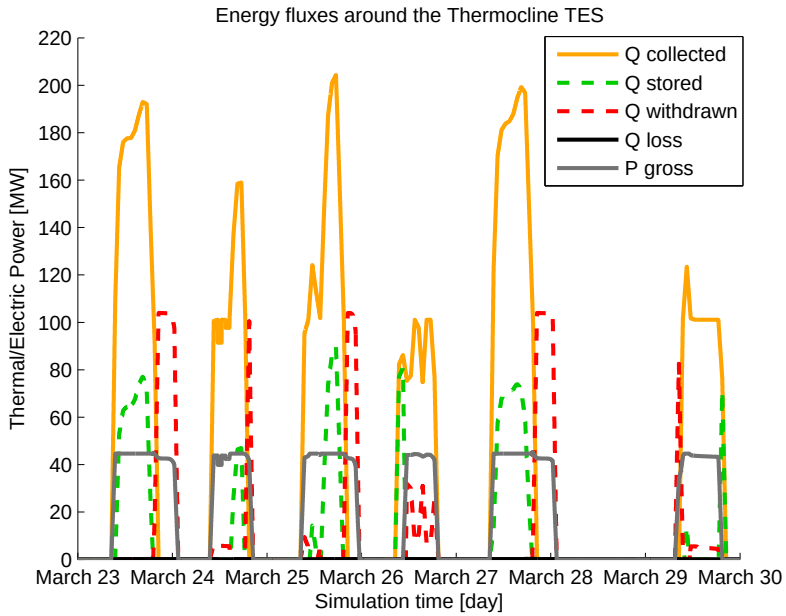

Figure 6-8 : Energy yield in the CSP. 23th – 29th March

Energy yield are presented in Figure 6-8. As said, radiant energy varies much day per day and the thermocline is managed much differently than in the summer. For example, the power block is never switched on early in the morning, except on 29th March. Also, energy is attentively stored and withdrawn, depending on sky conditions.

On 23rd March and on 27th March the sky is sunny and the CSP plant works at maximum power. Much thermal energy is stored and electric supply is extended of 5-6 hours after the sunset. In the other days of the week the management of the plant is much different, depending on the weather. For example, on 26th March radiation is always too poor to drive the power block (Figure 6-9); hence, thermal energy collected in the morning is entirely stored in the thermocline (from 8:30 to 11:10). Afterwards, the power block is turned on and it is fed with both thermal energy of the solar field and thermal energy withdrawn from the thermocline. The power block is turned off when all energy stored in the morning has been withdrawn. At this moment, the temperature of the thermocline is exactly as it was 24 hours before (yellow and black solid lines are almost overlapped). In other words, thermal energy is set apart in the morning and, once the power block is turned on, it is used as integration of the insufficient radiant energy.

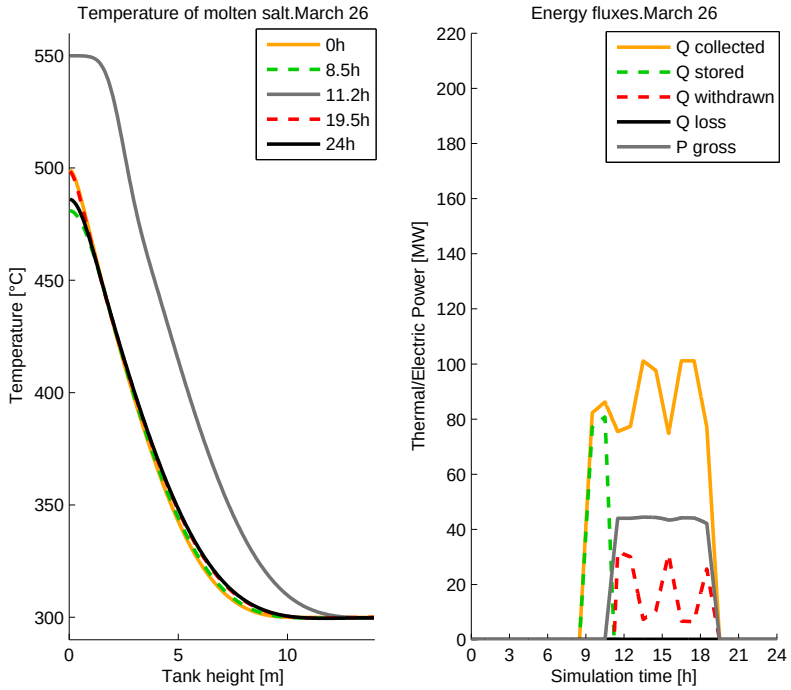

Figure 6-9 : Left: Temperature distribution on 26th March in the thermocline at midnight, at the beginning of energy sotrage in the morning (8:30), at the beginning of energy withdrawn at midday and again at midnight. Right: energy yield on 26th March.

On March 27th weather is good much thermal energy is stored and withdrawn for the thermocline TES (Figure 6-10). No molten salt at useful temperature is present in the tank at midnight (yellow line). At 8:30, injection of hot molten salt starts and continues until late in the evening (19:20, gray line). At this point, the thermocline TES is almost fully charged. Withdrawing starts and electricity generation continues steadily also after midnight: power production has been extended of about 5 hours.

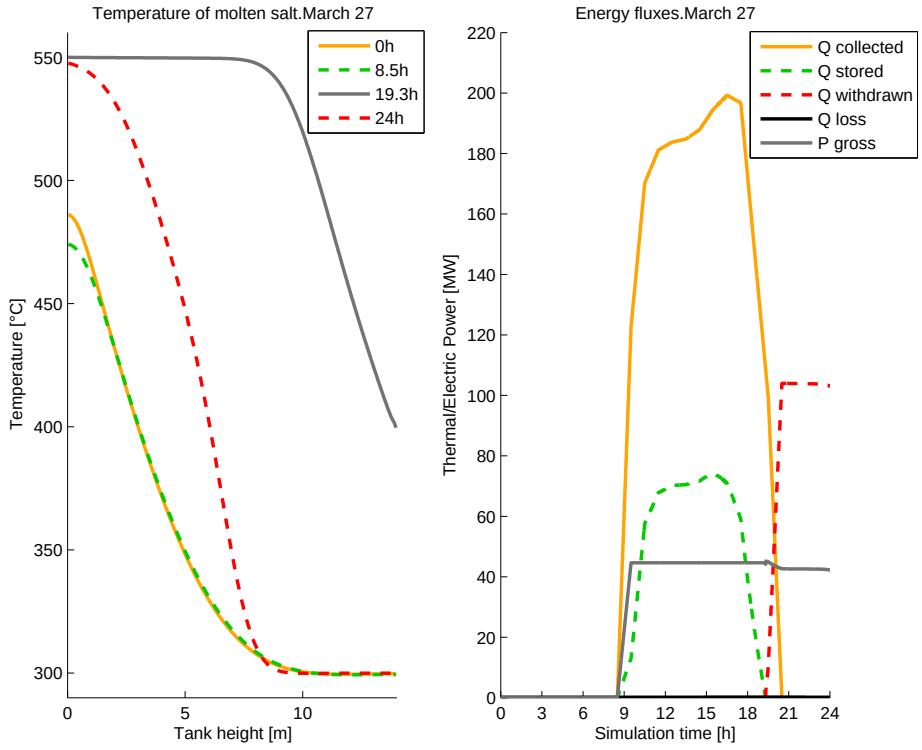

Figure 6-10: Left: Temperature distribution on 27th March in the thermocline at midnight, at the beginning of energy sotrage in the morning (8:30), at the beginning of energy withdrawn in the evening and again at midnight. Right: energy yield on 27th March.

On 28th March, there is no direct radiant energy and the power block is not event switched on. This day, the TES is in standby and the thermocline slowly expands.

As a result, on 23rd – 29th March the thermocline is used to flatten solar intermittency rather than for extending supply of electricity. The accurate management of the storage allows steady electric generation at nominal power for several hours every day.

6.2.1 Optimal size of the tank – spring season

The optimal size of thermocline tank in spring is assessed to be 6h (Figure 6-11). Indeed, much less radiant energy is available and larger vessels result oversized. Data concerning withdrawn energy are slightly affected by the change in internal energy (dU storage) and large tanks store some energy during the simulation: this energy is not accounted as withdrawn and hence it is not useful. Thermocline initial conditions should be manually arranged to flatten this change in internal energy and, hence, to obtain fully comparable data with the summer season.

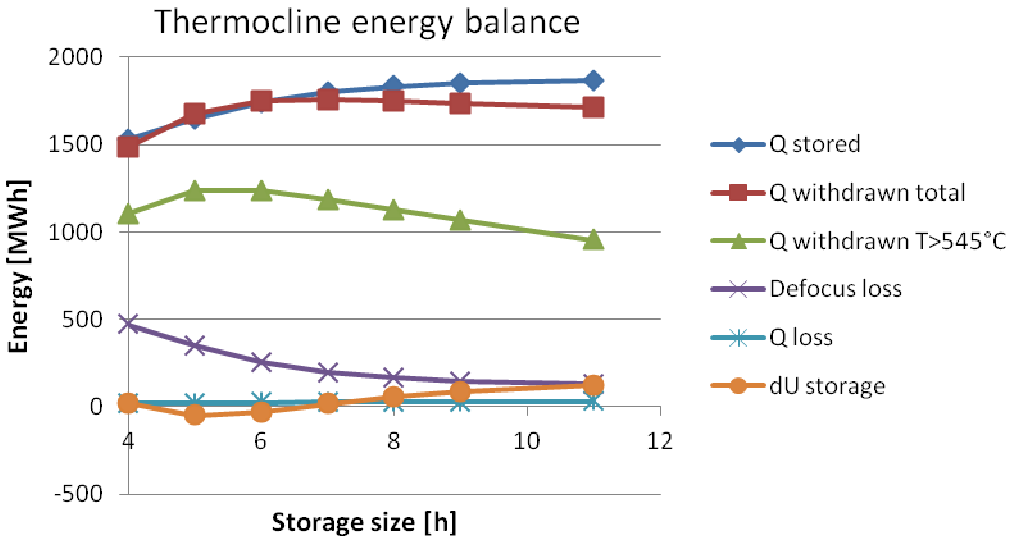

Figure 6-11: Energy yield of thermocline TES for different thermocline sizes. 23rd – 29th March

6.2.2 Comparison of thermocline TES performance: summer week and spring week

Compared to the summer week, in this spring week thermal energy collected at the solar field is almost half (Table 6-2). Indeed, much less radiation is available and thermal energy collected is just enough to feed the power block; only 22% of thermal energy collected is sent to the thermocline TES. Surprisingly, little defocusing is done also in spring: collection efficiency is 90,9%, which is equal to the collection efficiency of the summer week. Hence, the thermocline TES lead to some defocusing even in seasons with less solar radiation.

Table 6-2: Comparison of results: summer week and spring week simulations. 7,5h of full-load capacity

	Summer 9th - 15th July	Spring 23rd - 29th March
Q collected [MWh_{th}]	15765	8040
Q defocused [MWh_{th}]	504	181
Q stored [MWh_{th}]	5019	1818
Q withdrawn [MWh_{th}]	4980	1753
Q withdrawn useful [MWh_{th}]	3518	1154
Heat loss [MWh_{th}]	31	27
Electric output [MWh_e]	6448	3270
Load factor [%]	77	39
Load factor without storage [%]	55	31
Collection efficiency [%]	90,9	90,9
Discharge efficiency [%]	**70,6**	**65,8**

As the thermocline TES stores much less energy in spring than in summer season, it looks like the TES was oversized. As a consequence, the discharge efficiency of the thermocline TES slightly decrease, as explained in section 6.1.1: discharge efficiency drops from 70,6% to 65,8%. Hence, in spring less energy is stored and even less is withdrawn at useful temperature because of the lower discharge efficiency. However, the TES still improves significantly the load factor of the plant: load factor is 39%, but it would be just 31% if no thermal energy storage was added.

To sum up, discharge efficiency is lower in spring because less thermal energy is stored in the tank and, hence, the vessel behaves as an oversized vessel.

6.3 Improvement of thermocline TES performance

6.3.1 Discharge efficiency and threshold temperature

Low performance of the thermocline is closely connected to the chosen threshold temperature. It is observed that exergetic efficiency (eq.(6.4)) is very high in all cases and always above 97% (aFigure 6-6). This is because also heat extracted below 545°C is theoretically useful for thermal conversion with high efficiency. Unfortunately the power block is not able to elaborate heat at too low temperature: sliding-pressure Rankine cycles can work below the design temperature until a certain threshold temperature. Below this value, the power block is stopped.

$$\eta_{ex} = \frac{Q_{with}\left(1 - \frac{298}{T_{withdrawn} + 273}\right)}{Q_{stored}\left(1 - \frac{298}{550 + 273}\right)} \tag{6.4}$$

It is found that this threshold temperature influences deeply discharge efficiency and the performances of the entire CSP plant. A Rankine thermal cycle which can accept heat at low temperatures can exploit much more energy withdrawn from the thermocline thermal energy storage, boosting the effectiveness of the entire plant.

In Figure 6-12 energy withdrawn from the thermocline storage is ordered by its quality, i.e. by its temperature. Most of energy withdrawn is above 545°C yet many MWh are also withdrawn at very high temperatures, especially for big tanks (because of the less steep thermocline).

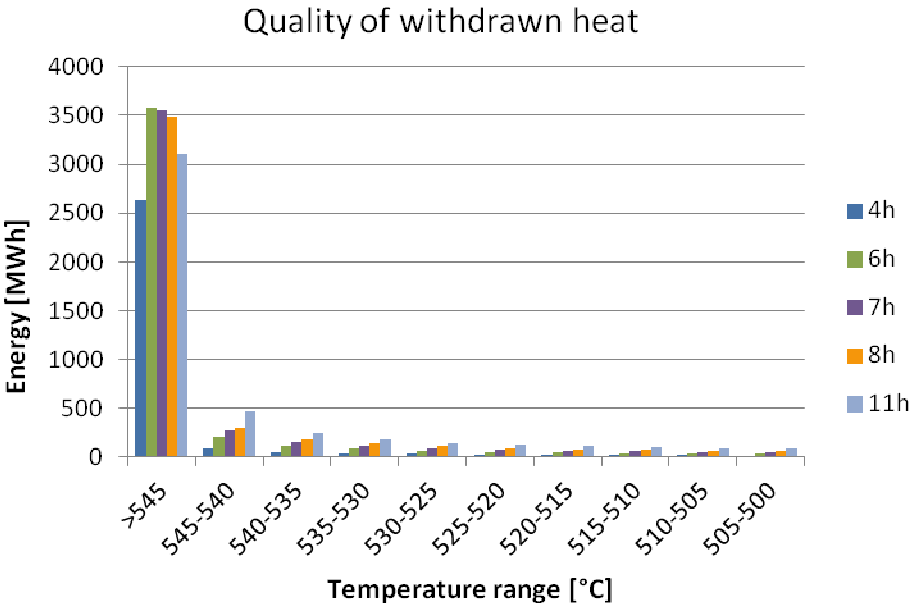

Figure 6-12: Quality of withdrawn heat for several tank sizes. 09th – 15th July

In Table 6-3 the change in discharge efficiency depending on the choice of the threshold temperature is presented. Efficiency is listed for vessels sizing 6h and 7.5h as well as depending on summer or spring simulation.

Table 6-3: Discharge efficiency depending on tank size, week chosen and threshold temperature. In bold the discharge efficiency of the simulation presented in section 6.1 and section 6.2

Discharge efficiency [%]	Summer week		Spring week	
Energy withdrawn above:	6h	7,5h	6h	7,5h
T>545°C	80,5	**70,6**	74,4	**65,8**
T>525°C	87,3	84,5	84,4	83,9
T>500°C	90,7	91,5	-	-
T>475°C	92,9	95,0	-	-

Littler tank show higher discharge efficiency, as expected (6h vs 7,5h). It is remarked that the threshold temperature strongly influences discharge efficiency. For example, the efficiency boosts from 70,6% to 95% when changing the threshold temperature from 545°C to 475°C (summer, 7,5h tank). This is however lee than the discharge efficiency of two-tank systems, which is always 100%.

As expected, discharge efficiency in spring is lower than in the summer, because the tank is only marginally used due to lower radiant energy. Discharge efficiency in spring is not presented for 500°C and for 475°C cases because the change in internal energy is about 7% of the entire total stored energy. Hence, results are affected and low accurate. Simulations should be re-run after a manual modification of the initial temperature.

As previously said, 545°C are a very conservative value. 545°C have been assumed because the aim of the simulation was the comparison with the two-tank system and molten salt must leave the thermocline at very high temperature. Instead, in real CSP plants molten salt are useful also at lower temperature. Power blocks can work with heat much below the nominal value: for instance, the power block of SEGS I was able to operate 90°C below the nominal temperature. If the threshold temperature is lowered, the power block manages to exploit much better the thermal energy stored in the thermocline TES. Assuming 475°C as the threshold temperature, it is found that discharge efficiency ranges 93-96% for the four case studied. So, most of injected energy is useful for power production.

Obviously, the comparison with the two-tank system is not valid anymore. Indeed it is impossible to compare the withdrawn energy from the two-tank system, which is always above 545°C, with the energy withdrawn from the thermocline, which is at temperature ranging between 475°C and 550°C. To compare those two systems, the electric output should be compared: thermal energy withdrawn from the two-tank system is converted steadily at nominal power block thermal efficiency, while in the thermocline case thermal-to-electric efficiency drops as the molten salt temperature decreases. The electric outputs should be compared to determine the overall efficiency of the two-tank system and of the thermocline systems.

Summing up, a decrease in the threshold temperature is beneficial for both discharge efficiency and for the entire CSP plant: discharge efficiencies above 90% are attained. However, it is not possible anymore to compare these efficiencies with those of the two-tank systems, because heat is withdrawn at different temperature and, hence, at different quality. To effectively compare those two systems, the electric output should be compared.

6.3.2 Molten salt choice

In this section two thermocline TES are compared: one using solar salt and one using Hitec. For solar salt, maximum temperature reached at the solar field is 550°C. In Hitec case, maximum temperature is 500°C.

Solar salt and Hitec thermal energy storages size 7,5 hours of full-load capacity; so, they have different physical dimension. Storage capacity is evaluated with eq. (6.5). Nominal power is 50 MW for both cases:

$$Q_{storage} = \frac{\dot{W}_{power\ block,nom}}{\eta_{power\ block}} * 7.5h = V_{storage} * \bar{c_p}\bar{\rho} * \Delta T \qquad (6.5)$$

Power block efficiency was set to 41% for solar salt. Hitec has lower thermal efficiency because maximum temperature is 500 °C, versus the 550 °C of solar salt. Thermal efficiency is assumed to 40% for Hitec case [61]. It is because of the different efficiency at the power block that thermal capacity of Hitec tank is slightly bigger than the solar salt one: 937 MWh_{th} versus 914 MWh_{th} (eq. (6.5)) (Table 6-4).

Concerning physical size of the tanks, Hitec tank is larger than the solar salt one because the temperature rise of Hitec is 200°C versus the 250°C of the solar salt case; this needs larger storage volumes (eq. (6.6)). As a result, solar salt tank sizes 23.7 meters of diameter and 14 meters tall, while Hitec tank is 26.4 meters large and 14 meters tall.

$$V_{storage} = \frac{Q_{storage}}{\bar{\rho}\bar{c}_p \Delta T} \qquad (6.6)$$

Table 6-4: Solar salt and Hitec and tank size

	Power block efficiency [%]	$Q_{storage}$ [MWh]	Temperature rise [°C]	$\bar{c_p} * \bar{\rho}$ [MJ/m^{3}K]	$V_{storage}$ [m^3]	Height [m]	Diameter [m]
Solar Salt	41	914	250	2,1348	6170	14	23,7
Hitec	40	937	200	2,2089	7640	14	26,4

Concerning costs, Hitec thermocline is certainly more expensive then solar salt one as it is bigger and because Hitec salt mixture is more expensive (Table 2-3). Summing up, solar salt tank is smaller and cheaper.

Despite of different storage sizes and molten salt types, energy stored and withdrawn to/from the two thermoclines is almost the same and, hence, discharge efficiency is the same (Table 6-5). To evaluate discharge efficiency, the same dimensionless threshold temperature is set for both solar salt and for Hitec. Dimensionless threshold temperature is defined as in eq. (6.7).

$$T_{threshold} = T_{low} + 0.98 * \left(T_{high} - T_{low}\right) \quad (6.7)$$

Table 6-5: Thermal energy storage energy yield. Simulation 9th – 15th July

	Thermal energy collected [MWh]	Energy stored [MWh]	Heat loss [MWh]	Threshold temperature [°C]	Energy withdrawn T>545°C/496°C [MWh]	$\eta_{discharge}$ [%]
Solar Salt	16268	5018	31	545	3520	70,6
Hitec	16268	5119	34	496	3598	70,3

Heat loss rates are similar. On one hand, Hitec tank has larger surface exposed to the environment than the solar salt one (+25%). On the other hand, the temperature difference with the environment is lower for Hitec.

The similar discharge efficiency is due to the almost identical behavior of the two thermoclines. First, the two molten salts have similar physical properties, as shown in Table 6-4. Interstitial heat transfer and thermal conductivity coefficient of the two salts are different, but they slightly influence the development of the thermocline, as said in section 3.4. Also, Hitec is characterized by almost the same Reynolds number than in solar salt case: mass flow rate is indeed weighted on its temperature rise, leading to greater Hitec mass flow than in solar salt case (eq. (6.9)).

$$\dot{Q}_{coll,Hitec} = \dot{Q}_{coll,solar\ salt} \quad (6.8)$$

$$\dot{m}_{ms,Hitec} = \dot{m}_{ms,solar\ salt} * \frac{\rho_{solar\ salt} * \Delta T_{solar\ salt}}{\rho_{Hitec} * \Delta T_{Hitec}} \quad (6.9)$$

However, Hitec has also larger tank diameter, which is also weighed on temperature rise (eq. (6.6)). So, molten salt velocities and Reynolds numbers are both very close in the two cases. Besides, the two cases are almost identical if the dimensionless temperature is considered [12]. They are not exactly identical, because dimensionless environment temperature is slightly different. However,

environmental temperature does not affect much results. As a consequence, dimensionless thermocline development is almost the same in the two cases (Figure 6-13) and TES discharging efficiency is almost identical.

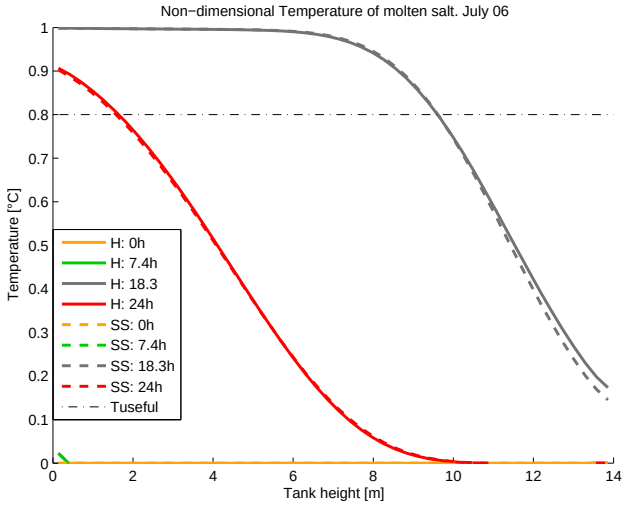

Figure 6-13: Dimensionless temperature distribution of solar salt (SS) and Hitec (H) on July 6th

Solar salt leads to more electricity than Hitec case. As shown, the two tank have almost the same behavior and the same amount of thermal energy is stored and then withdrawn (Table 6-5). However, the CSP plant using solar salt thermal efficiency is 1% (absolute) greater than Hitec one. As a result, CSP plant equipped with solar salt thermocline TES is supposed to be slightly more performing than a CSP equipped with a Hitec thermocline.

Concluding, solar salt TES and Hitec TES have almost the same discharge efficiency. However, solar salt TES is preferred because the storage is assessed to be cheaper and because thermal energy is converted to electricity with higher thermal efficiency.

6.3.3 Molten salt and packed bed thermal conductivity

Thermal conductivity influences thermocline development. Especially, during nighttime it is the responsible of thermocline expansion (subsection 5.3.1). A study on the influence of thermal conductivity of TES filler (packed bed and molten salt) on thermocline development is carried out.

Two simulations are compared in Figure 6-14. Solid lines represent the thermocline at various moments of the day when normal thermal conductivity is taken; dashed lines represent the thermocline development if both molten salt and packed bed thermal conductivities are taken equal to zero, i.e. there is no thermal diffusion in the tank. As expected, a change in thermal conductivity

little affects thermocline development. Indeed, Péclet number is much greater than 1 and thermocline expansion is mainly due to advection and not to diffusion (Table 6-6). Also Xu et al. assessed that thermal conductivity has little influence on thermocline development [12].

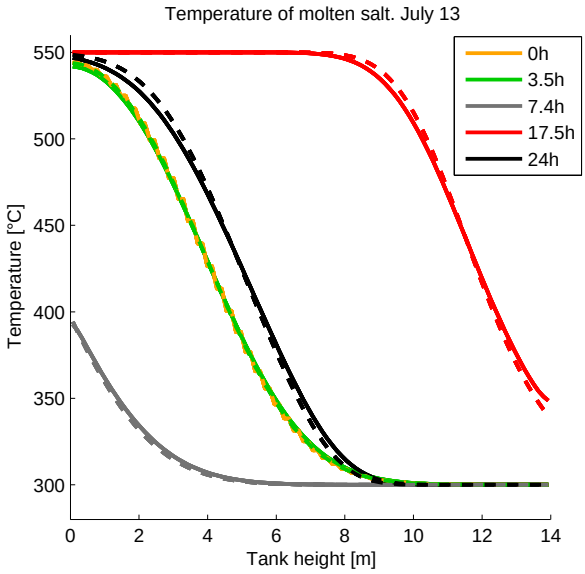

Figure 6-14: Molten salt temperature when thermal conductivity is changed from the normal value (solid lines) to the value of 0 (dashed lines)

To sum up, the expansion of the thermocline is mainly due to advective transport, i.e. the hot molten salt displaced in the cold region of the thermocline, or vice versa. The research of molten salts or packed bed with lower thermal conductivities is pointless: thermal conductivity of employed materials is low enough to prevent the thermocline to excessively expand. Also materials with slightly higher thermal conductivity (within 3-5 times) are expected to little affect thermocline development and hence, discharge efficiency (section 3.4.6) [11].

6.3.4 Tank height

An increase in height of thermocline tank is assessed to be beneficial, as explained in subsection 3.4.4 [1][12][14]. Thermocline extension is assessed to be averagely of 5-7 meters; hence, the relative portion of tank height occupied by the thermocline is in percentage less in tall tanks than in short tanks. Hence, in tall tanks thermal stratification is improved and discharge efficiency is increased.

In Figure 6-15, temperature distribution in three tanks with different heights is compared. The chosen tank is a 7.5h tank using solar salt. The volume is kept at 6150 m^3 (Table 6-4) and the height of the tank is changed: as a

consequence, the diameter changes (tall vessels have smaller diameter). The thermocline of the 25 meters–tall tank looks slightly steeper than the reference case (14 m-tall vessel). Instead, the thermocline of the 5 meters-tall tank is much more extended.

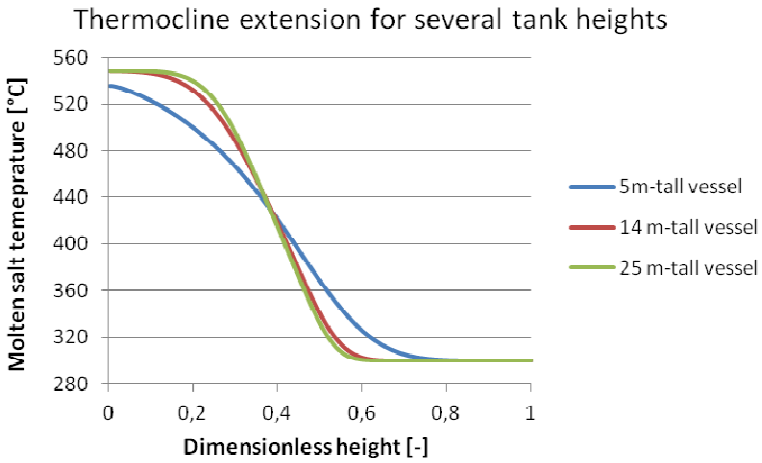

Figure 6-15: Thermocline extension for several tank heights

As tank height is raised, discharge efficiency improves (Figure 6-16). The increase is sharp when height is raised from 5 to 25 meters. For taller tanks, the increase in discharge efficiency is little. When 40 meters are reached, discharge efficiency reaches a maximum value. Further, it starts to drop slightly.

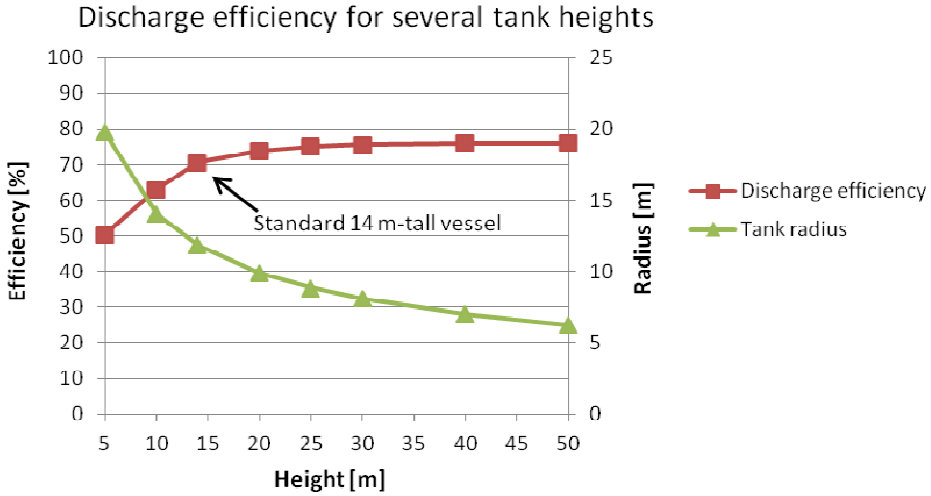

Figure 6-16: Discharge efficiency for several tank heights

Discharge efficiency rises from 50,4% to 75,0% when increasing height from 5 meters to 25 meters. For those vessels, an increase in height is advantageous

because of better thermal stratification. Further increase in height is pointless for two reasons. First, higher tanks have high molten salt velocity, which boosts thermocline expansion due to advection. However, this increased extension of the thermocline (in meters) is almost perfectly balanced by the increase in tank height (in meters). As a result, the ratio of thermocline extension on tank height is almost constant and discharge efficiency remains unchanged [12][15]. Second, in tall thin tanks heat loss increases because of the larger lateral surface exposed to the environment.

Unfortunately, maximum height of molten salt vessels is limited to about 14 meters, because of constructive issues [13][1][12]. However, if a 25 meters tall vessel is desired, it would be possible to build two tanks of 12,5 meters connected in series. This system behaves similarly to a 25 meters tank, except that there are two thermoclines, one in each tank. This arrangement can be very attractive, so further investigations are required.

Also in very tall tanks, where molten salt has higher velocity, fingering is evaluated as not a threat and thermal stratification is not spoiled by this phenomenon. Tall tanks have little diameter, high molten salt velocity and high Reynolds numbers (Table 6-6). A fingering factor of safety is defined in eq. (6.10). As seen, also in high tanks fingering is not likely to occur and factor of safety is always above 1.3 also for 70 m-tall tanks (Table 6-6).

$$factor\ of\ safety = \frac{v_c}{u_m} \tag{6.10}$$

Table 6-6: molten salt velocity, Reynolds number, Péclet number and fingering factor of safety

Tank height [m]	5	14	25	40	70
Tank diameter [m]	39,6	23,7	17,7	14,0	10,6
Reynolds number [-]	17	46	82	130	227
Péclet number [-]	68	191	342	547	957
Molten salt velocity (u_m) [mm/s]	1,54	4,19	7,40	11,78	20,55
Critical fingering velocity (v_c) [mm/s]	27,30	27,30	27,30	27,30	27,30
Factor of safety [-]	**17,7**	**6,5**	**3,7**	**2,3**	**1,3**

To sum up, an increase in tank height from 14 meters to 25 meters would give an increase in the range of 5% of discharge efficiency. This can be technically done putting in series two tanks of 12,5 meters. Tanks taller than 25 meters are pointless because the increase in discharge efficiency is little or negative. Thankfully, fingering does not occur even in very high tanks characterized by higher molten salt velocity. Thus, effective thermal stratification is always guaranteed.

Conclusions

Direct storage in thermocline TES system is believed to be cheaper than indirect state-of-art two-tank TES configuration. TES is responsible of about 15-20% of the investment cost of CSP plants: reduction of this cost is beneficial because larger storage becomes convenient and equivalent working hours of the plant are increased. This decreases the levelised cost of electricity because the cost of the power block and, hence, of the solar plant, is better amortized. Compared to two-tank systems, thermocline TES is cheaper because it requires only one vessel; also, the storage is filled with a low-cost packed bed of quartzite rocks and silica sand, which displace more expensive molten salt. Besides, thanks to direct storage, molten salt temperature is boosted to high values, such as 550 °C when using solar salt. Hence, storage dimension and its cost are further reduced and the power block works with high thermal-to-electric efficiency.

Unfortunately, thermocline TES is less performing than the state-of-art two-tank TES configuration. In thermocline TES, a significant amount of thermal energy is stored in the thermocline region at temperatures between 550°C and 300°C: hence, a share of injected thermal energy at 550 °C is depleted.

To predict temperature distribution in the tank, a two-dimensional finite-difference model is developed and validated with four analytical solutions and experimental data available in literature. The model includes heat transfer between the packed bed and the molten salt, heat loss with the environment as well as axial and radial heat diffusion. This model is used to study thermocline behavior and its performance.

At first, some issues of thermocline TES are studied. For example, thermocline tanks must be well designed to avoid thermal ratcheting. Thermal ratcheting occurs because the temperature of molten salt in the tank swings between high and low temperature. When the tank is heated up, the vessel expands and the packed bed rearranges itself: this prevents the tank to shrink when hot molten salt are withdrawn and, hence, the tank is cooled down. This induces great stresses in the steel envelope of the vessel, which could reach plastic deformation and, eventually, the point of fracture. Temperature distribution in the wall is studied and three walls structures which can stand thermal ratcheting are proposed. Also, insulation properties of these three structures are tested: the most insulated wall is identified as good wall candidate for thermocline TES.

Another example of thermocline problem is the fingering phenomenon. Fingering must be avoided because it might spoil thermal stratification. It is found that fingering might happen only when the thermocline is charged. After

the study of the hydrodynamics of the phenomenon, a critical velocity is found: molten salt velocity must not overtake this critical velocity in order to prevent fingering. It is observed that fingering does not occur in typical thermocline configurations and for typical molten salt mass flow rates.

The 7,5h two-tank systems of a CSP plant is replaced by a thermocline TES to better understand the difference in performance between the two configurations. Molten salt mass flow rate is unchanged: hence, the two systems work in the same conditions. To compare their performance, two performance indicators are defined: discharge efficiency and collection efficiency. Discharge efficiency is the ratio of thermal energy withdrawn at high temperature (>545°C) on total energy withdrawn; collection efficiency is the ratio of stored energy on storable energy. According to those definitions, two-tank systems have both 100% discharge efficiency and 100% collection efficiency. Several simulations are run to understand efficiencies of thermocline TES.

Simulations are run over a typical summer week (9^{th} – 15^{th} July) varying the size of thermocline tanks: it is found that there is a trade-off between collection efficiency and discharge efficiency. More in detail, little tanks show high discharge efficiency, because the thermocline is quite steep. On the other hand, they have little collection efficiency because they are filled quickly and much storable energy is wasted (defocusing). Larger tanks have high collection efficiency of 90-94%. Collection efficiency is always below 100% because some thermal energy is wasted when thermal gradient region reaches the bottom of the tank. On the other hand, large tanks have low discharge efficiency because these vessels are oversized: hence, thermocline is less steep and more energy is depleted in the thermal gradient region. Thermocline vessel sizing 6h of full-load capacity shows the highest quantity of thermal energy withdrawn at very high temperature (>545°C): 6h tank is the vessel which behaves most similarly to the two-tank system. Also 7h and 8h however are good candidates: in those two cases, the amount of energy withdrawn above 545°C is slightly less than in the 6h case.

6h tank suffers of quick change in temperature at the inlet and outlet of the tank: when thermocline reaches the top of the tank (tank almost completely discharged) temperature drops quickly. Evaporative pressure at the power block must be readily decreased and the procedure for turning-off of the plant starts. Also, when the thermocline reaches the bottom of the tank (tank almost fully charged), average temperature of molten salt at the solar field increases and some mirrors are placed in stowed position to avoid superheating of the collectors. This effect is much less severe in 7h and 8h tanks, which are finally preferred. Finally, thermocline sizing 7,5h is identified as the best choice.

To summarize, the optimal thermocline size is found to be 7,5h. During the chosen summer week, thermocline shows a discharge efficiency of 70,6% and a collection efficiency of 90,9%. In this thermocline, stored energy is 5019

MWh_{th} and useful thermal energy is 3518 MWh_{th}. Internal energy variation is negligible (≈ 5 MWh_{th}) and heat loss are as low as 31 $MWh_{th.}$ So, the remaining 1426 MWh_{th} are withdrawn below 545 °C. To compare, in the same period a two-tank system of the same size would have stored 5522 MWh_{th} and would have withdrawn 5450 MWh_{th} of useful energy. Concluding, useful energy withdrawn from the thermocline above the threshold temperature of 545 °C is 30-40% less than in the two-tank case.

Behavior of thermocline is also tested on a typical spring week. In spring the performance of thermocline TES is worsened because the tank is only marginally used and less thermal energy is stored in the tank: the tank behaves as an oversized storage. In these conditions, optimal tank size is still 6h, but 7h and 8h cases are less recommended because discharge efficiency drops. For 7,5h case, collection efficiency is still 90,9% but discharge efficiency is 65,8%.

Actually, the power block of CSP plants is able to work below the nominal temperature. There are Rankine cycles which can work also 90°C below the nominal temperature [2]. Hence, 545°C as threshold temperature is a very conservative assumption. Performance of thermocline TES is much improved when lower threshold temperatures are considered: it is found that discharge efficiency is 95% if 475°C is chosen as threshold temperature. However, in this case no comparison with two-tank systems is possible, because heat is withdrawn at different temperatures, i.e. at different quality.

Furthermore, some tests are performed in order to understand wheater the discharge efficiency can be improved when considering 545°C as threshold temperature. For example, thermoclines using solar salt and Hitec are compared. It is found that solar salt is to be preferred. Hitec and solar salt thermoclines give almost the same discharge efficiency, but solar salt operates at higher temperature. Hence, withdrawn heat is converted to electricity with higher thermal efficiency. Also, a sensitivity study on thermal conductivity is carried out, finding that thermal conductivity slightly affects thermocline development. Hence, the research of molten salts or packed beds with lower thermal conductivity is pointless. Finally, the height of the tank is increased. Indeed, tall tanks show better thermal stratification [14]. It is found that 25-meters tanks give 5% higher discharge efficiency. It is pointless to further push tallness of the vessels above 25-meters because stratification is not much improved and heat loss becomes more significant. As it is not possible to build 25-meter tall tanks, it has been proposed to connect in series two thermocline tanks of 12,5 meters. This new configuration is quite attractive but further studies are required.

Possible future studies on thermocline TES regard the study of the annual performance of the thermocline compared to two-tank configuration. A lighter one-dimensional one-phase thermocline model would be more suitable

for such annual simulations. Indeed, the developed two-dimensional two-phase numerical model is quite “heavy” and annual simulations would take much time. As demonstrated in this work, radial temperature distribution is almost uniform for well insulated tanks. So, the problem can be considered as one-dimensional. Also, for typical molten salt velocity, the temperature difference between the packed bed and the molten salt is small ($< 2°C$) and the mixture behaves as a single homogeneous medium. Hence, one-dimensional one-phase thermocline numerical model are expected to be well accurate: such model is suitable for annual simulation of thermocline TES.

To better compare performance of thermocline TES systems with two-tank TES systems, the electrical output of CSP plants using thermocline TES should be compared with the electrical output of CSP plants equipped with a two-tank system. Two-tank TES systems supplies thermal energy steadily at very high temperature while temperature of thermal energy withdrawn from thermocline TES can widely vary. In these two cases, thermal energy is converted to electricity with different efficiencies depending on the temperature of the withdrawn molten salt. To better compare the two systems, the useful electric output should be compared.

Finally, the levelised cost of each system should be evaluated. A cost comparison in necessary to determine which TES is the most suitable for CSP plants. Two-tank systems are more expensive, but more performing and thermal energy is converted steadily at nominal power block efficiency. Thermocline TES is much cheaper, but a big share withdrawn thermal energy is withdrawn below the nominal temperature and is converted at the power block in off-design conditions. Summing up, thermocline TES remain a very attractive choice as TES in CSP plants, yet further studies must be carried out to determine its cost-effectiveness.

Appendix-A. Discretization of molten salt energy equation

For molten salt energy equation (eq. (A.1)) second order differential terms constrain to integrate along the z-axis and r-axis before applying discretization schemes (2D problem). The integration and discretization passages are long and complex. After the double integration, time is discretized with an implicit downwind-differencing scheme, thermal diffusion with a centered-differencing scheme and advection with an upwind-differencing scheme. This equation is rearranged and several dimensional groups are identified. As a result, a linear system is found (eq. A.14). For molten salt temperature at the node *i* depends on the temperatures of the neighbor nodes, on the temperature of the packed bed and on the molten salt temperature at the previous time step:

$$\varepsilon\rho_{ms}c_{p,ms}\frac{\partial T_{ms}}{\partial t}+\rho_{ms}c_{p,ms}u_m\frac{\partial \mathrm{T_{ms}}}{\partial z}=\frac{\partial}{\partial z}\left(k_{eff}\frac{\partial T_{ms}}{\partial z}\right)+\frac{1}{r}\frac{\partial}{\partial r}\left(k_{eff}r\frac{\partial T_{ms}}{\partial r}\right)+h_v\left(T_{pb}-T_{ms}\right) \tag{A.1}$$

Coefficients are grouped and molten salt energy equation (A.1) is integrated along z-axis; in this case, molten salt is supposed to flow from North (N, the top of the tank) to South (S, the bottom of the tank):

$$\begin{aligned}\int_n^s \varepsilon\rho_{ms}c_{p,ms}\frac{\partial T_{ms}}{\partial t}dz+\int_n^s \rho_{ms}c_{p,ms}u_m\frac{\partial \mathrm{T_{ms}}}{\partial z}dz \\ =\int_n^s\frac{\partial}{\partial z}\left(k_{eff}\frac{\partial T_{ms}}{\partial z}\right)dz+\int_n^s\frac{1}{r}\frac{\partial}{\partial r}\left(k_{eff}r\frac{\partial T_{ms}}{\partial r}\right)dz \\ +\int_n^s h_v\left(T_{par}-T_{ms}\right)dx\end{aligned} \tag{A.2}$$

$$\begin{aligned}\varepsilon\rho_{ms}c_{p,ms}\frac{\partial T_{ms}}{\partial t}\Delta z+\left(\rho_{ms}c_{p,ms}u_m\,\mathrm{T_{ms}}\right)_s-\left(\rho_{ms}c_{p,ms}u_m\,\mathrm{T_{ms}}\right)_n \\ =\left(k_{eff}\frac{\partial T_{ms}}{\partial z}\right)_s-\left(k_{eff}\frac{\partial T_{ms}}{\partial z}\right)_n+\frac{1}{r}\frac{\partial}{\partial r}\left(k_{eff}r\frac{\partial T_{ms}}{\partial r}\right)\Delta z \\ +h_v\left(T_{par}-T_{ms}\right)\Delta z\end{aligned} \tag{A.3}$$

All terms of eq. (A.9) are multiplied by the radius (*r*) and eq. (A.9) is integrated about the radius:

$$\begin{aligned}\int_w^e \varepsilon\rho_{ms}c_{p,ms}\frac{\partial T_{ms}}{\partial t}\Delta z\, r\, dr + \int_w^e \left(\rho_{ms}c_{p,ms}u_m\, \mathrm{T_{ms}}\right)_s r\, dr \\ - \int_w^e \left(\rho_{ms}c_{p,ms}u_m\, \mathrm{T_{ms}}\right)_n r\, dr \\ = \int_w^e \left(k_{eff}\frac{\partial T_{ms}}{\partial z}\right)_s r\, dr - \int_w^e \left(k_{eff}\frac{\partial T_{ms}}{\partial z}\right)_n r\, dr \\ + \int_w^e \frac{\partial}{\partial r}\left(k_{eff}r\frac{\partial T_{ms}}{\partial r}\right) * \Delta z\, dr \\ + \int_w^e h_v\left(T_{par} - T_{ms}\right)\Delta z\, r\, dr\end{aligned} \tag{A.4}$$

Several groups are defined (eq. (A.5)-(A.10)):

$$CS = \frac{r_e^2 - r_w^2}{2} \tag{A.5}$$

$$F_{ms} = \rho_{ms}c_{p,ms}u_m * CS \tag{A.6}$$

$$D_{ms,axial} = \frac{k_{eff}}{\Delta z}CS \tag{A.7}$$

$$D_{ms,radial} = \frac{k_{eff}}{\Delta r}\Delta z * r \tag{A.8}$$

$$V_{ms} = \frac{\varepsilon\rho_{ms}c_{p,ms}\Delta z}{\Delta t}CS \tag{A.9}$$

$$Q = h_v\Delta z\, CS \tag{A.10}$$

After this second integration (eq. (A.4)), discretization approximation takes place. Time is discretized with an implicit downwind scheme, thermal diffusion with a centered scheme and advection with an upwind scheme. The terms defined in eq. (A.5)-(A.10) show out. Result of the two integrations is:

$$\begin{aligned}(V_{ms}^t T_P^t - V_{ms}^{t-1}T_P^{t-1}) + \max\left(F_{ms,s}; -F_{ms,n}\right)\mathrm{T_P^t} - max(F_{ms,n}; 0)\mathrm{T_N^t} \\ - \max\left(F_{ms,s}; 0\right)T_S^t \\ = D_{ms,s}(T_S^t - T_P^t) - D_{ms,n}(T_P^t - T_N^t) + D_{ms,e}(T_E^t - T_P^t) \\ - D_{ms,w}(T_P^t - T_W^t) + h_v\left(T_{par}^t - T_P^t\right)\Delta z\end{aligned} \tag{A.11}$$

Equation (A.11) is rearranged and subscript P, W, E, N and S (Center, West, East, North and South) are replaced by *i*, *i-1*, *i+1*, *i-Nr* and *i+Nr*:

$$\begin{aligned}\left(V_{ms} + \max\left(F_{ms,s}; -F_{ms,n}\right) + D_{ms,s} + D_{ms,n} + h_v \Delta z\right) T^t_{ms,i} \\ - \left(D_{ms,n} + \max\left(F_{ms,n}; 0\right)\right) T^t_{ms,i-1} - (D_{ms,s} \\ + \max\left(F_{ms,s}; 0\right)) T^t_{ms,i+1} = V_{ms}\, T^{t-1}_{ms,i} + h_v \Delta z\, T^t_{par,i}\end{aligned} \tag{A.12}$$

And equation (A.12) becomes:

$$\begin{aligned}a_{i,i}\, T^t_{ms,i} + a_{i,i-1}\, T^t_{ms,i-1} + a_{i,i+1}\, T^t_{ms,i+1} + a_{i,i+Nr} T^t_{ms,i+Nr} \\ + a_{i,i-Nr} T^t_{ms,i-Nr} = c_i\end{aligned} \tag{A.13}$$

Coefficients a_i and c_i are defined in eq. (A.14)-(A.19):

$$a_{i,i} = V_{ms} + \max\left(F_{ms,s}; -F_{ms,n}\right) + D_{ms,s} + D_{ms,n} + h_v \Delta z \tag{A.14}$$

$$a_{i,i-Nr} = -\left(D_{ms,n} + \max\left(F_{ms,n}, 0\right)\right) \tag{A.15}$$

$$a_{i,i+Nr} = -\left(D_{ms,s} + \max\left(F_{ms,s}, 0\right)\right) \tag{A.16}$$

$$a_{i,i-1} = -D_{ms,w} \tag{A.17}$$

$$a_{i,i+1} = -D_{ms,e} \tag{A.18}$$

$$c_i = V_{ms}\, T^{t-1}_{ms,i} + h_v \Delta z\, T^t_{pb,i} \tag{A.19}$$

D are diffuse fluxes, F are advective fluxes and V represents the energy storage in the control volume (eq. (A.5)-(A.10)). Eq. (A.19) recalls a matrix product. Indeed, coefficients *a* can be collected in matrix **A**, and the coefficients *c* in vector **C**. Thus, molten salt temperature can be simply obtained:

$$\boldsymbol{A} * \boldsymbol{T} = \boldsymbol{C} \tag{A.20}$$

The boundaries conditions imposed are:

- $\left.\frac{\partial T}{\partial r}\right|_{r=0} = 0$ at the center of the tank, because of symmetric considerations,
- convection with the environment through the wall at the tank wall,
- imposed velocity at the entrance of the tank,
- adiabatic conditions at the top and the bottom of the tank.

Unfortunately, the particle temperature $T^t_{pb,i}$, which shows out in the coefficient c_i (eq. (A.19)), is not know a priori and the problem cannot be solved straight

forwardly. Besides, temperature dependant coefficients (ρ, c_p, k) should be calculated on temperature T_{ms}, which is the unknown. Thus, an iterative procedure is needed to overcome this problem, as explained in subsection 4.2.3.

Appendix-B. Transient radial diffusion

Only radial transient diffusion of the molten salt is considered. Axial diffusion, axial advection and heat transfer with the packed bed are neglected. This problem is described by partial differential equation eq. (B.1). Boundary conditions are convection with the environment and axisymmetric condition at the center of the tank ($r = 0$):

$$\begin{cases} \rho c_p \dfrac{\partial T_{ms}}{\partial t} = \dfrac{1}{r}\dfrac{\partial}{\partial r}\left(k\, r \dfrac{\partial T_{ms}}{\partial r}\right) \\ T(r, t=0) = T_0 \\ -k \left.\dfrac{\partial T_{ms}}{\partial r}\right|_{r=0,t} = 0 \\ -k \left.\dfrac{\partial T_{ms}}{\partial r}\right|_{r=R,t} = h(T_{ms} - T_{amb}) \end{cases} \tag{B.1}$$

T_{amb} is the external temperature of the environment. The mathematical passages to draw the solution of the partial differential equation are here briefly presented as they are long and complex. It is recommended to consult a book on heat conduction for further details [56]. In brief, the resolution strategy redefining and regrouping the variables:

$$r' = r/R \qquad \vartheta = \frac{T - T_{amb}}{T_0 - T_{amb}} \qquad \alpha = \frac{k}{\rho c_p} \qquad H = \frac{h}{k} \tag{B.2}$$

The problem to be solved becomes:

$$\begin{cases} \dfrac{1}{\alpha}\dfrac{\partial \vartheta_{ms}}{\partial t} = \dfrac{\partial^2 \vartheta_{ms}}{\partial^2 r'} + \dfrac{1}{r'}\dfrac{\partial \vartheta_{ms}}{\partial r'} \\ \vartheta(r', t=0) = 1 \\ \left.\dfrac{\partial \vartheta_{ms}}{\partial r}\right|_{r'=0,t} = 0 \\ \left.\dfrac{\partial \vartheta_{ms}}{\partial r'}\right|_{r'=1,t} + H\,\vartheta_{ms} = 0 \end{cases} \tag{B.3}$$

Using the method of separation of variables the problem is redefined:

$$\vartheta(r', t) = R(r') * T(t) \tag{B.4}$$

$$\begin{cases} \frac{1}{\alpha}\frac{T'}{T} = \frac{R''}{R} + \frac{1}{r'}\frac{R'}{R} \\ T(t=0) = 1 \\ R'_{r'=0} = 0 \\ R'_{r'=1} + H\,R = 0 \end{cases} \tag{B.5}$$

As *T* and *R* are independent, they must be equal to a constant. The problem to solve is:

$$\frac{1}{\alpha}\frac{T'}{T} = \frac{R''}{R} + \frac{1}{r'}\frac{R'}{R} = -\beta^2 \tag{B.6}$$

$$\begin{cases} T' + \alpha\beta^2 \mathrm{T} = 0 & \text{(B.7)} \\ \left(R'' + \frac{1}{r}R'\right) + (\beta^2)\mathrm{R} = 0 & \text{(B.8)} \end{cases}$$

Where β^2 is a constant. The first equation has an exponential trends, while the second one is equal to the definition of the Bessel differential equation of order zero. So, the solution is of the form:

$$\begin{cases} T = C_1 \exp(-\alpha\beta^2\,\mathrm{t}) & \text{(B.9)} \\ R = C_2\,J_0(\beta\,\mathrm{r}) + C_3\,\mathrm{Y}_0(\beta\,\mathrm{r}) & \text{(B.10)} \end{cases}$$

Where J_0 and Y_0 are the Bessel functions of the first kind and order zero. Imposing the boundaries conditions, it is find that C_3 must be equal to zero and it is find that R is not a banal solution only if β is solution of this transcendental equation:

$$\beta_\mathrm{m}\,J_1(\beta_\mathrm{m}\,\mathrm{r}) - H\,J_0(\beta_\mathrm{m}\,\mathrm{r}) = 0 \tag{B.11}$$

Putting together R and T, temperature is:

$$\vartheta = \sum_{m=1}^{\infty} C_m \cdot \exp(-\alpha\beta_\mathrm{m}^2\,\mathrm{t}) * \mathrm{J}_0(\beta_\mathrm{m}\,\mathrm{r}) \tag{B.12}$$

After that, the property of orthogonality of the eigenfunctions $\mathrm{J}_0(\beta_\mathrm{m}\,\mathrm{r})$ is exploited and the non-homogenous boundary condition on time is imposed to find the complete solution. Finally, the solution of the radial transient diffusive problem is:

$$\vartheta(r',t) = \sum_{m=1}^{\infty} \frac{2}{R}\frac{H}{H^2+\beta_\mathrm{m}^2}\exp(-\alpha\beta_\mathrm{m}^2\,\mathrm{t}) \cdot \frac{\mathrm{J}_0(\beta_\mathrm{m}\,\mathrm{r}')}{\mathrm{J}_0(\beta_\mathrm{m}\,\mathrm{R})} \tag{B.13}$$

Appendix-C .Heat transfer between packed bed and molten salt

Heat transfer between molten salt and packed bed can be studied analytically if advection and diffusion are neglected. The equations to be solved are two, one for molten salt temperature and one for packed bed temperature (eq. (C.1)-(C.2)). There are no boundaries conditions, except for initial temperature at $t = 0$.

$$\begin{cases} \varepsilon\rho_{ms}c_{p,ms}\dfrac{\partial T_{ms}}{\partial t} = h_v\left(T_{par} - T_{ms}\right) & \text{(C.1)} \\ (1-\varepsilon)\rho_{par}c_{p,par}\dfrac{\partial T_{pb}}{\partial t} = h_v\left(T_{ms} - T_{par}\right) & \text{(C.2)} \\ T_{ms}(z, t=0) = T_{ms,0} \\ T_{pb}(z, t=0) = T_{pb,0} \end{cases}$$

The Biot number of this problem is little but sometimes above 0.1. Jefferson correction is applied and the problem is treated with the lumped capacitance method [57]. The problem recalls the scholastic problem of certain number of spheres (i.e. particles of the packed bed) immersed in a fluid (i.e., the molten salt) at a different temperature. In this case, the problem is more complex because both solid and fluid temperatures vary with time.

The mathematical passages to draw the solution of this ordinary differential equation system are here briefly presented. First, some dimensionless groups are defined.

$$C_{ms} = \varepsilon\rho_{ms}c_{p,ms} \tag{C.3}$$

$$C_{pb} = (1-\varepsilon)\rho_{par}c_{p,pb} \tag{C.4}$$

$$\lambda = \frac{C_{pb} + C_{ms}}{C_{ms}} \tag{C.5}$$

$$\omega = \frac{C_{pb}T_{pb,0} + C_{ms}T_{ms,0}}{C_{pb} + C_{ms}} \tag{C.6}$$

$$\vartheta_{pb}(t) = \frac{T_{pb}(t) - \omega}{T_{pb,0}} \tag{C.7}$$

Then, equations are summed, integrated on time and rearranged.

$$C_{ms}\frac{\partial T_{ms}}{\partial t} = -C_{pb}\frac{\partial T_{pb}}{\partial t} \tag{C.8}$$

$$\int_0^t C_{ms}\frac{\partial T_{ms}}{\partial t}dt = -\int_0^t C_{pb}\frac{\partial T_{pb}}{\partial t}dt \tag{C.9}$$

$$C_{ms}\big(T_{ms}(t) - T_{ms,0}\big) = -C_{par}(T_{pb}(t) - T_{pb,0}) \tag{C.10}$$

$$T_{ms}(t) = \frac{C_{pb}}{C_{ms}}\Big(T_{pb,0} - T_{pb}(t)\Big) + T_{ms,0} \tag{C.11}$$

This relation between the temperature of the molten salt and of the packed bed at a certain instant *t* is put in eq. (C.2). Now, eq. (C.12) turns out to be an ordinary linear differential equation of the first order, which is easily solved to find packed bed temperature (eq. (C.15)). Temperature of the molten salt is then found using eq. (C.11).

$$C_{pb}\frac{\partial T_{pb}}{\partial t} = -h_v\left(T_{pb}(t) - T_{ms,0} - \frac{C_{pb}}{C_{ms}}\Big(T_{pb,0} - T_{pb}(t)\Big)\right) \tag{C.12}$$

$$C_{pb}\frac{\partial T_{pb}}{\partial t} = -h_v\lambda\big(T_{pb}(t) - \omega\big) \tag{C.13}$$

$$\frac{\partial \vartheta_{pb}}{\partial t} = -\frac{h_v\lambda}{C_{pb}}\,\vartheta_{pb}(t) \tag{C.14}$$

$$\vartheta_{pb}(t) = \vartheta_{pb,0}\cdot\exp\left(-\frac{h_v\lambda}{C_{pb}}t\right) \tag{C.15}$$

Appendix-D. Molten salt physical properties

Molten salt physical properties are listed in Table B-1 [12][14][62][41].

Table B-1: molten salt physical properties. T always expressed in [°C]

Solar salt	
Density [kg/m3]	$2090 - 0{,}636 \cdot T$
Heat capacity [J/kgK]	$1443{,}2 - 0{,}172 \cdot T$
Viscosity $[mPa \cdot s]$	$22{,}714 - 0{,}12\,T + 2{,}281 \cdot 10^{-4}\,T^2 - 1{,}474 \cdot 10^{-7}\,T^3$
Thermal conductivity [W/mK]	$0{,}443 + 1{,}9 \cdot 1^{-4} \cdot T$
Hitec	
Density [kg/m3]	$1938 - 0{,}732 \cdot (T - 200)$
Heat capacity [J/kgK]	$1561{,}7$
Viscosity $[Pa \cdot s]$	$exp(-4{,}343 - 2{,}013 \cdot (log(T) - 5{,}011))$
Thermal conductivity [W/mK]	$-6{,}53 \cdot 10^{-4} \cdot (T - 260) + 0{,}421$
HitecXL	
Density [kg/m3]	$1992 - 0{,}58 \cdot (T - 300)$
Heat capacity [J/kgK]	1447
Viscosity $[Pa \cdot s]$	$exp(-3{,}618 - 1{,}99 \cdot (log(T) - 4{,}982))$
Thermal conductivity [W/mK]	$0{,}519$

Appendix-E . Matlab code: finite-difference thermocline model

The code is organized in a main program plus several functions.

Main program

```
%27 March 2012, Angelini Giovanni
%2D finite-difference model for temperature distribution in thermocline
%thermal energy storage
%author: giovanni@angelini.info, giovanni1.angelini@polimi.it

%% Manual setting of simulation data

clc
clear all
tic

%Data

file='Settimana_09_16_luglio.xlsx'; %origin of molten salt mass flow
and T
file_res='Risultati.xlsx';      %file for data print
celle='C12:K12';               %length of the simulation
giorno=['July 09';'July 10';'July 11';'July 12';'July 13';'July
14';'July 15';'July 16'];

numb=1;                %number of simulations to be performed
sequentially
h_storage_imp=[7.5]*ones(1,numb);
L_imp=[14];
number_of_plot_lines=[1]*ones(1,numb);  %except the first. 10 means 11
t_plot_lines=0;
Tin=[300];
time_step=[25]*ones(1,numb);    %time step length imposto/desiderato

phys=[4]*ones(1,numb);      %1: HITEC var, Garimella
                            %2: HITEC cost, T=390°C rho=1799
                            %3: HITEC cost, T=290°C rho=1872
                            %4: Solar Salt var
                            %6: HITEC XL, var

wall_prop=[1]*ones(1,numb);   %adiabatic=1
                              %Low insulation=5
                              %Medium insulation=6
                              %High insulation=7
Tuseful2=545;                %threshold temperature. above this value,
heat is considered as useful
Thigh_imp=[550]*ones(1,numb);
Diam_p=[0.01905]*ones(1,numb);      %particle average diameter
eps=[0.22]*ones(1,numb);            %porosity
```

```
limite_conv=[1e-3]*ones(1,numb);    %100*residuals
Tout=300;
thermocl_dT_tick=0.98*ones(1,numb);
T_amb=25;                           %external temperature
T_par_av=100;
emissiv=0.5;                    %emissivity of external surface
Tlow=300;

var load_factor;
eta_power_block='0.41+load_factor*0';   %thermal efficieny of the power
block
P_gross_max=50;       %power block gross power [MW]

%Numerical data

T_par_implicito=1;      %0 esplicito, 1 implicito
max_j=1000;         %max number of iteration allowed at each time step
relaxation=1;
dT_limite=50;          %Temperature limite dT delle rocce/molten salt.
dt3
Nz=200;             %axial mesh size
Nr=2;               %radial mesh size
num_sez=5;          %distribution or radial nodes

no_bar=0;               %waiting bar. 0 c'è, 1 non c'è
Pacheco_comparison=1;   %plot of Pacheco's exp. data. 0 c'è, 1 non c'è

dati2=zeros(80,numb);
condizione=0;           %0: tempo fissato,
Tstop=inf;

%% Program starts. Variable definition

num_charging_modes=numb;
Nt=zeros(num_charging_modes,1);
x_useful=[-1]*ones(1,numb);
colore=[[256 165 0]/256; [0 205 0]/256; [0.45 0.45 0.45]; [1 0 0]; [0 0
0];[238 47 167]/255; [0 205 0]/256; [0.3 0.3 0.3]; [0 0 0]; [0 0 1]];
stile_linea=[];
stile_linea=strvcat(stile_linea,strcat('-'));
stile_linea=strvcat(stile_linea,strcat('--'));
stile_linea=strvcat(stile_linea,strcat('-'));
stile_linea=strvcat(stile_linea,strcat('--'));
stile_linea=strvcat(stile_linea,strcat('-'));
stile_linea=strvcat(stile_linea,strcat('-.'));
stile_linea=strvcat(stile_linea,stile_linea);
Tm2=zeros(Nz*Nr,max(number_of_plot_lines)+1,num_charging_modes);
beta2=0;

%reading of initial temperature from .xlsx file
if (Nz==200)&&(Nr==2), T0=[]; T0=xlsread('temp.xlsx','B1:B400'); end;

%% Simulations

for ciclo=1:numb,       %from 1 to #simulation

t_plot_lines=0;
```

```
Tmassima=-inf;
aum_mass_flow=1;
sfasa=0;

h_storage=h_storage_imp(ciclo);
L=L_imp(ciclo);
dz=L/Nz;
Thigh=Thigh_imp(ciclo);
var T_prop;
[frho_h fcp_h fk_h fmu_h fk_ms T_freezing rho_p cp_p
k_p]=physical_property_chioce(phys,ciclo);
[rho_low cp_low k_low
mu_low]=prop_val(Tlow,frho_h,fcp_h,fk_h,fmu_h,1,k_p,eps);
[rho_high cp_high k_high
mu_high]=prop_val(Thigh,frho_h,fcp_h,fk_h,fmu_h,1,k_p,eps);
load_factor=1;
Q_storage=h_storage*P_gross_max/eval(eta_power_block);
V_storage=Q_storage*3.6e9/(eps(1)*rho_high*cp_high+(1-
eps(1))*rho_p*cp_p)/(Thigh-Tlow);
raggio=(V_storage/pi/L)^0.5,
contr=zeros(20,1);
mass_nominal=P_gross_max/eval(eta_power_block)/cp_high/(Thigh-
Tlow)*1e6;

%Setting of non-uniform radial mesh
if (num_sez<=1)||(num_sez>=Nr),
    num_sez=Nr;
    contr(11)=-1;
end,
r=zeros(Nr+1,1);
r(1)=0;
i=1;
for i=2:(Nr-num_sez+1),
    r(i)=(raggio-r(i-1))/num_sez+r(i-1);
end,
for i=(Nr-num_sez+2):(Nr+1)
    r(i)=(raggio-r(Nr-num_sez+1))/(num_sez)+r(i-1);
end,
dati=[];
if (phys(ciclo)==4), dati=xlsread(file,celle); else,
    dati=xlsread(file2,celle); end,

dt=time_step(ciclo);
temp=length(dati(:,6))*3600;

Nt=round(length(dati(:,6))*3600/dt);
dtm(ciclo)=dt;
Ntm(ciclo)=Nt;

%variables are set defined and to zero
[Ein Eout Eout_useful Elosses mass_in mass_in2 mass_out dmass_sto
dmass_sto2 Esto0 dEsto mass_sto0 err1_m err1_en err2_en
discharge_efficiency,tempo_esecuzione tot_iterazioni ttx dtm Ntm terr
vc1 um1 ciclo1 i
c1]=azzeramento_var(num_charging_modes,number_of_plot_lines,ones(1,numb
),ones(1,numb),ones(1,numb),time_step,colore,phys);
if i==4, contr(4)=1; end;
if c1==-3, contr(13)=-1; end;
```

```
Tmassima=-inf;
Tminima=inf;
Q_coll=zeros(Nt,1);
Q_stored=zeros(Nt,1);
Q_withdrawn=zeros(Nt,1);
Q_losses=zeros(Nt,1);
Q_defocus=zeros(Nt,1);
Q_withdrawn_useful=zeros(Nt,1);
P_gross=zeros(Nt,1);
mass_flow=zeros(Nt,1);
mass_withdrawn=zeros(Nt,1);
mass_to_power=zeros(Nt,1);
mass_extra=zeros(Nt,1);
mass_sun=zeros(Nt,1);
Q_gas_dir=0;

%molten salt mass flow rate and temperature are read from the
defined .xlsx file (Settimana_09_15_luglio.xlsx for example)
M=3600/dt;
if mod(M,2)==1, disp(strcat('ERROR!! 1800/dt dev''essere intero.
1800/dt: ',num2str(1800/dt))); disp(' '); end;
for i=1:M/2,
    mass_flow(i)=dati(1,5);
    mass_withdrawn(i)=dati(1,7);
    Tsol(i)=dati(1,6);
    if (Tsol(i)==0), Tsol(i)=Thigh; end,
    mass_to_power=dati(1,7);
    mass_sun(i)=dati(1,5);
    Q_coll(i)=mass_sun(i)*cp_high*(Tsol(i)-Tlow)*1e-6;
end,
c1=1;
for i=M/2+1:length(dati(:,6))*M-M/2,
    if i>c1*M+M/2, c1=c1+1; end;
    app=((mod(i-M/2-1,M)+1)*2-1)/(2*M);
    mass_flow(i)=(dati(c1,5)*(1-app)+dati(c1+1,5)*(app));
    mass_withdrawn(i)=(dati(c1,7)*(1-app)+dati(c1+1,7)*(app));
    mass_sun(i)=(dati(c1,5)*(1-app)+dati(c1+1,5)*(app));
    mass_to_power(i)=(dati(c1,7)*(1-app)+dati(c1+1,7)*(app));
    Tsol(i)=dati(c1+1,6);
    if (Tsol(i)==0), Tsol(i)=Thigh; end;
    Q_coll(i)=mass_sun(i)*cp_high*(Tsol(i)-Tlow)*1e-6;
end,
for i=length(dati(:,6))*M-M/2+1:length(dati(:,6))*M,
    mass_flow(i)=dati(length(dati(:,6)),5);
    mass_withdrawn(i)=dati(length(dati(:,6)),7);
    mass_sun(i)=dati(length(dati(:,6)),5);
    mass_to_power(i)=dati(length(dati(:,6)),7);
    Tsol(i)=dati(length(dati(:,6)),6);
    if (Tsol(i)==0), Tsol(i)=Thigh; end;
    Q_coll(i)=mass_sun(i)*cp_high*(Tsol(i)-Tlow)*1e-6;
end,

mass_withdrawn=-mass_withdrawn;
for i=1:length(mass_flow),
    if (mass_flow(i)*mass_withdrawn(i)~=0),
        if mass_flow(i)+mass_withdrawn(i)>0,
            mass_flow(i)=mass_flow(i)+mass_withdrawn(i);
            mass_withdrawn(i)=0;
```

```
        else,
            mass_withdrawn(i)=mass_withdrawn(i)+mass_flow(i);
            mass_flow(i)=0;
        end,
    end,
end,

mass_flow=mass_flow/(pi*raggio^2);
mass_withdrawn=mass_withdrawn/(pi*raggio^2);
mass_to_power=mass_to_power/(pi*raggio^2);
mass_sun=mass_sun/(pi*raggio^2);
Ein_rec=zeros(Nt,1);
Eout_rec=zeros(Nt,1);
Eloss_rec=zeros(Nt,1);

for i=1:length(dati(:,3)),
    if (dati(i,5)>0)||(dati(i,7)<0), Q_gas_dir=Q_gas_dir+dati(i,3);
    end,
end,

%Wall properties definition. Wall_properties function

[num_layer spessore conduttivita v_vento
adiabatic]=wall_properties(wall_prop,ciclo);
[alfa percentuale
type_conv]=calcolo_alfa2(adiabatic,raggio,spessore,T_amb,v_vento,num_la
yer,conduttivita,T_par_av,emissiv,L);
[frho_h fcp_h fk_h fmu_h fk_ms T_freezing rho_p cp_p
k_p]=physical_property_chioce(phys,ciclo);
t_inizio(ciclo)=toc;
T_valutazione_proprieta=(Tin+Tout)/2;
Tuseful=(Thigh-Tlow)*x_useful(ciclo)+Tlow;
Trif=Tlow;                    %temperature reference for energy yields
[rho cp k
mu]=prop_val(T_valutazione_proprieta,frho_h,fcp_h,fk_h,fmu_h,ciclo,k_p,
eps);
T_prop=Tlow;
rho=eval(frho_h);
um=mass_flow(ciclo)/(eps(ciclo)*rho);

%fingering check
[rho1 inutile1 inutile2
mu1]=prop_val(Thigh,frho_h,fcp_h,fk_h,fmu_h,ciclo,k_p,eps);
[rho2 inutile1 inutile2
mu2]=prop_val(Tlow,frho_h,fcp_h,fk_h,fmu_h,ciclo,k_p,eps);
K1=Diam_p(:).^2.*eps(:).^3./(175*(1-eps(:)).^2);
K=min(K1);
vc=9.81*K*(rho1-rho2)/(mu1-mu2);
if um>vc,
    contr(14)=-1;
    vc1=vc;
    um1=um;
    ciclo1=ciclo;
end,

%preliminar evaluation of external convection

mu_av=mean(mu);
```

```
rho_av=mean(rho);
k_av=mean(eval(fk_ms));
cp_av=mean(cp);
Re_D=rho_av*abs(um)*Diam_p(ciclo)/mu_av;
Pr=cp_av*mu_av/k_av;
h=(2+1.1*Pr^(1/3)*Re_D^0.6)*k_av/Diam_p(ciclo);
Biot=h*Diam_p(ciclo)/(3*k_p);
h=h/(1+Biot/5);       %Jefferson correction
hv=6*h*(1-eps(ciclo))/Diam_p(ciclo);

%other variables are defined
T=T0;           %imposizione T iniziale: T0 è letta da un file .xlsx
T_par=T;
T_app=T;
T_par_app=T_par;
T_old=T;
T_par_old=T_par;
Tm=zeros(Nz*Nr,number_of_plot_lines(ciclo)+1);
Tm_par=zeros(Nz*Nr,number_of_plot_lines(ciclo)+1);
Z=linspace(dz/2,L-dz/2,Nz);
Z2=linspace(L-dz/2,dz/2,Nz);
R=zeros(Nr,1);
for i=1:Nr,
    R(i)=(r(i+1)+r(i))/2;
end,
barra=zeros(Nt,1);
perc=zeros(7,1);
t_tot=zeros(7,1);
u_old=zeros(Nr*(Nz+1),1);
u=zeros(Nr*(Nz+1),1);
us=zeros(Nt,1);
Tm(:,1)=T;
Tm_par(:,1)=T_par;
Tm_counter=2;
tot_iteration=0;

if no_bar==0, barra_attesa=waitbar(0,'Solving..'); end,

%Energy initially stored in the tank
[rho cp k mu]=prop_val(Tm(:,1),frho_h,fcp_h,fk_h,fmu_h,ciclo,k_p,eps);
[rho_rif cp_rif inutile1
inutile2]=prop_val(Trif,frho_h,fcp_h,fk_h,fmu_h,ciclo,k_p,eps);

for i=1:Nr*Nz,
    col=mod(i,Nr);
    if col==0, col=Nr; end;
    Esto0(ciclo)=Esto0(ciclo)+(eps(ciclo)*(rho(i)*cp(i)*(Tm(i,1)-
Trif))+(1-eps(ciclo))*rho_p*cp_p*(Tm_par(i,1)-Trif))*(r(col+1)^2-
r(col)^2)/2*dz;
    mass_sto0(ciclo)=mass_sto0(ciclo)+eps(ciclo)*rho(i)*(r(col+1)^2-
r(col)^2)/2*dz;
end,
t=0;
c_mode_old=1;

%% Simualtion begins

    while (t<Nt)&&(max(contr(:))<=0),
```

```
        t=t+1;

         %waiting bar

        if mass_flow(t)>0, strg='Charge'; c_mode=2; end;
        if mass_withdrawn(t)<0, strg='Discharge'; c_mode=3; end;
        if ((mass_flow(t))==0)&&(mass_withdrawn(t)==0), strg='Standby';
c_mode=1; end;
        if (t/Nt>0.05)&&(t>1),
            car=strcat(num2str(round(t/Nt*100)),'%,
',num2str(round((toc-t_inizio(ciclo))*(Nt/(t)-0.5*exp(-t/Nt*15)-1*exp(-
t/Nt*50)-1))),'s, j=',num2str(j),',
T=[',num2str(round(Tout_av)),',',num2str(round(Tin_av)),'],
Mode=',strg,', Ciclo: ',num2str(ciclo),'/',num2str(numb));
        else,
            car=strcat('Solving: ',num2str(round(t/Nt*100)),'%,
T=[',num2str(round(min(T(:)))),',',num2str(round(max(T(:)))),'],
Mode=',strg);
        end,
        if condizione==1,
            car=strcat('Solving. Tout=',num2str(round(T((Nz-
1)*Nr+1)*10)/10));
        end,
        barra(t)=round(toc*(Nt/(t)-0.5*exp(-t/Nt*15)-1*exp(-t/Nt*50)-
1));
        if no_bar==0, waitbar(t/Nt,barra_attesa,car); end,

         %managing of molten salt velocity at thermocline port

        Tin_av=mean(T(1:Nr).*((r(2:Nr+1).^2-r(1:Nr).^2)/(raggio^2/2)));
        Tout_av=mean(T(Nr*(Nz-1)+1:Nr*Nz).*((r(2:Nr+1).^2-
r(1:Nr).^2)/(raggio^2/2)));
        Qsto0=mass_flow(t)*cp_high*(Thigh-Tlow)*pi*raggio^2*1e-6;
        T_rec_out(t)=Tout_av;
        T_rec_in(t)=Tin_av;

        if mass_flow(t)>0,
            um(t)=mass_flow(t)/(eps(1)*rho_high);       %injection
            Tin=Tsol(t);
            Tout=Tlow;
        else
            app=mean(rho(1:Nr).*((r(2:Nr+1).^2-
r(1:Nr).^2)/(raggio^2/2)));
            um(t)=mass_withdrawn(t)/(eps(1)*app);       %withdrawn
            mass_extra(t)=0;
            Tin=Tlow;
            Tout=Tin_av;
        end;

        if (um(t)<0)&&(Tin_av<Tuseful),      %No more Tuseful! empty
tank
            um(t)=0;
            mass_withdrawn(t)=0;
            c_mode=1;
        end,

        if um>vc,                                %fingering check
            contr(14)=-1;
```

```
            vc1=vc;
            um1=um;
            ciclo1=1;
        end,

        T_rec_in(t)=Tin_av;
        T_par_app(:)=T_par_old(:);
        conv=inf;
        j=1;

         %iterative calculation of molten salt temperature,
         %packed bed temperature and molten salt velocity begins

        while (conv>limite_conv(ciclo))&&(max(contr(:))<=0),

            tot_iteration=tot_iteration+1;

            Re_D=zeros(Nr*Nz,1);
            Pr=zeros(Nr*Nz,1);
            h=zeros(Nr*Nz,1);
            hv=zeros(Nr*Nz,1);

             %Evaluation of convetive/radiative heat loss
            [alfa percentuale
type_conv]=calcolo_alfa2(adiabatic,raggio,spessore,T_amb,v_vento,num_la
yer,conduttivita,T_par_av,emissiv,L);
            [rho cp k
mu]=prop_val(T,frho_h,fcp_h,fk_h,fmu_h,ciclo,k_p,eps);
            [rho_old cp_old inutile1
inutile2]=prop_val(T_old,frho_h,fcp_h,fk_h,fmu_h,ciclo,k_p,eps);
            [rhoin cpin inutile1
inutile2]=prop_val(Tin,frho_h,fcp_h,fk_h,fmu_h,ciclo,k_p,eps);
            mu_av=mean(mu);
            rho_av=mean(rho);
            k_av=mean(eval(fk_ms));
            cp_av=mean(cp);
            Re_D=rho_av*abs(um(t))*Diam_p(ciclo)/mu_av;
            Pr=cp_av*mu_av/k_av;
            h=(2+1.1*Pr^(1/3)*Re_D^0.6)*k_av/Diam_p(ciclo);
            Biot=h*Diam_p(ciclo)/(3*k_p);
            h=h/(1+Biot/5);       %Jefferson correction
            hv=6*h*(1-eps(ciclo))/Diam_p(ciclo)*ones(Nr*Nz,1);

             %molten salt velociy evaluation

            if (mass_withdrawn(t)<0),

u=risoluzione_u2(u,um(t),rho_low,rho,rho_old,dz,dt,Nz,Nr,eps,ciclo);
            else,

u=risoluzione_u(u,um(t),rho_high,rho,rho_old,dz,dt,Nz,Nr,eps,ciclo);
            end,
            u_old=u;

             %molten salt temperature evaluation
```

```
T=risoluzione_T(T,T_par_app,T_old,Nr,Nz,k,cp,cp_old,hv,rho,rho_old,dz,d
t,eps,r,R,alfa,u,um(t),Tin,frho_h,fcp_h,T_amb,ciclo,rhoin,cpin);

             %packed bed temperature evaluation

             for c1=1:Nr*Nz,
                if T_par_implicito==0,
                    T_par(c1)=(hv(c1)*dt*(T(c1)-
T_par_app(c1)))/(rho_p*cp_p*(1-eps(ciclo)))+T_par_old(c1);
                else,
                    T_par(c1)=((hv(c1)*dt)*T(c1)+rho_p*cp_p*(1-
eps(ciclo))*T_par_old(c1))/(hv(c1)*dt+rho_p*cp_p*(1-eps(ciclo)));
                end,
             end,

             %residuals estimation
            conv=max(max(abs(T(:)-T_app(:)),abs(T_par(:)-
T_par_app(:))));
            [j, conv];
            j=j+1;

             %preparation for next iteration
            T_app(:)=T_app(:)+(T(:)-T_app(:))*relaxation;
            T_par_app(:)=T_par_app(:)+(T_par(:)-
T_par_app(:))*relaxation;

            if (j>=max_j),
                contr(2)=1;
                terr=t*dt;
            end;

        end,

         %iterations ended. energy and mass fluexs of the time
step are
         %recorded
        if (Tmassima<Tout_av), Tmassima=Tout_av; end;

        T_old=T;
        T_par_old=T_par;

        [Ein Eout Elosses dEsto mass_in mass_out
dmass_sto]=calcoli_energetici4(Tin,rho_old,T_par,Tuseful,um(t),u,rho,cp
,T,ciclo,frho_h,fcp_h,Ein,Eout,Eout_useful,Esto0,Elosses,alfa,mass_flow
(t),raggio,T_amb,mass_sto0,mass_out,dmass_sto2,rho_rif,cp_rif,Trif,cp_p
,rho_p,mass_in,mass_in2,dt,dz,r,R,eps,Nr,Nz);

        if um(t)>0, Ein_rec(t)=Ein; else Ein_rec(t)=Eout; end;
        if um(t)>0, Eout_rec(t)=Eout; else Eout_rec(t)=Ein; end;
        Eloss_rec(t)=Elosses(ciclo)-sum(Eloss_rec(1:(t-1)));
        Tin_av=mean(T(1:Nr).*((r(2:Nr+1).^2-r(1:Nr).^2)/(raggio^2/2)));
        Tout_av=mean(T(Nr*(Nz-1)+1:Nr*Nz).*((r(2:Nr+1).^2-
r(1:Nr).^2)/(raggio^2/2)));
        Q_losses(t)=Elosses(ciclo)*1e-6*2*pi/dt-sum(Q_losses(1:(t-1)));
        Q_stored(t)=(mass_flow(t)>0)*(Ein_rec(t)-Eout_rec(t))*2*pi*1e-
6/dt;
```

```
        Q_defocus(t)=(mass_flow(t)>0)*(Qsto0-Q_stored(t));
        Q_withdrawn(t)=(mass_withdrawn(t)<0)*(-
Ein_rec(t)+Eout_rec(t))*2*pi*1e-6/dt;

        Tm6=zeros(Nz,1);
        app=0;
        app2=1e-9;
        for c1=1:Nz,
            Tm6(c1)=mean(T((c1-1)*Nr+1:(c1*Nr)).*((r(2:Nr+1).^2-
r(1:Nr).^2)/(raggio^2/2)));
            if (Tm6(c1)>Tuseful2), app=app+Tm6(c1)-Tlow; else
app2=app2+Tm6(c1)-Tlow; end;
        end,
        Q_stored_useful(t)=app/(app+app2);

        if (Tin_av>Tuseful2)&&(mass_withdrawn(t)<0),
Q_withdrawn_useful(t)=(mass_withdrawn(t)<0)*(-
Ein_rec(t)+Eout_rec(t))*2*pi*1e-6/dt; end;

        if mass_withdrawn(t)<0,
            Tpb=((mass_to_power(t)+mass_withdrawn(t)).*Tsol(t)-
mass_withdrawn(t).*Tin_av)./mass_to_power(t);
        else,
            Tpb=Tsol(t);
        end,
        mass_to_power(t)=mass_sun(t)-mass_flow(t)-mass_withdrawn(t);
        load_factor=P_gross(t)/P_gross_max;
        eta_power_block_eff(t)=eval(eta_power_block);
        P_gross(t)=(Q_coll(t)-Q_stored(t)-Q_defocus(t)-
Q_withdrawn(t))*eta_power_block_eff(t);

         %molten salt freezing check
        a1=zeros(Nz,1);
        for i=1:Nz,
            a1(i)=(T(Nr*i)-T(Nr*i-1))/(R(Nr)-R(Nr-1))*(raggio-
R(Nr))+T(Nr*i);
        end,
        T_par_av=mean(a1(:));
        if (min(a1)<T_freezing)&&(max(contr)<=0),
            contr(1)=1;
            terr=t*dt;
        end,

        if (T((Nz-1)*Nr+1)<Tstop)&&(condizione==1),
            contr(3)=1;
            terr=t*dt;
        end,

         %recording of molten salt temperature if the thermocline
         %changes of mode (for example, from standby to charge)

        if mass_flow(t)>0, strg='Charge'; c_mode=2; end;
        if mass_withdrawn(t)<0, strg='Discharge'; c_mode=3; end;
        if ((mass_flow(t))==0)&&(mass_withdrawn(t)==0), strg='Standby';
c_mode=1; end;

        if (c_mode~=c_mode_old)||(mod(t*dt,(3600*24))==0)||(t==Nt),
%al cambio mode o ogni 24h
```

```
            c_mode_old=c_mode;
            t_plot_lines(Tm_counter)=t*dt;

            %memorizzio Tm e Tm_par
            Tm(:,Tm_counter)=T(:)';
            Tm_par(:,Tm_counter)=T_par(:)';
            Tm_counter=Tm_counter+1;
        end,

    end,

%end of the simulation. Data are recorded in dati2 and figures
are produced

if Tm_counter==2, contr(15)=-1; end;
disp_warnings_and_errors2(contr,terr,ciclo1,um1,vc1);

Tm2(:,1:number_of_plot_lines(ciclo)+1,ciclo)=Tm(:,1:number_of_plot_line
s(ciclo)+1);

%Figures

if no_bar==0, close(barra_attesa); end,

Tm5=zeros(Nz,length(t_plot_lines));
for i=1:length(t_plot_lines),
    for c1=1:Nz,
        Tm5(c1,i)=mean(Tm((c1-1)*Nr+1:(c1*Nr),i).*((r(2:Nr+1).^2-
r(1:Nr).^2)/(raggio^2/2)));
    end,
end,

beta=0;
c2=2;
id_col=0;
for c1=2:length(t_plot_lines),
    if (t_plot_lines(c1)/(3600*24))>beta,
        beta=beta+1;
        beta2=beta2+1;
        id_col=1;
        figure(beta2);
            subplot(1,2,2);

    hold on
    app=(1+(beta-1)*24*3600/dt:beta*24*3600/dt);
    app3=(1+(beta-1)*24*3600/dt:temp/dt);
    if (temp<beta*24*2600), app=app3; end;
    app2=app*dt/3600;

plot(app2,Q_coll(app),'Color',colore(1,:),'Linewidth',2,'Linestyle',sti
le_linea(1,:));

plot(app2,Q_stored(app),'Color',colore(2,:),'Linewidth',2,'Linestyle',s
tile_linea(2,:));
    plot(app2,-
Q_withdrawn(app),'Color',colore(4,:),'Linewidth',2,'Linestyle',stile_li
nea(4,:));
```

```
plot(app2,Q_losses(app),'Color',colore(5,:),'Linewidth',2,'Linestyle',s
tile_linea(5,:));

plot(app2,P_gross(app),'Color',colore(3,:),'Linewidth',2,'Linestyle',st
ile_linea(3,:));
    %
plot(app,Q_defocus,'Color',colore(6,:),'Linewidth',2,'Linestyle',stile_
linea(6,:));

    legend('Q collected','Q stored','Q withdrawn','Q loss','P gross');
    xlabel('Simulation time [h]');
    ylabel('Thermal/Electric Power [MW]');
    title(strcat('Energy yield.',giorno(beta,:)));
    set(gca,'XTick',0:3:24*beta);
    if beta==1,    set(gca,'Xticklabel',([(0:3:24)]));
    else set(gca,'Xticklabel',([(0:3:(24*(beta-1))-3),(0:3:24)])); end;
    axis([24*(beta-1) 24*(beta) 0 ceil(max([max(Q_stored/20),max(-
Q_withdrawn/20),max(Q_coll/20),max(Q_losses/20),max(P_gross/20)]))*20])
;

        subplot(1,2,1);
        hold on
        c3=c2;
        while
(c3<length(t_plot_lines))&&((t_plot_lines(c3)/(3600*24))<=beta),
            c3=c3+1;
        end,
        p=[];
        for i=c2-1:c3-2,

p=strvcat(p,strcat(num2str(mod(round((t_plot_lines(i))/360)/10,24)),'h'
));
        end,
        if (mod(round((t_plot_lines(c3-1))/360)/10,24))==0,
p=strvcat(p,strcat('24h'));
%             p=strvcat(p,'Tuseful');
%             H=line([0 L],[Tuseful Tuseful]);
%             set(H,'Color','k','Linestyle','-.');
        else,
            p=strvcat(p,strcat(num2str(mod(round((t_plot_lines(c3-
1))/360)/10,24)),'h'));
            p=strvcat(p,strcat('24h'));
%             p=strvcat(p,'Tuseful');
        end;
        c2=c3;
        plot(Z,Tm5(:,c1-
1)','Color',colore(id_col,:),'LineWidth',2,'LineStyle',stile_linea(id_c
ol,:));
        id_col=id_col+1;
        legend(p);
    end,

plot(Z,Tm5(:,c1)','Color',colore(id_col,:),'LineWidth',2,'LineStyle',st
ile_linea(id_col,:));
    id_col=id_col+1;
        if
(c1==length(t_plot_lines))||(t_plot_lines(c1+1)/(3600*24))>beta,
```

```
            H=line([0 L],[Tuseful Tuseful]);
            set(H,'Color','k','Linestyle','-.');
        end,
    legend(p);

    xlabel('Tank height [m]');
    ylabel('Temperature [°C]');
    title(strcat('Temperature of molten salt. ',giorno(beta,:)));
    axis([0,L,min(Tminima-10,min(Tout-10,Tlow-
10)),max(max(Tin(:))+10,max(Tout+10,Thigh+10))]);
end,

tot_iterazioni(1)=tot_iteration;
discharge_efficiency=sum(-Q_withdrawn)/(sum(Q_stored));

%Record of useful data and results

dati2(1,ciclo)=sum(Q_coll)*dt/3600;              %Q collected [MWhth]
dati2(2,ciclo)=sum(Q_stored)*dt/3600;                   %Q stored
dati2(3,ciclo)=sum(-Q_withdrawn)*dt/3600;               %Q withdrawn
dati2(4,ciclo)=sum(Q_losses)*dt/3600;                       %Q loss
dati2(5,ciclo)=sum(Q_defocus)*dt/3600;                      %Q defocus
dati2(6,ciclo)=sum(Q_stored-Q_losses+Q_withdrawn)*dt/3600;  %dU
dati2(7,ciclo)=sum(Q_coll-Q_stored-Q_defocus-Q_withdrawn)*dt/3600; %Q
to the power block
dati2(8,ciclo)=sum(P_gross)*dt/3600;        %P gross
dati2(9,ciclo)=Q_gas_dir;                   %Q gas
dati2(10,ciclo)=sum(dati(:,3))-Q_gas_dir;   %Qgas for freezing
protection
dati2(11,ciclo)=sum(P_gross)/sum(Q_coll)*100;  %sun-to-electric effic
dati2(12,ciclo)=sum(P_gross)/sum(Q_coll-Q_stored-Q_defocus-
Q_withdrawn)*100;
dati2(13,ciclo)=discharge_efficiency(1)*100;     %Qwith/Qstored
dati2(14,ciclo)=0;
dati2(15,ciclo)=0;
dati2(16,ciclo)=wall_prop(ciclo);           %wall type (1-7) [-]
dati2(17,ciclo)=sum(Q_withdrawn_useful)/sum(Q_withdrawn)*100;
%discharge efficiency
dati2(18,ciclo)=sum(-Q_withdrawn_useful)*dt/3600;       %Q useful
dati2(19,ciclo)=phys(ciclo);    %molten salt physical prop (1-8) [-]
dati2(20,ciclo)=dt;                         %time step length
dati2(21,ciclo)=Nz;                         %mesh dimension
dati2(22,ciclo)=raggio;                     %tank radius [m]
dati2(23,ciclo)=h_storage;                  %tank size (in hours)
dati2(24,ciclo)=V_storage;                  %tank volume [m3]
dati2(25,ciclo)=Q_storage;                  %tank storage capactiy
[MWhth]
dati2(26,ciclo)=max(T_rec_out);

%record of heat withdrawn at different temperatures
for i=1:Nt*dt/24/3600, dati2(26+i,ciclo)=sum(Q_withdrawn(1+(i-
1)*24*3600/dt:i*24*3600/dt));end;
for i=1:Nt*dt/24/3600,
dati2(26+i+Nt*dt/24/3600,ciclo)=sum(Q_stored(1+(i-
1)*24*3600/dt:i*24*3600/dt));end;
for i=1:Nt*dt/24/3600,
dati2(26+i+2*Nt*dt/24/3600,ciclo)=sum(Q_losses(1+(i-
1)*24*3600/dt:i*24*3600/dt));end;
```

```
end,

%end of all simulations. Figures are produced and dati2 are
saved in Results.xlsx

figure(9),
hold on
app=(dt/2:dt:(temp-dt/2))/3600;
plot(app,Q_coll,'Color',colore(1,:),'Linewidth',2);
plot(app,Q_stored,'Color',colore(2,:),'Linewidth',2);
plot(app,-Q_withdrawn,'Color',colore(4,:),'Linewidth',2);
plot(app,Q_losses,'Color',colore(5,:),'Linewidth',2);
plot(app,P_gross,'Color',colore(3,:),'Linewidth',2);
legend('Q collected','Q stored','Q withdrawn','Q loss','P gross');
xlabel('Simulation time [day]');
ylabel('Thermal/Electric Power [MW]');
title('Energy yield around the Thermocline TES');
set(gca,'XTick',0:24:temp/3600);
set(gca,'Xticklabel',giorno);
axis([0 temp/3600 0 ceil(max([max(Q_stored/20),max(-
Q_withdrawn/20),max(Q_coll/20),max(Q_losses/20),max(P_gross/20)]))*20])
;

figure(14);
hold on
app=(dt/2:dt:(temp-dt/2))/3600;
plot(app,mass_sun*pi*raggio^2,'Color',colore(1,:),'Linewidth',2,'Linest
yle',stile_linea(1,:));%,'Marker','d');
plot(app,mass_to_power*pi*raggio^2,'Color',colore(4,:),'Linewidth',2,'L
inestyle',stile_linea(3,:));%,'Marker','d');
plot(app,mass_flow*pi*raggio^2,'Color',colore(2,:),'Linewidth',2,'Lines
tyle',stile_linea(2,:));%,'Marker','p');
plot(app,-
mass_withdrawn*pi*raggio^2,'Color',colore(3,:),'Linewidth',2,'Linestyle
',stile_linea(4,:));%,'Marker','v');

axis([0 temp/3600 -0.01
ceil(max([max(mass_sun*pi*raggio^2),max(mass_to_power*pi*raggio^2),max(
mass_flow*pi*raggio^2),max(-mass_withdrawn*pi*raggio^2),1]*2))/2]);
set(gca,'XTick',0:24:temp/3600);
set(gca,'Xticklabel',giorno);
legend('mass solar field','mass to PB','mass to storage','mass
withdrawn');
xlabel('Simulation time [day]');
ylabel('Thermal storage mass flow [kg/s]');
title('Mass injected and withdrawn to/from the Thermocline TES');

figure(15);
hold on
app=[];
app2=[];
for i=1:t, app(i)=T_rec_out(i); end;
for i=1:t, app2(i)=T_rec_in(i); end;
plot((1:t)*dt/3600/24,app,'Linewidth',2,'Color','b');
plot((1:t)*dt/3600/24,app2,'Linewidth',2,'Color','r');
plot((1:t)*dt/3600/24,mass_flow*10+300,'Color',colore(2,:),'Linewidth',
2,'Linestyle',stile_linea(2,:));
```

```
plot((1:t)*dt/3600/24,-
mass_withdrawn*10+300,'Color',colore(4,:),'Linewidth',2,'Linestyle',sti
le_linea(4,:));
title('Temperature at the bottom and top of the thermocline');
xlabel('Simulation time [day]');
ylabel('Molten Salt Temperature at the boundaries of the thermocline
[°C]');
axis([dt/3600/24 t*dt/3600/24 290 560]);
legend('T at the bottom','T at the top','Charge','Discharge','T at the
bottom, 7.7h','T at the top, 7.7h');

xlswrite(file_res,dati2,'Foglio1',strcat('B4:',char(65+numb),'85'));

toc
```

Energetic balance

```
function [Ein Eout Elosses dEsto mass_in mass_out
dmass_sto]=calcoli_energetici4(Tin,rho_old,T_par,Tuseful,um,u,rho,cp,T,
ciclo,frho_h,fcp_h,Ein,Eout,Eout_useful,Esto0,Elosses,alfa,mass_flow,ra
ggio,T_amb,mass_sto0,mass_out,dmass_sto2,rho_rif,cp_rif,Trif,cp_p,rho_p
,mass_in,mass_in2,dt,dz,r,R,eps,Nr,Nz)

Ein=0;
Eout=0;
ciclo=1;
for i=1:Nr,
    if um==0,
        rhoin=rho(i);
        cpin=cp(i);
        Tingresso=T(i);
        u_in=0;
    else
        Tingresso=Tin(ciclo);
        T_prop=Tin(ciclo);
        rhoin=eval(frho_h);
        cpin=eval(fcp_h);
        if (um>0), u_in=um;
        else u_in=u(Nr*(Nz+1)); end;
    end,

Ein(ciclo)=Ein(ciclo)+(rhoin*cpin*abs(u_in)*eps(ciclo)*Tingresso)*dt*(r
(i+1)^2-r(i)^2)/2;

mass_in(ciclo)=mass_in(ciclo)+rhoin*abs(um)*eps(ciclo)*dt*(r(i+1)^2-
r(i)^2)/2;
    mass_in2(ciclo)=mass_in2(ciclo)+abs(mass_flow(ciclo))*dt*(r(i+1)^2-
r(i)^2)/2;
end,

for i=Nr*(Nz-1)+1:Nr*Nz,
    col=mod(i,Nr);
    if col==0, col=Nr; end;
    if um>=0,
        rho_out=rho(i);
        cp_out=cp(i);
        T_uscita=T(i);
```

```
        u_out=u(i+Nr);
    else
        T_uscita=T(i-Nr*(Nz-1));
        rho_out=rho(i-Nr*(Nz-1));
        cp_out=cp(i-Nr*(Nz-1));
        u_out=-um;
    end,
    if (T_uscita>Tuseful),

Eout_useful(ciclo)=Eout_useful(ciclo)+(rho_out*cp_out*u_out*eps(ciclo)*
T_uscita-rhoin*cpin*abs(um)*eps(ciclo)*Tin(ciclo))*dt*(r(col+1)^2-
r(col)^2)/2;
    end,

Eout(ciclo)=Eout(ciclo)+(rho_out*cp_out*u_out*eps(ciclo)*T_uscita)*dt*(
r(col+1)^2-r(col)^2)/2;

mass_out(ciclo)=mass_out(ciclo)+rho_out*u_out*eps(ciclo)*dt*(r(col+1)^2
-r(col)^2)/2;
end,

for i=Nr:Nr:Nr*Nz,
    Elosses(ciclo)=Elosses(ciclo)+(T(i)-T_amb)*alfa*dt*dz*raggio;
end,

dEsto(ciclo)=-Esto0(ciclo);
dmass_sto(ciclo)=-mass_sto0(ciclo);
for i=1:Nr*Nz,
    col=mod(i,Nr);
    if col==0, col=Nr; end;
    dEsto(ciclo)=dEsto(ciclo)+(eps(ciclo)*(rho(i)*cp(i)*T(i)-
rho_rif*cp_rif*Trif)+(1-eps(ciclo))*rho_p*cp_p*(T_par(i)-
Trif))*(r(col+1)^2-r(col)^2)/2*dz;
    dmass_sto(ciclo)=dmass_sto(ciclo)+eps(ciclo)*rho(i)*(r(col+1)^2-
r(col)^2)/2*dz;
end,
```

Molten salt temperature calculation

```
function
T=risoluzione_T(T,T_par_app,T_old,Nr,Nz,k,cp,cp_old,hv,rho,rho_old,dz,d
t,eps,r,R,alfa,u,um,Tin,frho_h,fcp_h,T_amb,ciclo,rhoin,cpin)

ae=zeros(Nz*Nr,1);
aw=zeros(Nz*Nr,1);
as=zeros(Nz*Nr,1);
an=zeros(Nz*Nr,1);
ap=zeros(Nz*Nr,1);

De=zeros(Nr*Nz,1);
Dw=zeros(Nr*Nz,1);
Dn=zeros(Nr*Nz,1);
Ds=zeros(Nr*Nz,1);
Vp=zeros(Nr*Nz,1);
Fs=zeros(Nr*Nz,1);
Fn=zeros(Nr*Nz,1);
```

```
Q=zeros(Nr*Nz,1);
C=zeros(Nr*Nz,1);
N=zeros(Nr*Nz,1);

A=[];
B=zeros(Nr*Nz,5);
b=zeros(Nz*Nr,1);
d=[-Nr,-1,0,1,Nr];

Tingresso=Tin;

for i=1:Nr*Nz,

    col=mod(i,Nr);
    if col==0, col=Nr; end;
    rig=floor((i-0.01)/Nr)+1;
    DR=(r(col+1)^2-r(col)^2)/2;
    if (col<Nr), ke=(k(i)+k(i+1))/2;
    else, ke=0; end;
    if (col>1), kw=(k(i)+k(i-1))/2;
    else, kw=0;  end;
    if (rig>1),
        kn=(k(i)+k(i-Nr))/2;
    else
        kn=0;
    end,

    if (rig<Nz),
        ks=(k(i)+k(i+Nr))/2;
    else,
        ks=0;
    end,

    Vp(i)=eps(ciclo)*rho(i)*cp(i)*DR*dz/dt;
    Vp_old(i)=eps(ciclo)*rho_old(i)*cp_old(i)*DR*dz/dt;
    Q(i)=hv(i)*dz*DR;

    if (col==1),
        Dw(i)=0;
    else, Dw(i)=kw*dz*r(col)/(R(col)-R(col-1));
    end,

    if (col==Nr),
        De(i)=0;
        C(i)=alfa*dz*r(col+1);
    else,
        De(i)=ke*dz*r(col+1)/(R(col+1)-R(col));
        C(i)=0;
    end,

    if (rig==1),
        if u(i)<0,
            Dn(i)=0;
            Ds(i)=ks/dz*DR;
            Fn(i)=rho(i)*cp(i)*u(i)*DR*eps(ciclo);
            Fs(i)=rho(i+Nr)*cp(i+Nr)*u(i+Nr)*DR*eps(ciclo);
```

```
        else,
                Fn(i)=0;
                Fs(i)=rho(i)*cp(i)*u(i+Nr)*DR*eps(ciclo);
                if (um==0),
                    rhoin=rho(i);
                    cpin=cp(i);
                    Tingresso=T(i);
                else,
                    T_prop=Tin;
                    rhoin=eval(frho_h);
                    cpin=eval(fcp_h);
                end,
                N(i)=(rhoin*cpin*u(i)*DR)*eps(ciclo);
                Ds(i)=ks/dz*DR;
                Dn(i)=0;
        end,
    end,

    if (rig==Nz),
        if u(i)>0,
            Dn(i)=kn/dz*DR;
            Ds(i)=0;
            Fn(i)=rho(i-Nr)*cp(i-Nr)*u(i)*DR*eps(ciclo);
            Fs(i)=rho(i)*cp(i)*u(i+Nr)*DR*eps(ciclo);
        else,
            Fs(i)=0;
            Fn(i)=rho(i)*cp(i)*u(i)*DR*eps(ciclo);
            N(i)=-(rhoin*cpin*u(i+Nr)*DR)*eps(ciclo);
            Dn(i)=kn/dz*DR;
            Ds(i)=0;
        end,
    end,

    if (rig~=1)&&(rig~=Nz),
        Dn(i)=kn/dz*DR;
        Ds(i)=ks/dz*DR;
        if (u(i)>0),
            Fn(i)=rho(i-Nr)*cp(i-Nr)*u(i)*DR*eps(ciclo);
            Fs(i)=rho(i)*cp(i)*u(i+Nr)*DR*eps(ciclo);
        else,
            Fn(i)=rho(i)*cp(i)*u(i)*DR*eps(ciclo);
            Fs(i)=rho(i+Nr)*cp(i+Nr)*u(i+Nr)*DR*eps(ciclo);
        end,
    end,
    ae(i)=De(i);
    aw(i)=Dw(i);
    as(i)=Ds(i)+max(-Fs(i),0);
    an(i)=Dn(i)+max(Fn(i),0);

b(i)=Q(i)*T_par_app(i)+Vp_old(i)*T_old(i)+C(i)*T_amb+N(i)*Tingresso;
    ap(i)=Vp(i)+max(Fs(i),-Fn(i))+Q(i)+Ds(i)+Dn(i)+De(i)+Dw(i)+C(i);

    if (an(i)~=0), B(i-Nr,1)=-an(i);   end;
    if (aw(i)~=0), B(i-1,2)=-aw(i);   end;
    if (ap(i)~=0), B(i,3)=ap(i);   end;
    if (ae(i)~=0), B(i+1,4)=-ae(i);   end;
    if (as(i)~=0), B(i+Nr,5)=-as(i);   end;
```

```
end,

A=spdiags(B,d,Nz*Nr,Nz*Nr);

T=A\b;
```

Molten salt velocity evaluation

```
function u=risoluzione_u(u,um,rhoin,rho,rho_old,dz,dt,Nz,Nr,eps,ciclo)

B1=zeros((Nz+1)*Nr,2);
A1=[];
b1=zeros(Nr*(Nz+1),1);

if (um>0),

    d1=[-Nr 0];
    B1(1:Nr,2)=1;
    b1(1:Nr)=um;

    for c2=Nr+1:2*Nr,
        B1(c2,2)=1;
        b1(c2)=um*rhoin/rho(c2-Nr)-dz/dt*(rho(c2-Nr)-rho_old(c2-
Nr))/rho(c2-Nr);
    end,
    for c2=Nr*2+1:Nr*(Nz+1),
        B1(c2-Nr,1)=-rho(c2-Nr*2)/rho(c2-Nr);
        B1(c2,2)=1;
        b1(c2)=-(rho(c2-Nr)-rho_old(c2-Nr))/rho(c2-Nr)*dz/dt;
    end,

else,

    d1=[0 Nr];

    B1(Nr*Nz+1:(Nz+1)*Nr,1)=1;
    b1(Nr*Nz+1:(Nz+1)*Nr)=um;

    for c2=Nr*(Nz-1)+1:Nr*(Nz),
        B1(c2,1)=1;
        b1(c2)=um*rhoin/rho(c2)+eps(ciclo)*dz/dt*(1-
rho_old(c2)/rho(c2));
    end,

    for c2=1:(Nz-1)*Nr,
        B1(c2,1)=1;
        B1(c2+Nr,2)=-rho(c2+Nr)/rho(c2);
        b1(c2)=(1-rho_old(c2)/rho(c2))*eps(ciclo)*dz/dt;
    end,

end,
A1=spdiags(B1,d1,Nr*(Nz+1),Nr*(Nz+1));
```

```
u=A1\b1;
```

Evaluation of heat loss to the environment

```
function [alfa, perc,
type_conv]=calcolo_alfa2(adiabatic,raggio,spessore,T_amb,v_vento,num_la
yer,conduttivita,Tparete,emissiv,L)

%Thermal resistence of wall, with radiative apport
if adiabatic==0,

    %convez forzata
    D_tank=(raggio+sum(spessore))*2;
    rho_amb=101325/(8314/28.9*(T_amb+273));
    k_amb=((T_amb+23)*(30-22.3)/100+22.3)*1e-3;
    mu_amb=((T_amb+23)*(208.2-159.6)/100+159.6)*1e-7;
    Re_amb=rho_amb*D_tank*v_vento/mu_amb;
    Pr_amb=0.7;
    if Re_amb>5e5,
        Nu=(0.037*Re_amb^0.8-871)*Pr_amb^0.333;
    else,
        Nu=0.664*Re_amb^0.5*Pr_amb^0.333;
    end,
    h_amb=Nu*k_amb/D_tank;

    %convez naturale

    Gr=9.81*L^3*(Tparete-
T_amb)/((Tparete+T_amb)/2+273)*rho_amb^2/mu_amb^2;
    Ra=Gr*Pr_amb;
    Nu_nat=(0.825+0.387*Ra^(1/6)/(1+(0.492/Pr_amb)^(9/16))^(8/27))^2;
    type_conv=Gr/Re_amb^2;          %<1 forced >1 natural
    h_nat=Nu_nat*k_amb/L;

    r_s=zeros(num_layer+1,1);
    R_eq=zeros(num_layer+2,1);
    r_s(1)=raggio;
    for i=2:num_layer+1,
        r_s(i)=spessore(i-1)+r_s(i-1);
        R_eq(i-1)=log(r_s(i)/r_s(i-1))/(2*pi*conduttivita(i-1));
    end,

R_eq(i)=((2*pi*r_s(i)*h_amb)+(2*pi*r_s(i)*h_nat)+(2*pi*r_s(i)*emissiv*5
.67*1e-8*(Tparete+T_amb+273*2)*((Tparete+273)^2+(T_amb+273)^2)))^-1;
    perc(1)=2*pi*r_s(i)*h_amb*R_eq(i);
    perc(2)=2*pi*r_s(i)*h_nat*R_eq(i);
    perc(3)=(2*pi*r_s(i)*emissiv*5.67*1e-
8*(Tparete+T_amb+273*2)*((Tparete+273)^2+(T_amb+273)^2))*R_eq(i);
    alfa=1/(sum(R_eq)*2*pi*raggio);
else,
    alfa=0;
    perc=[0 0 0];
    type_conv=0;
end,
```

Bibliography

[1] J. Pacheco, S. K. Showalter and W. J. Kolb, "Development of a Molten-Salt Thermocline Thremal Storage System for Parabolic Trough Plants," *Journal of Solar Engineering* , vol. 124, pp. 123-153, 2002, doi:10.1115/1.1464123.

[2] G. J. Kolb, "Evaluation of Annual Performance of 2-Tank and Thermocline Thermal Storage Systems for Trough Plants," *Journal of Solar Engineering* , vol. 133, p. doi:10.1115/1.4004239, 2011.

[3] M. Passoni and M. Radice, *Analisi tecnico-economica di sistemi di accumulo per impianti solari termodinamici a concentrazione parabolico-lineare,* Archivio tesi Politecnico di Milano: [https://www.politesi.polimi.it], 2011.

[4] F. Cavallaro, "Fuzzy topsis approach for assessing thermal-energy storage in concentrated solar power systems," *Applied Energy,* vol. 87, pp. 496-503, 2010, doi:10.1016/j.apenergy.2009.07.009.

[5] I. R. E. A. IRENA, "Concentrating Solar power - Cost Analysis," 2012.

[6] S. V. Garimella, S. Flueckiger and Z. Yang, "An integrated thermal and mechanical investigation of molten-salt thermocline energy storage," *Applied Energy* , vol. 88, pp. 2098-2105, 2011, doi:10.1016/j.apenergy.2010.12.031.

[7] F. G. F. Qin, X. Yang, Z. Ding, Y. Zuo, Y. Shao and R. Jiang, "Thermocline stability criterions in single-tanks of molten salt thermal energy storage," *Applied energy* , vol. 97, pp. 816-821, 2012, doi:10.1016/j.apenergy.2012.02.048.

[8] M. Binotti, "Electricity production from fossil fuels with carbon capture by Sorption Enhanced Water Gas Shift," 2011. [Online]. Available: www.politesi.polimi.it. [Accessed 01 March 2013].

[9] C. Xu, Z. Wang, Y. He, X. Li and F. Bai, "Parametric study and standby behavior of a packed-bed molten salt thermocline thermal storage system," *Renwable Energy* , vol. 48, pp. 1-9, 2012, doi:10:1016/j.renene.2012.04.017.

[10] T. E. W. Schumann, "Heat transfer: a liquid flowing through a porous prism," *Journal of the Franklin Institute,* vol. 208, no. 3, pp. 405-416, 1929.

[11] X. Yang, X. Yang, J. Ding, Y. Shao, F. Qin and R. Jiang, "Criteria for performance improvement of a molten salt thermocline storage system," *Applied Thermal Engineering* , vol. 48, pp. 24-31, 2012, doi:10:1016/j.applthermaleng.2012.04.046.

[12] C. Xu, Z. Wang, Y. He, X. Li and F. Bai, "Sensitivity analysis of the numerical study on the thermal performance of a packed-bed molten salt thermocline thermal storage system," *Applied Energy* , vol. 92, pp. 65-75, 2012, doi:10.1016/j.apenergy.2011.11.002.

[13] S. Flueckijer and S. Garimella, "Second-law analysis of molten-salt thermal Energy storage in thermoclines," *Solar Energy* , vol. 86, pp. 1621-1631, 2012, doi:10.1016/j.solener.2012.02.028.

[14] Z. Yang and S. V. Garimella, "Thermal analysis of solar thermal energy storage in a molten-salt thermocline," *Journal of Solar Energy Engineering*, vol. 84, pp. 974-985, 2010, doi:10.1016/j.solener.2010.03.007.

[15] R. Bayon and E. Rojas, "Simulation of thermocline storage for solar thermal power plants: from dimensionless results to prototypes and real-size tanks," *Journal of Heat and Mass transfer*, vol. 60, pp. 713-721, 14 February 2013.

[16] V. Smil, Energy in World History, 1994.

[17] IEA, "Key World Energy Statistics," 2012.

[18] B. Petroleoum, "Statistical Review of World Energy," June 2012.

[19] IEA, "Solar Energy Perspectives," 2011.

[20] A. Luque, Handbook of Photovoltaic Science and Engineering, Hegedus, ISBN 0-471-49196-9: John Wiley and Sons, 2003.

[21] Haverford. [Online]. Available: www.haverford.edu. [Accessed 03 April 2013].

[22] E. P. I. Association, "PV status Report," 2011.

[23] EPIA, "World Passes 100GW installed PV capacity," 11 February 2013. [Online]. Available: http://www.pv-magazine.com/news/details/beitrag/world-passes-100-gw-installed-pv-capacity-mark_100010145/#axzz2NbhgyqDI. [Accessed 15 March 2013].

[24] "Photovoltaic," Renewable Eenrgy in the California deserrt, [Online]. Available: http://webservices.itcs.umich.edu/drupal/recd/?q=node/156. [Accessed 23 March 2013].

[25] NREL, "Photovoltaic research," [Online]. Available: http://www.nrel.gov/pv/. [Accessed 18 February 2013].

[26] Meteonorm. [Online]. Available: www.meteonorm.com. [Accessed 22 March 2013].

[27] "CSP world," [Online]. Available: www.csp-world.com. [Accessed 23 March 2013].

[28] "Solar Pond," Solar Thermal magazine, [Online]. Available: http://www.solarthermalmagazine.com/learn-more/solar-ponds/. [Accessed 21 March 2013].

[29] G. Smestad, H. Ries, R. Winston and E. Yablonvitch, "The thermodyamic limits of light concentrators," *Solar Energy Materials*, vol. 21, pp. 99-111, 1990.

[30] [Online]. Available: see.murdoch.edu.au. [Accessed 01 April 2013].

[31] G. Manzolini, E. Macchi, P. Silva and M. Binotti, "Comparison of two commercial linear collectors in solar thremal plants: parabolic trough versus Fresnel," *Journal of Solar Energy Engineering*, 2011.

[32] [Online]. Available: kernenergien.de.

[33] Colzi and Petrucci, "Modelling On/Off - Design performance of solar tower plants," 2009. [Online]. Available: www.politesi.polimi.it.

[34] L. Simonin, "L'emploi industriel de la chaleur solaire," *Revue des deux Mondes*, vol. 15, no. mai-juin, 1876.

[35] C. Silvi, "Le origini tutte italiane del solare termodinamico. Gruppo per la storia dell'energia solare," [Online]. Available: http://www.rinnovabili.it/energia/termico/le-origini-tutte-italiane-del-solare-termodinamico/.

[36] GSES, "Pionieri in primo piano: Giovanni Francia," [Online]. Available: http://www.gses.it/pionieri/francia.php. [Accessed 25 March 2013].

[37] Treccani, "Generazione elettrica da fonti rinnovabili".

[38] Desertec. [Online]. Available: http://www.desertec.org/.

[39] Terna. [Online]. Available: www.terna.it. [Accessed 21 March 2013].

[40] D. Kearney, U. Herrmann, P. Nava, B. Kelly, R. Mahoney, J. Pacheco, R. Cable, N. Potrovitza, D. Blake and H. Price, "Assessment of a Molten Salt Heat Transfer Fluid in a Parabolic Trough Solar Field," *Journal of Solar Engineering* , vol. 125, 2003, doi:10.1115/1.1565087.

[41] D. Kearney, "Engineering Evaluation of a Molten Salt HTF in a Parabolic Trough Solar Field," [Online]. Available: [http://www.nrel.gov/csp/troughnet/pdfs/ulf_herrmann_salt.pdf].

[42] A. Gil, M. Medrano, I. Martorell, A. Lazaro, P. Dolado, B. Zalba and L. Cabeza, "State of the art on high temperature thermal Energy storage for power generation. Part 2 – Case studies," *Renewable and Sustainable Energy Reviews* , vol. 14, pp. 56-72, 2010, doi:10.1016/j.rser.2009.07.036.

[43] A. Gil, M. Medrano, I. Martorell, A. Lazaro, P. Dolado, B. Zalba and L. Cabeza, "State of the art on high temperature thermal Energy storage for power generation. Part 1 – Concepts, materials and modeling," *Renewable and Sustainable Energy Reviews* , vol. 14, pp. 31-55, 2010, doi:10.1016/j.rser.2009.07.035.

[44] NREL, "Concentrating Solar Power Projects," [Online]. Available: http://www.nrel.gov/csp/solarpaces/. [Accessed 29 March 2013].

[45] A. Galli, *Assessment of direct working fluid storage concepts for ORC power systems,* Archivio tesi Politecnico di Milano: [https://www.politesi.polimi.it], 2011.

[46] D. Brosseau, P. Hlava and M. J. Kelly, "Testing thermocline filler materials and molten-salt heat transfer fluids for thermal energy storage systems used in trough solar power plants," 2004. [Online]. Available: [www.nrel.gov/csp/troughnet/pdfs/brosseau_sand2004_3207_final.pdf].

[47] P. Li, J. Lew, W. Karaki, C. Chan, J. Stephens and Q. Wang, "Generalized charts of Energy storage effectiveness for thermocline heat storage tank design and calibration," *Solar Energy* , vol. 85, pp. 2130-2143, 2011, doi:10.1016/j.solener.2011.05.022.

[48] W. M. Kays, M. Crawford and B. Weigand, Convective heat and mass transfer, McGraw Hill, ISBN:0072468769, 2005.

[49] F. P. Incropera and D. P. D. Witt, Fundamentals of heat and mass transfer, John Wiley & Sons, 2012.

[50] R. Issa, A. Gosman and A. Watkins, "THE COMPUTATION OF COMPRESSIBLE AND INCOMPRESSIBLE RECIRCULATING-FLOWS BY A

NONITERATIVE IMPLICIT SCHEME," *JOURNAL OF COMPUTATIONAL PHYSICS,* vol. 62, pp. 66-82, 1986.

[51] S. V. Patankar, Numerical Heat transfer and mass flow, McGraw Hill, 1980.

[52] S. V. Garimella and Z. Yang, "Molten-salt thermal energy storage in thermoclines under different environmental boundary conditions," *Applied Energy* , vol. 87, pp. 3322-3329, 2010, doi:10.1016/j.apenergy.2010.04.024.

[53] N. Nakao, S. Kaguei and T. Funazkri, "Effect of fluid dispersion coefficient on particle-to-fluid heat transfer coefficients in packed beds: correlation of Nusselt number," *Chemical Engineering Science* , vol. 34, pp. 325-336, 1979.

[54] N. Wakao and S. Kaguei, Heat and mass transfer in packed beds, New York: Gordon and Beach, 1982.

[55] R. J. LeVeque, Finite difference methods for differential equations, 2005.

[56] M. N. Ozisik, Boundary value problems of heat conduction, ISBN 0-486-65990-9, 1968.

[57] C. P. Jefferson, "Prediction of Breakthrough Curves in Packed Beds: Applicability of Single Parameter Models," *Journal for the American Institute of Chemical Engineers,* vol. 18, p. 409–416, 1972.

[58] H. Zurigat and R. Liche, "Influence of inlet geometry on mixing in thermocline thermal energy storage," *Journal Heat Mass Transfer* , vol. 34, no. 1, pp. 115-125, 1991.

[59] T. Harrison and R. Randall, "Thermal Storage Experience at the MSSF and plans for the future," Sandia Laboratories.

[60] C. Zhengzhou Sunrise Technology Company. [Online]. Available: http://tysunrise.en.alibaba.com/. [Accessed 10 February 2013].

[61] NREL, "NREL TES Workshop," February 2003. [Online]. Available: www.nrel.gov. [Accessed 28 March 2013].

[62] C. a. C. co, "Hitec Heat Transfer Salt. Technical Bulletin.," [Online]. Available: [www.coal2nuclear.com].

[63] J. Pacheco, S. K. Showalter and W. J. Kolb, "Development of a molten-salt thermocline thermal storage system for parabolic trough plants," 2001. [Online]. Available: [http://www.nrel.gov/csp/troughnet/pdfs/jpacheco_thermocline.pdf].

[64] A. Mawire, S. H. Taole and R. V. d. Heetkamp, "Experimental investigation on simultaneous charging and discharging of an oil storage tank," *Energy Conversion and Management* , vol. 65, pp. 245-254, 2013, doi:10.1016/j.enconman.2012.08.011 .

[65] G. Manzolini, A. Giostri, C. Saccillotto, P. Silva and E. Macchi, "Development o fan innovative code for the design of thermodynamic solar power plants Part B: Performance assessment of commercial and innovative technologies," *Renewable Energy* , vol. 36, pp. 2465-2473, 2011, doi:10.1016/j.renene.2011.02.003.

[66] G. Manzolini, A. Giostri, C. Saccillotto, P. Silva and E. Macchi, "Development o fan innovative code for the design of thermodynamic solar power plants Part A: Code description and test case," *Renewable Energy,* vol. 36, pp. 1993-2003, 2011, doi:10.1016/j.renene.2010.12.027.

[67] G. Manzolini, A. Giostri, C. Saccilotto, P. Silva and E. Macchi, "A numerical model for off-design performance prediciotn for parabolic trough based solar power plants," *Solar Energy Engineering*, vol. 134, pp. 1208-1221, 2012.

[68] T. Gropp, "US$12 billion in World Bank funds would be better invested in desert power than in fossil fuels," 21 November 2012. [Online]. Available: [http://www.desertec.org/en/press/press-releases/121121-01-us12-billio].

[69] E. Gonzo, "Estimating correlations for the effective thermal conductivity of granular materials," *Journal of Chemicla Engineering* , vol. 90, pp. 299-302, 2002.

[70] A. Giostri, M. Binotti, P.Silva, E. Macchi and G. Manzolini, "Comparison of two commercial linear collectors in solar thermal plants: parabolich trough vs Fresnel," in *Proceedings of the ASME 5th International Conference on Energy Sustainability*, Washington, 2011.

[71] NREL, "Power Technologies Energy Data Book, Fourth edition," August 2006. [Online]. Available: [http://www.nrel.gov/analysis/power_databook/docs/pdf/39728_complete.pdf]. [Accessed 01 April 2013].